# Identification of Excited States and Evidence for Octupole Deformation in $^{226}$U

Thesis submitted in accordance with the requirements of
the University of Liverpool for the degree of Doctor in Philosophy

by

**Paul Thomas Greenlees**

Oliver Lodge Laboratory July 1999

*This thesis is dedicated to my parents,*
*Tracey, Jessie, Ronnie, Rosie and Frank (R.I.P.).*

# Abstract

Excited yrast states in the neutron-deficient nucleus $^{226}$U have been identified in two experiments performed at the Accelerator Laboratory of the University of Jyväskylä, Finland. In the first, the technique of recoil-decay tagging was employed using the JUROSPHERE plus RITU device, where the reaction channel of interest is selected through correlation with a characteristic decay. In the second, the RITU device was employed to study the $\alpha$ decay of $^{230}$Pu. Through these experiments the level scheme of $^{226}$U was deduced for the first time.

Interleaved bands of positive- and negative- parity states suggest the octupole nature of this nucleus, and the behaviour of the difference in aligned angular momentum between the negative- and positive- parity states with rotational frequency is consistent with that expected of a rotating reflection-asymmetric shape. This represents an extension of the known octupole-deformed nuclei to $Z = 92$.

The interleaved bands of alternating parity are connected by strong electric dipole transitions, and values of $|D_0/Q_0|$, extracted from $E1/E2$ $\gamma$-ray branching ratios, suggest that $^{226}$U possesses one of the largest $E1$ moments near to the ground state of the nuclei in this region.

# Acknowledgements

Firstly, I would like to thank Professor P.J. Twin for allowing me this opportunity to carry out research at the University of Liverpool.

I'd also like to thank my supervisor, Professor P.A. Butler for his support and interest in this work; and for giving me the chance to live in Finland for a year. Gratitude also goes to Dr. G.D. Jones for all his help and advice during the last three years.

I am also most grateful to everyone at the University of Jyväskylä, Finland, for looking after me during my stay. Special thanks to Professors R. Julin and M. Leino for all their assistance and hospitality.

Many thanks to Dr. J.F.C. Cocks, Dr. P. Campbell, Dr. J.F. Smith and
Dr. R.D. Herzberg for proof-reading this work.

Thanks to the computer support staff at Liverpool, and Dr. P. Jones in Jyväskylä for all their help with my computer troubles.

Many thanks to EPSRC for funding my Ph.D studentship.

I would also like to thank all the students in both Liverpool and Jyväskylä for providing entertainment both in and out of working hours.

Finally, special mentions for Dr. J.F.C. Cocks and Dr. K.J. Cann for introducing me to the bright lights of Jyväskylä back in 1995, and everything since; also to Dr. R.G. Allatt, Dr. M.B. Smith, Dr. J.F. Smith, Alex Keenan, Stephen King, Mike Taylor, Adrian Chewter, Neil Hammond and to Mr. A.R. Ball and Mr. S.Z. Holt for friendship, football and numerous other things.

# Contents

# Chapter 1

# Introduction to Nuclear Properties

## 1.1 Introduction

The atomic nucleus consists of protons and neutrons, and is extremely small ($10^{-14}$ to $10^{-15}$ m in diameter). The protons, being positively charged, repel each other through the Coulomb interaction. The very fact that protons and neutrons can form stable systems in such a small spatial volume is an indication of the presence of a strong attractive force. A great deal is already known about this *strong* nuclear force. It is known that the mass of a given nucleus is less than the sum of its constituent nucleons. This *mass defect* can be equated to an energy, known as the nuclear binding energy. A plot of the nuclear binding energy per nucleon as a function of mass can be found in many texts (see, for example, [Krane 88]). It is well known that such a plot forms a curve, with a maximum at around A$\simeq$60, and that above this value the binding energy per nucleon remains approximately constant, at around 8 MeV. The size of nuclei, together with the empirical observation that the nuclear force can effectively be neglected when dealing with atomic phenomena, show that the nuclear force must have a short range. Electron scattering experiments show that the density of nuclear matter is almost constant and independent of the number of nucleons (given by the atomic mass number, A). The shape of the binding energy per nucleon curve, and the fact that the nuclear density is almost constant, indicate that

the nuclear force *saturates*. If this were not the case, and the nuclear force extended equally to all nucleons, the binding energy per nucleon and the nuclear density would increase with A. In addition to this, we know that the masses of *mirror nuclei*, (nuclei where the number of protons and neutrons are interchanged) are almost identical after the different Coulomb interaction strengths are corrected for. This means that the nuclear force must be charge symmetric. There is a wealth of evidence (e.g. nuclear binding energies, proton and neutron separation energies, energies of first excited states) that certain numbers of protons and neutrons are more stable than others. These numbers of nucleons, known as *magic numbers*, provide an insight into the fact that the nucleus has a shell structure, similar to that of the electrons surrounding the atom. The ordering and energy separation of nuclear states can be calculated using the non-relativistic Schrödinger equation for the motion of a particle in a potential. The form of the potential is thus of paramount importance if we wish to accurately predict the nuclear level energies. It should also be remembered that nucleons are spin 1/2 particles or *fermions*, and as such are governed by the Pauli Exclusion Principle; the nuclear states must be occupied accordingly. In a calculation with a suitable potential, gaps in the level density appear for certain numbers of nucleons, corresponding to the magic numbers. In the nucleus, the potential is generated by the nucleons themselves, and a good first-order approximation for the nuclear potential is a central or spherically symmetric one. The nuclear potential and the modifications required to accurately reproduce the experimentally observed magic numbers will be discussed later in this work.

The shell model, using a central potential, has been very successful in predicting the properties of nuclei close to closed shells. However, as the number of valence nucleons (number of nucleons beyond a closed shell) is increased, the residual interactions between the valence nucleons that cannot be described by the mean field approximation, mean that the shell model calculations become intractable. Coherence in the motion of these valence particles can lead to effects where many nucleons move in a similar manner. These *collective* effects can be understood using more macroscopic

models of the nucleus, rather than the microscopic approach of the shell model, which aims to describe the motion of single particles. It is the build up of strength in these residual interactions that can drive the nucleus away from sphericity, and in some cases the total energy of the nucleus can be lower if it has a permanently deformed shape. This thesis is devoted to the study of deformed nuclei, and the theory presented in the remainder of this chapter and the next is strongly biased towards the properties of such nuclei.

## 1.2 Deformation

The nuclear shape can be parameterised in terms of a spherical harmonic or multipole expansion. The nuclear surface is defined by a radius vector pointing from the origin to the surface. In the case of axial symmetry

$$R(\theta,\phi) = c(\beta_\lambda)\, R_0 \left[1 + \sum_{\lambda=2}^{\lambda_{max}} \beta_\lambda Y_{\lambda 0}(\theta,\phi)\right] \tag{1.1}$$

where $R_0$ is the radius of a sphere having the same volume as the deformed nucleus and the $\beta_\lambda$ expansion coefficients are known as the deformation parameters. The factor $c(\beta_\lambda)$ is due to the volume conservation condition. $Y_{\lambda 0}$ is a spherical harmonic of order $\lambda$. The lowest multipole, $\lambda = 2$, corresponds to quadrupole deformation and a spheroidal shape. The next multipole, $\lambda = 3$, corresponds to octupole deformation. Octupole deformation describes reflection-asymmetry in the nuclear shape, giving the nucleus a shape similar to that of a pear. The properties of reflection-asymmetric nuclei will be discussed in the next chapter.

## 1.3 Rotation

An important consequence of deformation is the fact that rotational motion is a possible mode of excitation. In the spherical case, it is not possible to observe the collective rotation about an axis of symmetry, since the different orientations of the nucleus are

quantum-mechanically indistinguishable. In the case of an axially-symmetric nucleus, there is a set of axes of rotation, perpendicular to the symmetry axis. The rotational angular momentum, $\vec{R}$, is generated by the collective motion of many nucleons about this axis. Additional angular momentum can be generated by the intrinsic angular momentum of any valence nucleons, $\vec{J}$. The total angular momentum, $\vec{I}$, of the nucleus is then

$$\vec{I} = \vec{R} + \vec{J}. \tag{1.2}$$

This angular momentum coupling is shown schematically in figure 1.1.

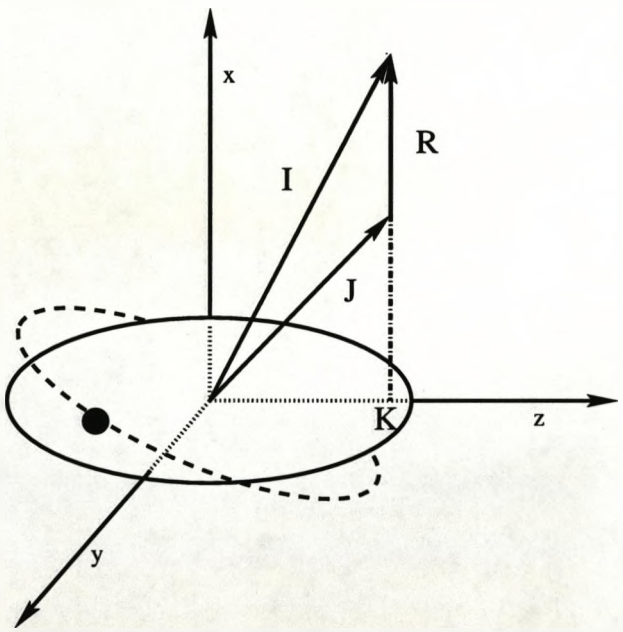


**Figure** 1.1: Schematic of the coupling of the collective angular momentum, $\vec{R}$ and the intrinsic angular momentum of the valence nucleons, $\vec{J}$. The projection of the total angular momentum, $\vec{I}$, onto the symmetry axis is $K$.

The intrinsic angular momentum of the valence nucleons, $\vec{J}$, is the sum of the angular momenta of the individual valence nucleons, i.e. $\vec{J} = \sum_{i=1}^{A} \vec{j}_i$. The projection of the total angular momentum onto the symmetry axis is $K$, and is the same as the projection of $\vec{J}$. The projection of the angular momentum, $\vec{j}$, of a valence nucleon is

$\Omega$; thus $K = \sum_{i=1}^{A} \Omega_i$. In the ground-state rotational band of an even-even nucleus, the valence particles are paired (see section 1.4) such that $\vec{J} = 0$, and the total angular momentum $\vec{I} = \vec{R}$.

The collective rotational energy can be determined through analogy with a classical rotating rigid body. The classical kinetic energy of the rotating rigid body is

$$E = \frac{1}{2}\mathcal{J}\omega^2 \tag{1.3}$$

where $\mathcal{J}$ is the moment of inertia and $\omega$ is the rotational frequency. By analogy to the quantum mechanical case, this becomes

$$E = \frac{\langle \hat{I}^2 \rangle}{2\mathcal{J}} \quad ; \quad \langle \hat{I}^2 \rangle = \hbar^2 I\,(I+1)\,. \tag{1.4}$$

Thus the rotational motion of the nucleus leads to a sequence of states with energies

$$E = \frac{\hbar^2}{2\mathcal{J}^{(0)}} I\,(I+1)\,. \tag{1.5}$$

In the above equations $\mathcal{J}^{(0)}$ is the static moment of inertia. It should be noted that the nucleus, however, is not a rigid body, and measured moments of inertia are somewhat less (30 to 50%) than rigid body values at low spin [Bardeen 57]. This is due to the effects of the pairing interaction, which make the nucleus behave like a superfluid. Pairing is discussed in section 1.4. Experimental moments of inertia are also larger than those calculated for the rotation of a superfluid, showing that the nucleus is somewhere between these two extremes. As the nucleus rotates, it is found that the moment of inertia changes as a function of spin.

## Moments of Inertia

The rotating nucleus can be described in terms of its angular rotational frequency, $\omega$. Classically, this is

$$\omega = \frac{dE}{dI}. \tag{1.6}$$

The quantum-mechanical analogue of this is given by

$$\hbar\omega = \frac{dE(I)}{d\sqrt{I\,(I+1) - K^2}} \tag{1.7}$$

where $\sqrt{I\,(I+1) - K^2}$ is the projection of the total angular momentum onto the rotational axis, known as the *aligned angular momentum*, $I_x$. For a $K = 0$ rotational band of stretched $E2$ transitions this can be approximated by

$$\hbar\omega = \frac{E_I - E_{I-2}}{\sqrt{I\,(I+1)} - \sqrt{(I-2)\,(I-1)}} \simeq \frac{E_\gamma}{2} \quad when \quad I \gg K. \tag{1.8}$$

Rotational energy spectra can be discussed in terms of two spin-dependent moments of inertia, which are related to the first- and second-order derivatives of the excitation energy with respect to the *aligned angular momentum*, $I_x$. The first order derivative is the *kinematic moment of inertia*,

$$\mathcal{J}^{(1)} = I_x \left(\frac{dE}{dI_x}\right)^{-1} \hbar^2 = \hbar\frac{I_x}{\omega}. \tag{1.9}$$

The kinematic moment of inertia can be related to the transition energy, $E_\gamma$, through equation 1.5. For a rotational band

$$E_\gamma = \frac{\hbar^2}{2\mathcal{J}^{(1)}}\,(4I - 2)\,. \tag{1.10}$$

The second order derivative is the *dynamical moment of inertia*,

$$\mathcal{J}^{(2)} = \left(\frac{d^2E}{dI_x^2}\right)^{-1} \hbar^2 = \hbar\frac{dI_x}{d\omega}. \tag{1.11}$$

The dynamical moment of inertia can be related to the difference in transition energy of consecutive $\gamma$ rays,

$$\Delta E_\gamma = \frac{4\hbar^2}{\mathcal{J}^{(2)}}. \tag{1.12}$$

Thus, if the dynamical moment of inertia were a constant, the transition energy difference would be the same for all values of spin. Often this is not true and $\mathcal{J}^{(2)}$

is found to increase with increasing spin. The two moments of inertia can related as follows:

$$\mathcal{J}^{(2)} = \frac{dI_x}{d\omega} = \frac{d}{d\omega}\left(\omega\mathcal{J}^{(1)}\right) = \mathcal{J}^{(1)} + \omega\frac{d\mathcal{J}^{(1)}}{d\omega}. \tag{1.13}$$

In the limit of rigid rotation, $\mathcal{J}^{(2)} \simeq \mathcal{J}^{(1)}$.

## 1.4 Pairing

The pairing interaction is an attractive force that occurs between identical nucleons in the same $j$ orbit. The interaction is such that the energy of the $J = 0$ configuration for the two nucleons is much lower in energy than any other. The existence of pairing correlations in the nucleus is well supported by experimental evidence. Some examples are given below:

- the ground-state spin of all even-even nuclei is $0\hbar$, which suggests that there is a force that acts to couple nucleons pairwise such that their the angular momenta cancel out;
- the energy of the first excited non-collective state is much higher (above 1 MeV) in even-even nuclei than in odd-mass nuclei;
- the ground-state spin of odd-mass nuclei is determined by the spin of the last nucleon, which is unpaired;
- the measured moments of inertia of nuclei are much less than rigid-body values, suggesting that the nucleus may behave like a "superfluid";
- the masses of even-even nuclei, when compared to their odd-mass neighbours, are much lower. This suggests that the gain in binding energy is much larger when a nucleon is added to an odd mass nucleus than when a nucleon is added to an even mass nucleus.

Thus, in the ground state of an even-even nucleus, all the nucleons are coupled pairwise, such that total angular momentum is $0\hbar$. The strength of the pairing interaction, $G$, is larger for high-$j$ orbits and is dependent upon the *spatial overlap* of the two nucleons. The strength therefore decreases with mass, since in heavier nuclei the outer nucleons are further apart. The strength is also lower for protons than for neutrons, due to the effect of Coulomb repulsion. The strength can be estimated from

$$G_p = \frac{17}{A}\ MeV, \quad G_n = \frac{23}{A}\ MeV.$$

## Coriolis Anti-Pairing

The two nucleons in a given orbit have velocities of opposite sign (time-reversed orbits) and as rotation is induced the Coriolis force acts differently on each of them. This is shown schematically in figure 1.2

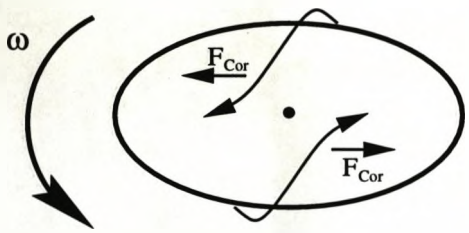


**Figure** 1.2: Illustration of the Coriolis force, which when the nucleus is rotated, acts to break the pairs of nucleons coupled to $J^\pi = 0^+$ . The axis of rotation points up out of the plane of the paper.

The classical Coriolis force is given by the expression

$$\vec{F}_{Cor} = -2m\left(\vec{\omega} \times \vec{V}\right) \tag{1.14}$$

where $m$ is the mass of the particle, $\vec{\omega}$ is the rotational frequency and $\vec{V}$ is the velocity of the particle. It can be seen that the Coriolis force acts to break the pair of nucleons which are coupled to $J^\pi = 0^+$. This is known as the Coriolis anti-pairing effect (CAP) [Mottelson 60]. A striking feature of this effect is the observation of *backbending* which occurs in certain nuclei. Backbending occurs when the Coriolis force,

defined in equation 1.14, becomes greater than the pairing energy of two nucleons in a time-reversed orbit. The phenomenon is characterised by a sudden increase in the moment of inertia, along with a decrease in rotational frequency. Thus in a plot of the moment of inertia against the square of the rotational frequency, the moment of inertia bends back and up, hence the name backbending. The first observation of this phenomenon was interpreted as the consequence of breaking a pair of $i_{13/2}$ neutrons which then align their angular momentum with the rotation axis [Stephens 72a], and was first observed in the ground state rotational bands of $^{162}$Er and $^{158,160}$Dy [Johnson 71].

## Pairing and the Fermi Surface

The pairing interaction not only couples pairs of nucleons in state $j$ to $J^\pi = 0^+$ but also to $J^\pi = 0^+$ states composed from two nucleons in a different $j$ state, $j'$. The effect of this is that pairs of nucleons in an orbit, $j$, coupled to $J^\pi = 0^+$, can be "scattered" into another orbit, $j'$, as a pair, still with $J^\pi = 0^+$. Far below the Fermi surface the Pauli principle forbids such scattering to occur since the orbits above $j$ are filled. This is how it is possible to consider independent particle motion in such a dense object as the nucleus. However, near to the Fermi surface where there is some probability that orbits are not occupied, this scattering can occur. The scattering results in a "smearing" of the Fermi surface. In the absence of pairing, orbits would simply be filled sequentially in accordance with the Pauli principle until all $A$ nucleons had been placed in the lowest orbits, giving a sharply defined Fermi surface. The effect of pairing on the Fermi surface is shown in figure 1.3.

The smearing of the Fermi surface leads to the concept of *quasiparticles* [Bardeen 57, Bohr 58], which can be considered as a linear combination of particle and hole wavefunctions. The probability that a state $i$ is occupied by a hole or a particle is given by the expressions

$$U_i = \frac{1}{\sqrt{2}}\left[1 + \frac{(\epsilon_i - \lambda)}{\sqrt{(\epsilon_i - \lambda)^2 + \Delta^2}}\right]^{\frac{1}{2}}, \quad V_i = \frac{1}{\sqrt{2}}\left[1 - \frac{(\epsilon_i - \lambda)}{\sqrt{(\epsilon_i - \lambda)^2 + \Delta^2}}\right]^{\frac{1}{2}} \tag{1.15}$$

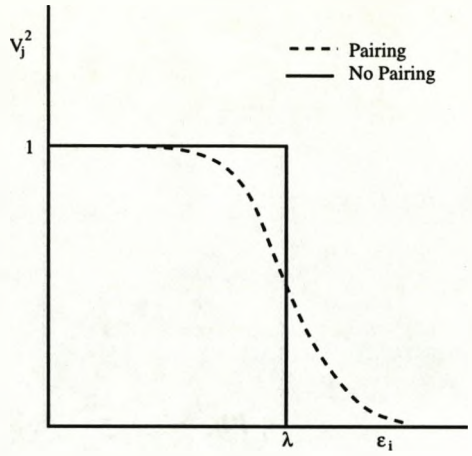


**Figure** 1.3: Schematic representation of the smearing of the Fermi surface due to the pairing interaction. This is understood in terms of the scattering of pairs of particles in a time-reversed orbit, $j$, to another, $j'$.

where $U_i^2$ is the probability the the orbit $i$ is occupied by a hole and $V_i^2$ is the probability the orbit $i$ is occupied by a particle; $\epsilon_i$ is the single particle energy, $\Delta$ is the pair gap parameter and $\lambda$ is the Fermi energy (see [Casten 90] for a more detailed discussion of these quantities). The probabilities are normalised such that $U^2 + V^2 = 1$. The pair gap parameter $\Delta$ and number of particles $n$ can be related to particle and hole occupation probabilities by

$$\Delta = G \sum_i U_i V_i, \quad n = 2 \sum_i V_i^2. \tag{1.16}$$

It can be seen that, far below the Fermi energy ($\epsilon_i \ll \lambda$) $V_i^2 = 1$, and far above the Fermi energy ($\epsilon_i \gg \lambda$) $U_i^2 = 1$. Close to the Fermi surface the occupation probabilities are mixed. In an even-even nucleus an energy of $2\Delta$ is required to excite a single nucleon to a higher state (two-quasiparticle excitation), whilst in an odd-mass nucleus the nucleon is already unpaired. This can explain the observed difference in energy between the first non-collective excited states in even-even nuclei when compared to odd-mass nuclei.

## 1.5 The Nilsson Model

As mentioned in the introduction to this chapter, the spherical shell model provides an excellent description of nuclei close to closed shells. However, the large body of evidence that points toward the existence of deformed nuclei necessitates a model that uses a deformed nuclear potential. One such potential is the modified harmonic-oscillator potential, which was first used by Nilsson [Nilsson 55] to investigate the effect of deformation on the single-particle orbits. The Hamiltonian in the case of a modified harmonic-oscillator potential can be written

$$H_{Nil} = \frac{-\hbar^2}{2m}\nabla^2 + \frac{m}{2}\left(\omega_x^2 x^2 + \omega_y^2 y^2 + \omega_z^2 z^2\right) - 2\kappa\hbar\omega_0\left[\vec{l}.\vec{s} - \mu\left(l^2 - \langle l^2\rangle_N\right)\right] \quad (1.17)$$

where the $\left(\vec{l}.\vec{s}\right)$ term represents the spin-orbit force, first introduced by Haxel, Jensen and Suess [Haxel 49] and the term $l^2 - \langle l^2\rangle_N$ was introduced by Nilsson to simulate the flattening of the nuclear potential at the centre of the nucleus. The factors $\kappa$ and $\mu$ determine the strength of the spin-orbit and $l^2$ terms, respectively. The $\omega_{x,y,z}$ terms are the one-dimensional oscillator frequencies which can be expressed as functions of the deformation. In the axially-symmetric case

$$\omega_x^2 = \omega_y^2 = \omega_0^2\left(1 + \frac{2}{3}\epsilon\right), \quad \omega_z^2 = \omega_0^2\left(1 - \frac{4}{3}\epsilon\right) \quad (1.18)$$

where $\epsilon$ is the deformation parameter, and $\omega_0$ is the oscillator frequency ($\hbar\omega_0 = 41A^{-1/3}$ MeV) in the spherical potential with $\epsilon = 0$. Using this deformation-dependent Hamiltonian, the single-particle energies can be calculated as a function of $\epsilon$. A plot of single-particle energy against deformation is known as a Nilsson diagram, an example of which for neutrons with N$\geq$126 is shown in figure 1.4.

The Nilsson orbitals can be characterised by the so-called asymptotic quantum numbers

$$\Omega^\pi\left[Nn_z\Lambda\right] \quad (1.19)$$

where $N$ is the principal quantum number, $\Omega$ is the projection of the single-particle angular momentum onto the symmetry axis ($z$), $\Lambda$ is the projection of the orbital

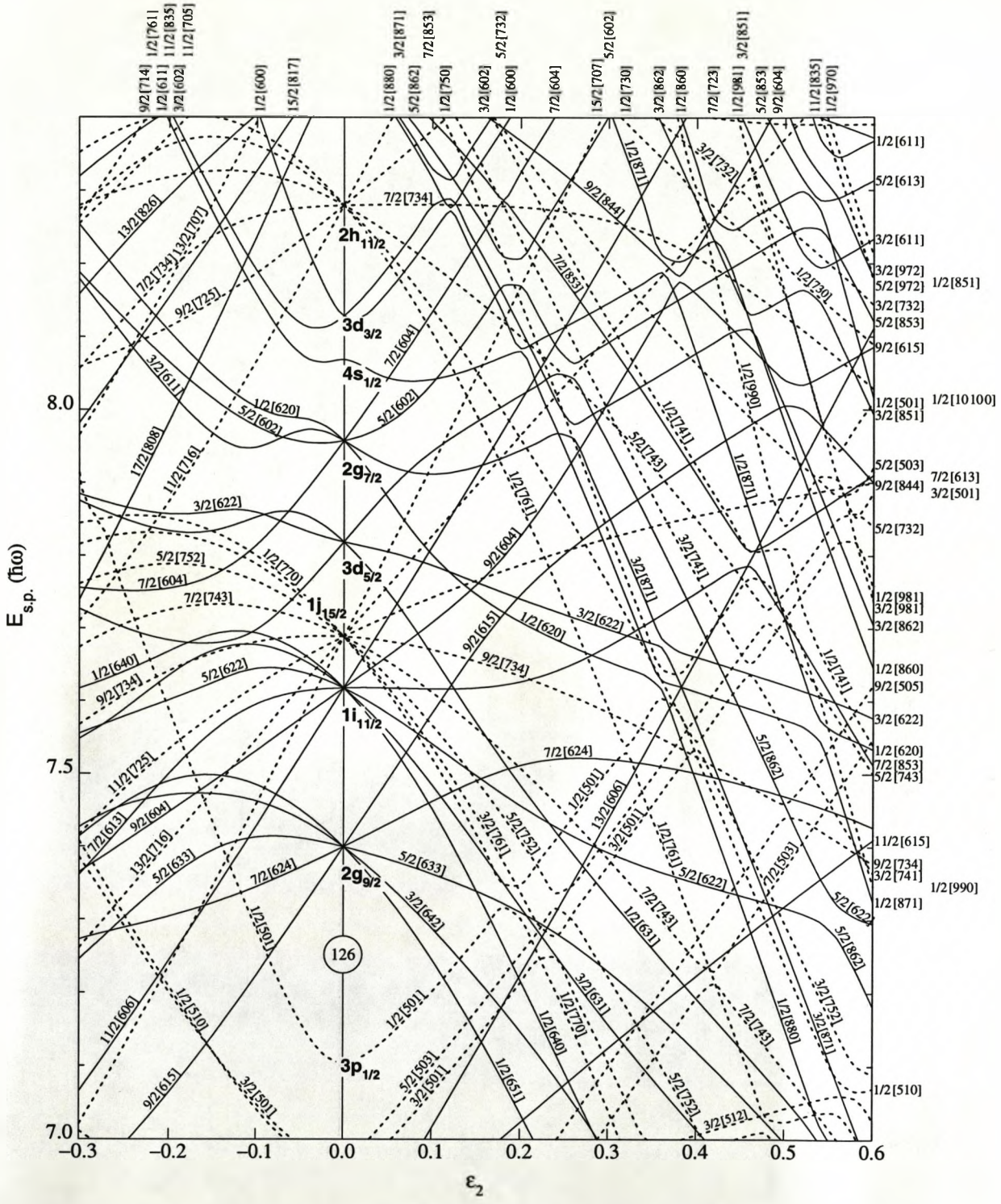


**Figure** 1.4: Nilsson diagram for neutrons, N≥126. The deformation parameter $\epsilon_2$ is approximately $0.95\beta_2$.

angular momentum onto the symmetry axis and $n_z$ is the number of oscillator quanta along the symmetry axis. The parity of the state, $\pi$, is determined by $(-1)^N$. The projection of the intrinsic spin of the nucleon onto the symmetry axis is $\Sigma(= \pm\frac{1}{2})$, thus we can define $\Omega = \Lambda \pm \frac{1}{2}$. It should also be remembered that if $N$ is even, then $(n_z + \Lambda)$ must also be even. Similarly if $N$ is odd, then $(n_z + \Lambda)$ must be odd. It can be seen in figure 1.4 that at zero deformation, the $(2j+1)$-fold degeneracy of a given $j$ state is not lifted. When the deformation is introduced, the $j$ states split into two-fold degenerate levels, the number of which from a state $j$ is $j + \frac{1}{2}$. Many of the properties of the Nilsson orbitals can be understood in simple terms. If we consider the motion of particles around a prolate deformed shape, as shown in figure 1.1, we can define the classical orbit angle, $\theta$, as being approximately $\theta = sin^{-1}(K/j)$ [Casten 90]. Thus it can be seen that low $K$ values correspond to motion around the equator of the nucleus. Since the orbiting nucleon spends more time closer to the majority of the nuclear matter, these "equatorial" orbits will be lower in energy. In addition to this, $\theta$ changes slowly for low $K$, and more rapidly for higher $K$, thus the difference in energy between successive $K$ values increases with increasing $K$. It is forbidden by the Pauli Principle that any two levels with the same quantum numbers may cross, thus we can expect that as an orbit approaches another with the same $K$ and $\pi$, the two levels will repel each other. The interaction between the two orbitals means, however, that though the levels do not cross, the wave function properties are exchanged near the inflection point. The effect of the strong spin-orbit interaction is evidenced by the lowering of the $i_{13/2}$ shell. This $l = 6$ shell has positive parity, and lies in a region of predominantly negative-parity orbits. Since there are few orbits nearby with the same $K$ and $\pi$ values, the $i_{13/2}$ orbits are extremely pure and very straight. They remain so out to very large deformations. High-$K$ orbits also remain rather straight, since there are no other orbits of the same $K$ nearby. All these properties are evident in figure 1.4.

In order to calculate the total energy of the nucleus, a summation of all populated single-particle energies can be made. The steep down-slope of some orbitals as a

function of increasing deformation leads to the conclusion that some deformed configurations will have lower energy than a spherical one. Thus, within the framework of the Nilsson model, it is possible to predict stable deformation for nuclei removed from closed shells.

## 1.6 The Strutinsky-Shell Correction Method

As discussed in the previous section, it is possible to calculate the total energy of the nucleus through a summation of single-particle energies. This procedure is reasonably successful in that it can predict the existence of stably-deformed shapes, but it fails to accurately reproduce some of the bulk properties of the nucleus, such as the total binding energy. Another approach is to use the macroscopic liquid drop model (see for example [Nilsson 95] and references therein). This approach, although reproducing the bulk properties of the nucleus well, fails to predict the existence of stable deformation in the nuclear ground state and other properties such as the second minimum in the fission barrier of actinide nuclei. Thus an approach that incorporates both of these approaches is required. Strutinsky [Strutinsky 67, Strutinsky 68] applied the concepts of both the liquid-drop model and the shell model to accurately reproduce observed experimental nuclear ground-state energies.

The basis of the method is that the total energy is split into two terms; the first is a smoothly varying energy derived from the liquid drop model, and the second a rapidly varying part that is calculated from the fluctuations in the shell model energy,

$$E_{tot} = E_{ldm} + E_{shell}(protons) + E_{shell}(neutrons). \tag{1.20}$$

The shell energy, $E_{shell}$, is calculated independently for protons and neutrons, and can be defined as the difference between the actual discrete level density, $g$, and a "smeared" level density $\tilde{g}$. The discrete and smeared level densities are given by

$$g(e) = \sum_i \delta(e - e_i) \tag{1.21}$$

and:

$$\tilde{g}(e) = \frac{1}{\gamma\sqrt{\pi}} \sum_i f_{corr}\left(\frac{e-e_i}{\gamma}\right) exp\left(-\frac{(e-e_i)^2}{\gamma^2}\right). \tag{1.22}$$

Here $\gamma$ is an energy of the order of the shell spacing $\hbar\omega_0$, and $f_{corr}$ is a correction function which keeps the long-range variation over energies much larger than $\hbar\omega_0$ unchanged. The shell energy can thus be calculated using

$$E_{shell} = 2\sum e_i - 2\int e\tilde{g}(e)\,de \tag{1.23}$$

where the factor 2 arises because of the double degeneracy of the deformed levels. This method has been used to good effect to predict the existence of stably deformed reflection-asymmetric nuclear ground states [Möller 81, Nazarewicz 84], and some of the results of these calculations will be discussed in section 2.1.

## 1.7 The Cranked Shell Model

The cranked shell model was introduced by Inglis in 1954 [Inglis 54], and was further developed by Bengtsson and Frauendorf [Bengtsson 79]. The model gives a microscopic description of the influence of rotation on single-particle motion. In this way, the collective angular momentum can be determined through a summation over the single-particle angular momenta, thus the theory can be used to describe single-particle as well as collective effects.

The rotation is treated classically, with the rotation vector coinciding with one of the main axes of the nucleus. The nucleons can then be described as independent particles moving in a rotating potential. The calculations are then performed in the intrinsic co-ordinates of the rotating system. The single-particle cranking Hamiltonian is defined by

$$h^{\omega} = h^0 - \hbar\omega j_x \tag{1.24}$$

where $h^0$ is the Hamiltonian in the laboratory system, $j_x$ is the total angular momentum projection operator onto the rotation axis, and the term $-\hbar\omega j_x$ contains the Coriolis and centrifugal terms which modify the nucleon orbitals. The Coriolis force

acts to align the angular momenta of the nucleons with the rotation axis. The eigenvalues of this Hamiltonian are known as Routhians. The total cranking Hamiltonian can be obtained by summation over all of the independent particles of the system,

$$H^{\omega} = H^{0} - \hbar\omega I_{x}. \tag{1.25}$$

A summation over all occupied orbits, $\nu$, of the eigenvalues plus a contribution from the $\hbar\omega j_x$ terms yields the total energy in the laboratory frame,

$$E = \sum_{\nu} e_{\nu}^{\omega} + \omega \sum_{\nu} \langle \nu^{\omega} | j_x | \nu^{\omega} \rangle. \tag{1.26}$$

The projection of the total angular momentum onto the rotation axis can be determined by

$$I_x = \sum_{\nu} \langle \nu^{\omega} | j_x | \nu^{\omega} \rangle. \tag{1.27}$$

A diagram of the single-particle energy against the rotational frequency is known as a Routhian plot, and in some cases the effect of rotation is quite large. The differential of the Routhian, $e^{\omega}$, is related to the aligned angular momentum, $i_x$, by

$$i_x = -\frac{de^{\omega}}{d\omega}. \tag{1.28}$$

This relation allows the aligned angular momenta of experimental data to be compared to theoretical Routhians. The method of transforming experimental data into the rotational frame of reference is discussed below.

The effects of the pairing interaction can also be incorporated into the cranked shell model. The cranking Hamiltonian is modified to include a pairing term,

$$H = H^{0} - \hbar\omega J_x - \Delta\left(P^{+} + P\right) - \lambda N \tag{1.29}$$

where $\Delta$ is the pair gap, defined in section 1.4 and $P^{+}/P$ are the quasi-particle pair creation/annihilation operators. The term involving the Fermi surface, $-\lambda N$, is introduced in order to keep the total number of particles constant. This Hamiltonian is known as the Hartree-Fock-Bogolyubov Hamiltonian [Bengtsson 85] and calculations using this Hamiltonian yield *quasi-particle Routhians.*

## Signature and Parity

When the cranking Hamiltonian is employed, the $-\hbar\omega J_x$ term breaks the time-reversal symmetry. The only two remaining symmetries for a reflection-symmetric nucleus are *Parity*, $\pi$; which describes the symmetry under space reflection, and *Signature*, $\alpha$, which describes the invariance with respect to a rotation of 180° about the rotation axis. The eigenvalues of the $\mathcal{R}_x$ operator are given by

$$r = e^{-i\pi\alpha}, \tag{1.30}$$

which can be related to the angular momentum by

$$I = \alpha \; mod \; 2. \tag{1.31}$$

For even-mass nuclei $\alpha = 0$ or 1, and for odd-mass nuclei $\alpha = \pm\frac{1}{2}$. The parity assignments are $\pi = \pm$, depending on the behaviour of the single-particle wavefunction under space reflection. In the case of a reflection-asymmetric nucleus, both signature and parity are no longer good quantum numbers. A combination of both signature and parity known as *simplex* is, however, still a good quantum number. Simplex will be discussed further in the next chapter.

## Comparison of Experimental Data with Theoretical Routhians

In order to transform the experimental data to the rotating frame, the total experimental Routhian must first be defined. An expression for the total experimental Routhian is

$$E^{\omega}_{expt}(I) = \frac{1}{2}\left[E\left(I+1\right) + E\left(I-1\right)\right] - \omega\left(I\right) I_x\left(I\right) \tag{1.32}$$

where $I_x$ is the aligned angular momentum, given by the square-root term in the denominator of equation 1.7. The rotational frequency, $\omega$, is obtained from equation 1.8 and as mentioned previously, is approximately given by $E_\gamma/2$. Comparison between the total experimental Routhian and the theoretical quasi-particle Routhian requires the subtraction of an energy reference. A subtraction of this kind removes the contributions from the core, and leaves the experimental behaviour of the quasi-particles.

The experimental quasi-particle Routhian and alignment are defined by

$$e^{\omega}_{expt}(I) = E^{\omega}_{expt}(I) - E^{\omega}_{ref}(I) \tag{1.33}$$

and

$$i^{expt}_{x}(\omega) = I_x(\omega) - I^{ref}_{x}(\omega). \tag{1.34}$$

The energy reference of the core can be calculated using a variable moment of inertia fit to the low-lying transitions as a function of $\omega^2$;

$$\mathcal{J}^{(1)}_{ref}(\omega) = \mathcal{J}_0 + \omega^2 \mathcal{J}_1 \tag{1.35}$$

where $\mathcal{J}_0$ and $\mathcal{J}_1$ are known as the Harris parameters [Harris 65]. Following the discussion of moments of inertia in section 1.3, the aligned angular momentum reference is given by

$$I^{ref}_{x}(\omega) = \frac{1}{\hbar}\left(\mathcal{J}_0 + \omega^2 \mathcal{J}_1\right)\omega, \tag{1.36}$$

and the reference energy by

$$E^{ref}_{x}(\omega) = -\frac{1}{2}\omega^2 \mathcal{J}_0 - \frac{1}{4}\omega^4 \mathcal{J}_1 + \frac{1}{8}\frac{\hbar^2}{\mathcal{J}_0}. \tag{1.37}$$

The integration constant $\hbar^2/8\mathcal{J}_0$ is introduced to ensure that the ground state reference energy is set to zero. The experimental alignment $i_x(\omega)$ and Routhian $e^{\omega}_{expt}(\omega)$ can be compared directly with the theoretical alignment and Routhian.

# Chapter 2

# Reflection Asymmetry in Nuclei

The possibility that certain nuclei may have reflection-asymmetric shapes was realised in the 1950s, when low-lying negative parity states were observed in light-actinide nuclei [Asaro 53, Stephens 54, Stephens 55]. Since this time, much progress has been made both theoretically and experimentally in describing and observing the effects of the octupole interaction. In this chapter, some of the properties of reflection-asymmetric nuclei will be discussed, along with discussion of the regions of the nuclear chart which are susceptible to octupole deformation and the methods that can be used to populate them.

## 2.1 Introduction: Microscopic Origin of Octupole Correlations

The origins of octupole deformation can be understood through consideration of figure 2.1, which shows a schematic of the single-particle level energy sequence for a harmonic-oscillator potential. In certain cases, an orbit is lowered into the next lowest major shell by the $l^2$ and $l.s$ terms. These *intruder orbits*,$(l_{int}, j_{int})$, lie close in energy to orbits with $l = l_{int} - 3$ and $j = j_{int} - 3$, and the pairs of orbits with $\Delta l = \Delta j = 3$ can be strongly coupled by the octupole interaction. The most important couplings are $(g_{9/2} \rightarrow p_{3/2})$, $(h_{11/2} \rightarrow d_{5/2})$, $(i_{13/2} \rightarrow f_{7/2})$ and $(j_{15/2} \rightarrow g_{9/2})$;

these couplings are shown to the right of figure 2.1. Nuclei that have their Fermi surface in close proximity to these pairs of orbitals will be particularly susceptible to octupole correlation effects. The particle numbers close to these coupled orbits are 34, 56, 88 and 134, or just above closed shells. Nuclei with both proton and neutron numbers close to these values will exhibit stronger octupole correlations. It can also be seen in figure 2.1 that the octupole-driving $\Delta l = \Delta j = 3$ orbits are closer together for larger particle numbers, thus heavier nuclei should have the strongest octupole correlations.

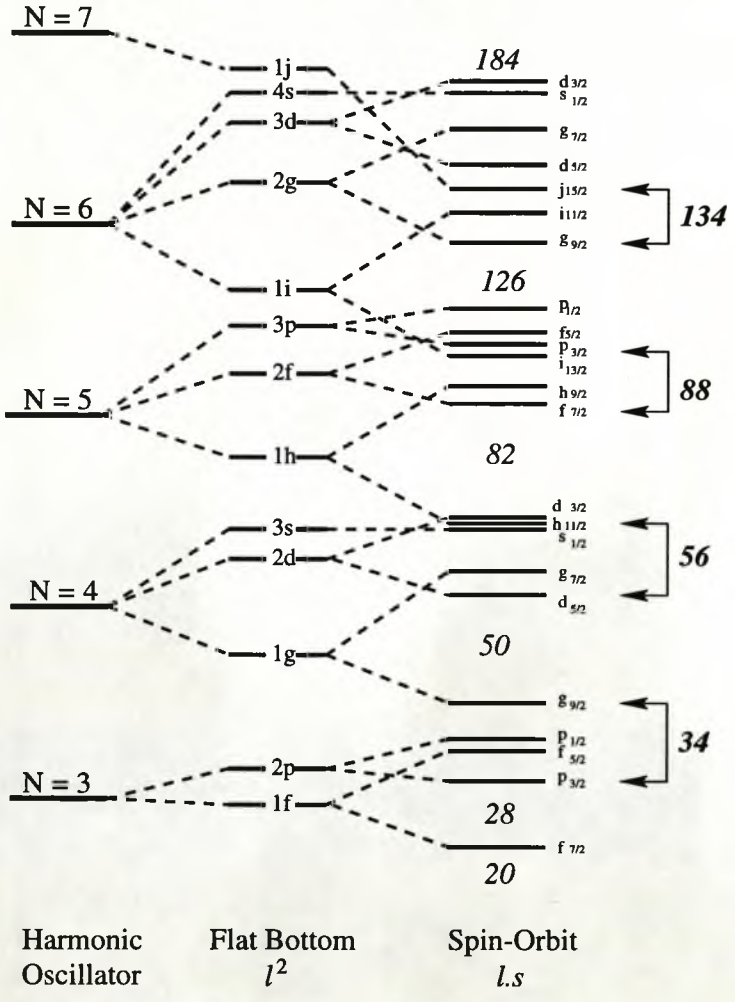


**Figure** 2.1: Ordering and splitting of energy levels due to the $l^2$ and $l.s$ terms added to the harmonic oscillator potential. The most important $\Delta l = \Delta j = 3$ couplings are also shown.

Since the single-particle level energies are dependent upon the form of the nuclear potential, calculations predicting the strength of the octupole correlations must also be dependent upon the potential. The effect of the choice of potential on the potential energy surface was calculated by Nazarewicz *et al.* [Nazarewicz 84] using the Strutinsky method. Some of the results obtained are shown in figure 2.2. The depth of the minimum in potential energy for non-zero $\beta_3$, relative to that obtained for a reflection-symmetric shape, is found to vary over quite a large range for different potentials, though the value at which the minimum occurs in $\beta_3$ is rather similar. The figure also highlights the fact that the heaviest nuclei have the strongest octupole correlations.

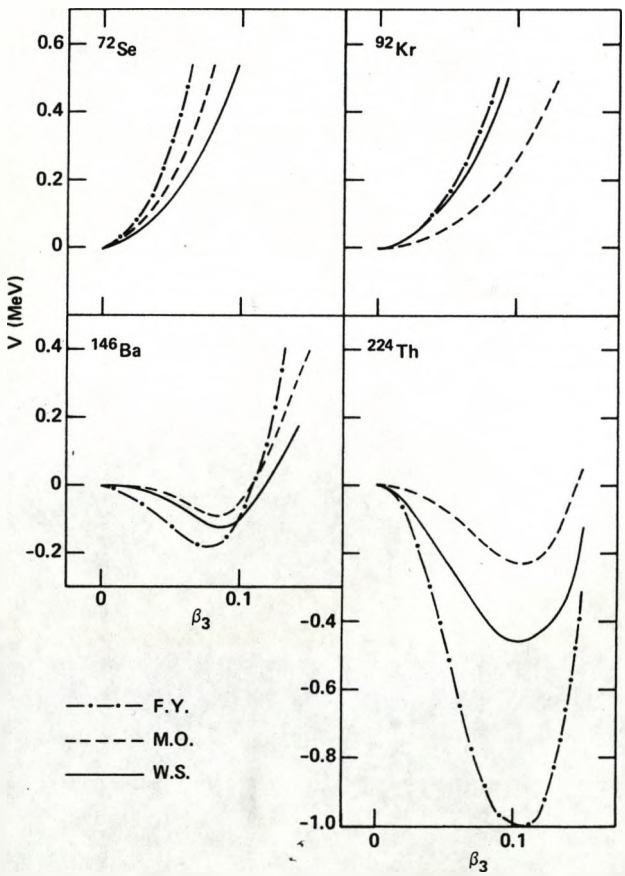


**Figure** 2.2: Plots of potential energy, V, against $\beta_3$, relative to a reflection-symmetric shape, calculated using the Strutinsky method for various potentials. The labels F.Y., M.O., and W.S. correspond to folded-Yukawa, modified oscillator and Woods-Saxon potentials, respectively. Taken from [Nazarewicz 84].

## 2.2 Spectroscopic Properties of Reflection-Asymmetric Nuclei

In this section, some of the experimental evidence for the existence of reflection asymmetry in nuclei will be discussed. Though the existence of reflection asymmetry in the nuclear ground state is difficult to prove conclusively, there is a wealth of experimental evidence that can be reproduced rather well by the inclusion of the octupole degree of freedom in theoretical calculations. The spectroscopic properties that are of relevance to this thesis will be discussed in detail; further properties are listed for completeness together with appropriate references at the end of this section.

### 2.2.1 Low-lying Negative-Parity States

As discussed in the introduction to this chapter, the observation of low-lying $1^-$ and $3^-$ states in isotopes of Ra and Th, populated via $\alpha$-decay, provided the first experimental evidence that some nuclei may possess reflection-asymmetric shapes. In a reflection-asymmetric molecule, such as HCl or $NH_3$, the positive- and negative-parity states are perfectly interleaved according to the $I(I+1)$ formula. The observed $1^-$ and $3^-$ states in the isotopes of Th and Ra remain higher in energy than the $2^+$ and $4^+$ states, respectively. This leads to the hypothesis that the nucleus is not rigidly octupole deformed and may fluctuate back to a reflection-symmetric shape. Figure 2.3 shows that the energies of the lowest-lying negative-parity states in the even-even isotopes of Rn, Ra, Th and U are well correlated to the predicted minima in the potential energy for non-zero $\beta_3$. The lowest-lying states are also very localised in $N$. As yet, in no nucleus has the lowest $1^-$ state been observed below the first $2^+$ state. There have been a number of attempts to describe the properties of the low-lying negative-parity states theoretically. Early calculations, using an octupole-vibrational model, were able to reproduce the energies of the negative-parity states in nuclei with $152 \leq A \leq 190$ [Neergård 70]. However, the model did not work as well in the actinide region, where the octupole correlations are stronger [Neergård 70a, Neergård 70b].

Further discussion of the theoretical attempts to describe the properties of the $1^-$ and $3^-$ states can be found along with references in the review article of Butler and Nazarewicz [Butler 96].

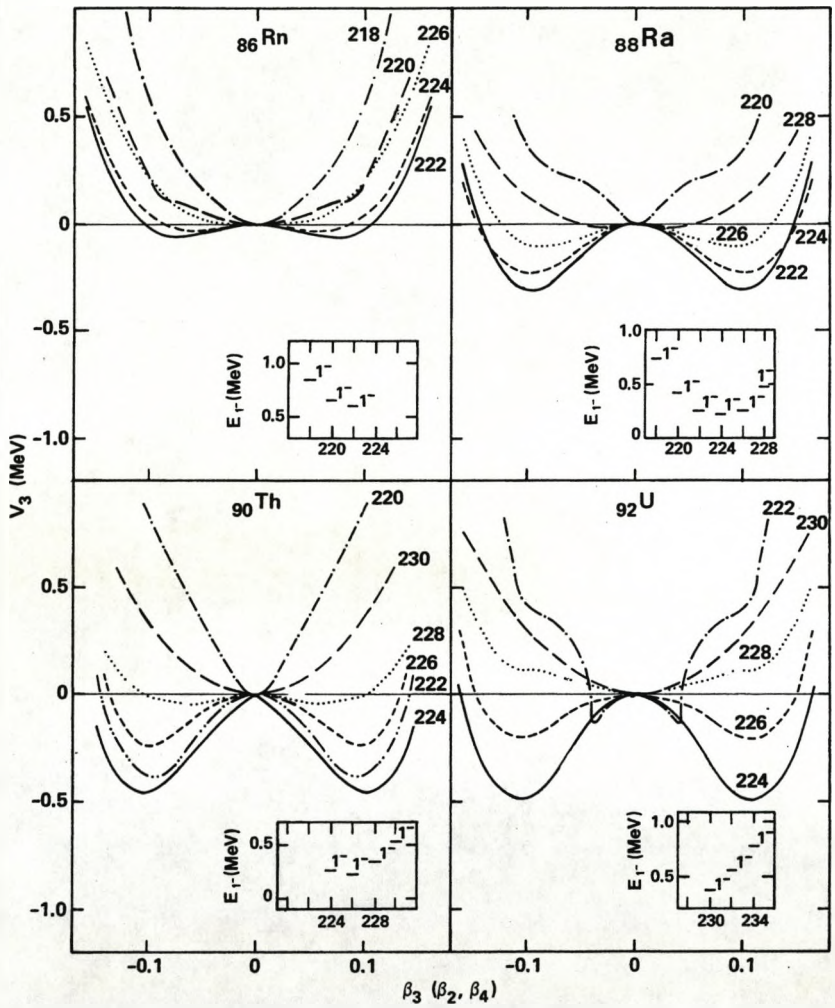


**Figure** 2.3: Octupole-deformation energy curves and lowest-lying negative parity states for Rn, Ra, Th, and U isotopes. Taken from Nazarewicz *et al.* [Nazarewicz 84].

## 2.2.2 Alternating-Parity Rotational Bands

Alternating-parity rotational bands, with interleaved states in the sequence $I^+$, $(I+1)^-, (I+2)^+, ...$, were first observed in the actinide region in $^{218}$Ra and $^{222}$Th [Fernández-Niello 82, Ward 83, Bonin 83]. Bands with similar structures were ob-

served earlier in medium-mass nuclei such as $^{152,150}$Gd and $^{150}$Sm [Zolnowski 75, Haenni 77, Sujkowski 77]. Since this observation, bands of this type have been observed in over 50 nuclei. It should be noted, however, that at low spin ($I < 5$) the bands are not interleaved and as stated earlier, in no nucleus does the $1^-$ state lie between the $0^+$ and $2^+$ states. This displacement can be understood through consideration of figure 2.4.

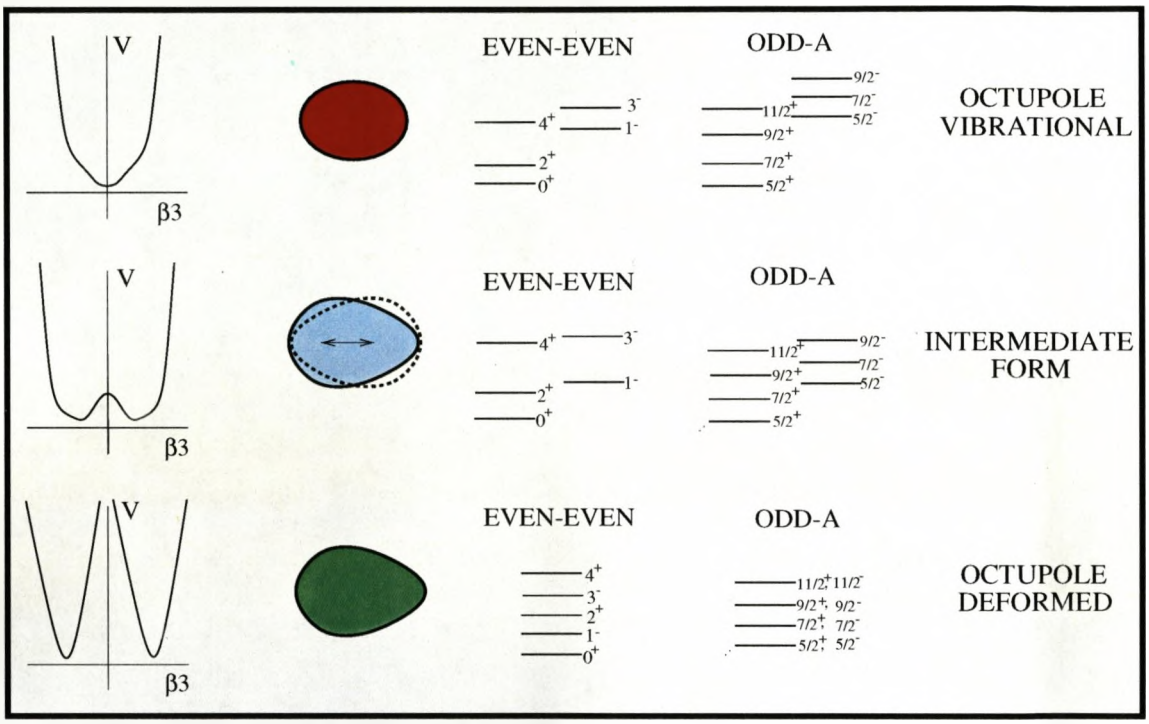


**Figure** 2.4: Plots of potential energy, V, as a function of $\beta_3$, and associated level schemes. The uppermost potential corresponds to a nucleus with a reflection-symmetric ground-state shape; the lowest to a static octupole-deformed shape. The centre potential is an intermediate between these two.

The figure shows three different plots of potential energy, V, against $\beta_3$. The uppermost potential corresponds to a nucleus with a reflection-symmetric shape in its ground state, but the nucleus can undergo fluctuations (vibrations) about this symmetric shape. If the vibration is of odd-multipolarity, then the nucleus can take on a reflection-asymmetric shape giving a $K^\pi = 0^-$ band at an energy of approximately

1 MeV. The lowermost potential corresponds to a nucleus with a permanent ground state octupole deformation. The potential barrier has two degenerate minima at $\pm\beta_3$ and rises to infinity at $\beta_3 = 0$. The nucleus cannot take on a reflection-symmetric shape. The spectrum for an even-mass nucleus is characterised by a set of perfectly interleaved states of alternating parity. The potential in the centre is intermediate between the two other potentials. There is a small ($< 0.5\ MeV$) potential barrier and the nucleus can tunnel through the barrier to the mirror image shape. This interaction results in the displacement of the two bands. In reality, the limit shown by the lowermost potential is never reached, and the barriers separating the two degenerate octupole minima are more like the one depicted in the centre. The displacement of a state from the midpoint of the two adjacent states with opposite parity, is known as the *parity splitting*, $\delta E$, and can be calculated by

$$\delta E = E(I)^- - \frac{1}{2}\left(E(I+1)^+ + E(I-1)^+\right). \tag{2.1}$$

It is observed that the parity splitting tends to zero at spins of around $10\hbar$, giving energy level schemes similar to that depicted in the lower part of figure 2.4. It seems that the rotational motion acts to stabilise the octupole deformation. Two explanations have been put forward to explain this phenomenon:(i) the octupole shape has weaker pairing correlations, which increases the moments of inertia and (ii) the rotational motion perturbs the single particle states of opposite parity, which brings the $\Delta l = \Delta j = 3$ orbitals closer together with increasing rotational frequency, thus enhancing the strength of the octupole correlations [Nazarewicz 87, Nazarewicz 92, Egido 90].

## Simplex

A reflection-asymmetric nucleus breaks the two symmetries of signature and parity discussed in section 1.7. The only remaining symmetry is a combination of these two, known as *simplex*, $s$ [Goodman 74, Nazarewicz 85]. Simplex is equivalent to reflection in a plane containing the symmetry axis, and is defined as the eigenvalue of the $S$ operator

$$S = \mathcal{P}\mathcal{R}^{-1}. \tag{2.2}$$

A rotational band with simplex $s$ has states of spin $I$ with alternating parity, related by [Bohr 75]

$$p = se^{-i\pi I}. \tag{2.3}$$

For a reflection-asymmetric nucleus with even mass, the spin and parity sequences are restricted to

$$s = +1, \quad I^\pi = 0^+, 1^-, 2^+, 3^-, ..., \tag{2.4}$$

$$s = -1, \quad I^\pi = 0^-, 1^+, 2^-, 3^+, ..., \tag{2.5}$$

and in the case of an odd mass nucleus

$$s = +i, \quad I^\pi = \tfrac{1}{2}^+, \tfrac{3}{2}^-, \tfrac{5}{2}^+, \tfrac{7}{2}^-, ..., \tag{2.6}$$

$$s = -i, \quad I^\pi = \tfrac{1}{2}^-, \tfrac{3}{2}^+, \tfrac{5}{2}^-, \tfrac{7}{2}^+, .... \tag{2.7}$$

## Rotational Alignment Properties

The behaviour of the aligned angular momentum (defined in section 1.7) as a function of rotational frequency can yield information concerning the structure of octupole nuclei. Cocks *et al.* [Cocks 97, Cocks 99] recently investigated the behaviour of several isotopes of Rn, Ra and Th at high spins using plots of the difference in aligned angular momentum, $\Delta i_x = i_x^- - i_x^+$, between the positive- and negative-parity bands. The value of $\Delta i_x$ was calculated by subtracting from the value of $i_x$ for each negative-parity state a smoothed interpolated value of $i_x$ for the positive-parity states at the same value of $\hbar\omega$. A plot of $\Delta i_x$ for $^{220}$Rn, $^{222}$Ra and $^{224}$Th created using data from references [Cocks 97, Ackermann 93] is shown in figure 4.17. For an octupole-vibrational nucleus, where the negative-parity states are described in terms of an octupole phonon coupled to the positive-parity states, the value of $\Delta i_x$ should be approximately three, as the octupole phonon quickly aligns with the rotational axis as the rotational frequency increases. For a nucleus with a stable octupole-deformed shape, the value of $\Delta i_x$ should be zero. This is due to the fact that for a stable octupole-deformed nucleus the energy of the $I^+$ to $I - 2^+$ transition should be equal to that for the $I + 1^-$ to $I - 1^-$ transition [Cocks 99].

### 2.2.3 Intrinsic Electric Dipole Moments

It is observed that electric dipole ($E1$) transitions are enhanced in nuclei that exhibit octupole deformation. For heavy nuclei, typical $E1$ transition rates are approximately $10^{-4}$ to $10^{-7}$ Weisskopf units (W.u.), but in octupole deformed nuclei, $E1$ rates can be on the order of $10^{-3}$ to $10^{-2}$ W.u. This enhancement was first described by Bohr and Mottelson [Bohr 57, Bohr 58a] and Strutinsky [Strutinsky 56] in terms of the macroscopic liquid-drop model. In this model, if the nucleus has an asymmetric shape, the protons will tend to move toward the pointed end of the pear shape where the curvature of the surface is the greatest. This is known as the lightning rod effect. The movement of the protons leads to a separation of the centre of charge from the centre of mass, giving an intrinsic electric dipole moment. The dipole moment is given (to first order) by

$$D_0 = C_{LD} A Z e \beta_2 \beta_3 \tag{2.8}$$

where $C_{LD}$ is approximately 0.0007 fm [Strutinsky 56]. The proportionality to $\beta_2\beta_3$ shows that the intrinsic dipole moment should be larger in nuclei that have well developed quadrupole and octupole deformation. This macroscopic model was refined using the droplet model [Myers 74, Dorso 86], which includes the effect of the neutron skin and nonuniformities in the nuclear density. Realistic calculations require the inclusion of microscopic shell effects; such calculations were first performed by Leander [Leander 86] and later extended by Butler and Nazarewicz to include higher-order deformations [Butler 91]. In this approach, the dipole moment is considered to be a sum of contributions from a macroscopic term, calculated using a liquid drop or droplet model, and microscopic shell correction term calculated using a deformed Woods-Saxon potential

$$\mathbf{D} = \mathbf{D}_{macro} + \mathbf{D}_{shell}. \tag{2.9}$$

It is found that the two contributions can be of similar magnitude, and may have the same or opposite sign; the two contributions can either enhance or diminish the dipole moment. Such cancellation effects mean that two nuclei with similar shapes may have different dipole moments, such that a correlation between the dipole mo-

ment and $\beta_3$ deformation is difficult to make. The calculations reproduced the trend of experimentally observed dipole moments in both the actinide and lanthanide regions; they were also able to reproduce the anomalously small dipole moment which was observed experimentally in $^{224}$Ra [Poynter 89a].

The dipole moment can be extracted from experimental data by measurement of the observed B($E1$)/B($E2$) branching ratios. The intrinsic electric dipole moment is related to the $E1$ transition probability by the rotational model formula (see section 3.6.2)

$$B\left(E1; I_i \rightarrow I_f\right) = \frac{3}{4\pi} e^2 D_0^2 \langle\, I_i K_i 10 \mid I_f K_f \,\rangle^2; \tag{2.10}$$

and the E2 transition probability to the transition quadrupole moment by

$$B\left(E2; I_i \rightarrow I_f\right) = \frac{5}{16\pi} e^2 Q_0^2 \langle\, I_i K_i 20 \mid I_f K_f \,\rangle^2. \tag{2.11}$$

These formulae provide a consistent method to extract intrinsic dipole moments from experimental data, although the assumption that the nuclei under investigation are good rotors may be questionable. The experimentally measured intrinsic dipole moments in several regions of the nuclear chart can be found in the review article of Butler and Nazarewicz [Butler 96].

### 2.2.4 Other Spectroscopic Properties

Some of the other spectroscopic properties that can be associated with octupole deformation are discussed briefly below.

- In odd-mass nuclei, there exist near degenerate pairs of rotational bands with the same spin values but opposite parity, known as *parity doublets*. These parity doublets, according to Chasman [Chasman 80], can occur when there are near-degenerate single particle orbitals of the same value of $\Omega$ and opposite parity. A signature of octupole deformation is a large B(E3) strength connecting the two bands [Dahlinger 88, Hughes 90];

- the $B(E3)$ transition strength in nuclei close to the predicted regions of octupole deformation is enhanced with respect to those measured elsewhere in the nuclear chart [Rohoziński 88, Spear 90, Raman 91];
- it is observed that alpha-decay probabilities to low-lying ($1^-$) states in Ra and Rn nuclei are enhanced, suggesting that there is a strengthening of the octupole correlations for the Ra and Rn nuclei with N$\leq$136 [Leander 84, Poynter 89];
- laser-spectroscopy measurements of the isotope shift $\delta\langle r^2\rangle^{A-1,A}$ across a series of isotopes have shown that there is an inversion or attenuation of the odd-even staggering observed in the majority of the nuclear chart. This inversion occurs in the regions of the nuclear chart where octupole deformation effects are expected to be the strongest [Borchers 87, Ahmad 88].

## 2.3 Regions of Octupole Deformation: Motivation to Study $^{226}$U

As indicated earlier in this chapter, nuclei which are particularly susceptible to octupole correlations have proton and neutron numbers close to 34, 56, 88 and 134; the strongest occurring for heavier nuclei. Thus nuclei in the lanthanide (Z$\simeq$54–65, N$\simeq$84–92) and actinide (Z$\simeq$86–92, N$\simeq$128–140) regions show evidence for the strongest octupole correlations. Since this work concentrates on the actinide region, the methods of population of these nuclei will be discussed here. Octupole correlation effects and methods of population in other regions of the nuclear chart are discussed in [Butler 96].

### 2.3.1 The Actinide Region

Nuclei in the actinide region are extremely difficult to populate experimentally. Until recently, little information existed concerning the high-spin states of many nuclei which were predicted to possess strong octupole correlations. Figure 2.5 depicts the

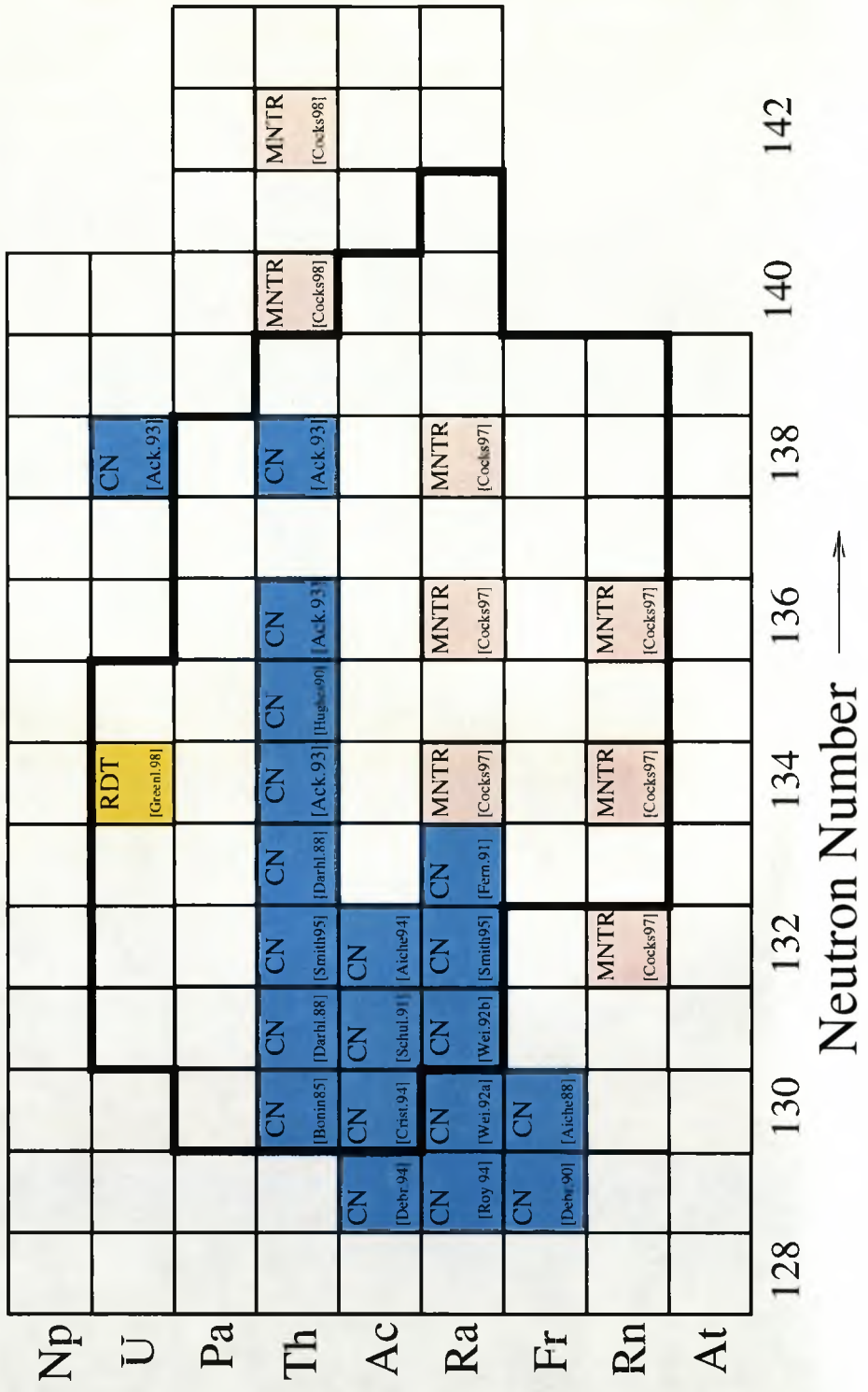


**Figure** 2.5: The actinide region of the nuclear chart. Alternating-parity bands have been observed in the nuclei which are shaded. The method of population and a recent reference is also indicated. These are: Compound Nucleus Reactions (CN), Multi-Nucleon Transfer Reactions (MNTR) and Recoil-Decay-Tagging (RDT). The bold line is the predicted boundary of octupole deformation [Sheline 87, Nazarewicz 84].

actinide region; the solid line represents the approximate boundary of predicted octupole deformation [Sheline 87, Nazarewicz 84]. The nuclei shaded in the figure are those in which characteristic alternating parity bands have been observed; those labelled CN can be populated through compound nucleus reactions, using $^{209}$Bi or $^{208}$Pb targets and beams such as $^{14}$C or $^{18}$O. The lack of stable isotopes above $^{209}$Bi means that many of the more neutron-rich isotopes of Rn and Ra cannot be populated in this manner. A recent development was the use of multi-nucleon transfer reactions to populate these nuclei, where the octupole correlations are predicted to be strong [Cocks 97]. Nuclei labelled MNTR in figure 2.5 were populated in this manner, using a $^{136}$Xe beam and $^{232}$Th target combination.

To date, only five nuclei in this region, $^{222,224,226}$Ra and $^{224,226}$Th, exhibit alignment properties expected for octupole deformation at sufficiently high rotational frequencies ($\hbar\omega > 0.2$ MeV) [Cocks 97, Cocks 99]. A long standing prediction by Nazarewicz *et al.* [Nazarewicz 84], based on Strutinsky-type potential energy calculations which employed a Woods-Saxon type potential with universal parameters (see figure 2.3), is that $^{224}$U and $^{226}$U should possess a deep minimum in the potential energy surface for non-zero $\beta_3$, with gains in potential energy of $\simeq 0.5$ and $\simeq 0.2$ MeV, respectively, relative to the reflection-symmetric shape.

These values are similar to those calculated for the isotopes of Ra and Th discussed above. Additional interest in these nuclei is generated by the prediction that $^{224,226}$U should possess large intrinsic dipole moments [Butler 91], comparable to that of $^{224}$Th, which has one of the largest measured $E1$ moments near to the ground state of the nuclei in this region of the nuclear chart [Ackermann 93].

The neutron-deficient uranium isotopes are difficult to study, partly because of strong fission competition and partly because the fusion-evaporation exit channel cross sections are dominated by the $\alpha xn$ channels to isotopes of thorium. The maximum cross section for the reaction $^{208}$Pb($^{22}$Ne,4n)$^{226}$U is approximately 6 $\mu b$ [Yeremin 94], compared with around 300 $\mu b$ for the $\alpha xn$ channels [Andreyev 89]. Some form of channel selection is therefore required in order to retrieve the events

of interest from the high background. Channel selection was achieved in this work through the recoil-decay-tagging (RDT) technique, which will be described in detail in the next chapter.

Although $^{224}$U would appear to be potentially a better case for octupole deformation, a number of experimental difficulties place the study of this nucleus at the extreme limit of sensitivity with currently available devices.

# Chapter 3

# Experimental Methods and the Recoil-Decay Tagging Technique

## 3.1 Introduction

As our knowledge of the nuclear chart is extended towards the proton drip line away from the valley of stability, new measurements become increasingly difficult, since the cross sections for populating these neutron-deficient nuclei are greatly reduced. The combination of small production cross sections and the competition from much more probable processes such as, in the case of heavy nuclei, fission, means that standard $\gamma$-ray spectroscopy techniques cannot be applied. The $\gamma$ rays of interest cannot be resolved from the large background of unwanted $\gamma$ rays.

Fortunately, however, many of the neutron-deficient nuclei above $Z \simeq 50$ decay by emitting characteristic charged particles (alphas, protons, $\beta$-delayed protons) from their ground state. The observation of these characteristic decays enables identification of a given isotope produced in a nuclear reaction. The combination of $\gamma$-ray spectroscopy and radioactive decay detection techniques thus allows weak reaction channels to be selected. This so-called technique of recoil-decay tagging was first employed in the late eighties at GSI, Darmstadt [Simon 86] and further developed at Daresbury Laboratory in the U.K. [Paul 95]. The experiments involve the coupling

of a high-efficiency germanium detector array with a recoil mass separator.

This chapter is devoted to the description of the experimental equipment and the techniques employed in recoil-decay tagging experiments carried out at the Accelerator Laboratory of the University of Jyväsklyä, Finland. Firstly, a brief outline of the principles involved is given, followed by more detailed discussion of RITU, the gas-filled recoil separator, and JUROSPHERE, an efficient array of germanium detectors.

## 3.2 Principles

In a recoil-decay tagging experiment, nuclear species are produced via fusion-evaporation reactions following bombardment of a thin target foil with ions accelerated to energies above the Coulomb barrier for the target/projectile pair. Some properties of fusion-evaporation reactions will be discussed in section 3.3. Prompt $\gamma$ rays are collected by an array of germanium detectors surrounding the target. The recoiling fusion-evaporation products are then separated magnetically from primary beam and fission products by a recoil mass separator, and implanted into a position-sensitive silicon detector at the focal plane of the device. The time, position and energy of the implants are recorded. The implanted nuclei then remain in the silicon detector, where they then decay. The characteristic decays are registered in the detector, and the time, position and energy of these are also recorded allowing correlation between an implant/decay pair. Once an implant has been identified by correlation with its subsequent decay in the silicon detector, the prompt $\gamma$ rays associated with the implant can then be recovered, since the $\gamma$ rays are recorded in coincidence with recoil implants, allowing for the flight time of the recoil through the separator. The power of the recoil-decay tagging technique is illustrated by figure 3.1. The figure shows the $\gamma$-ray spectra obtained using the JUROSPHERE array of germanium detectors coupled to the RITU gas-filled recoil separator, from the reaction $^{144}$Sm($^{36}$Ar,4n)$^{176}$Hg at a bombarding energy of 190 MeV [Muikku 98]. The cross section for this reaction is estimated to be approximately 5 $\mu$b, with a transmission efficiency for fusion-evaporation residues

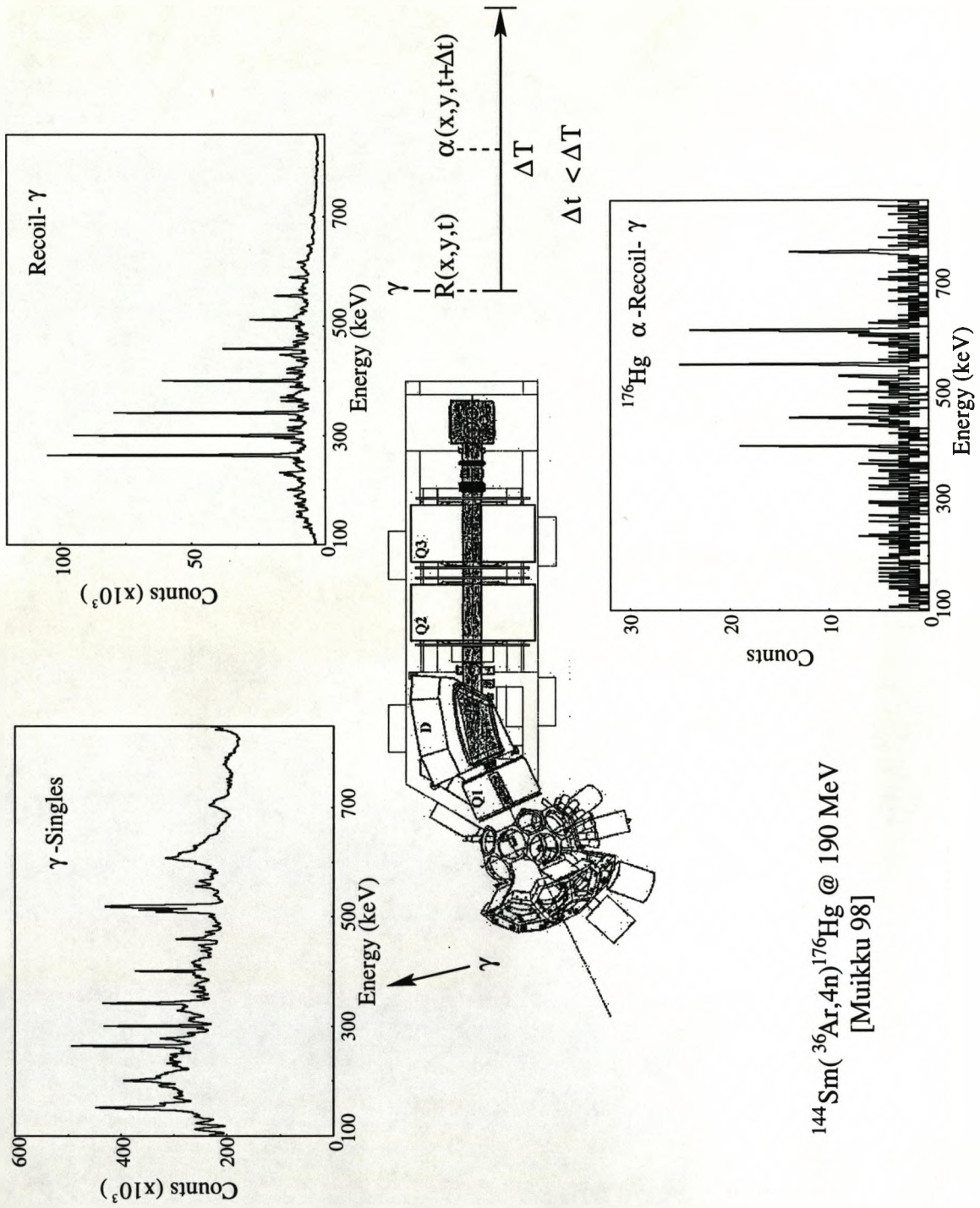


**Figure** 3.1: Schematic representation of the recoil-decay tagging technique. Prompt $\gamma$ rays produced at the target are detected by the JUROSPHERE array of Ge detectors, and the fusion-evaporation products are separated in flight using the RITU device. The products are then implanted into a Si-strip detector at the focal plane. Subsequent decays can then be correlated with the corresponding implant, allowing extraction of the $\gamma$ rays of interest.

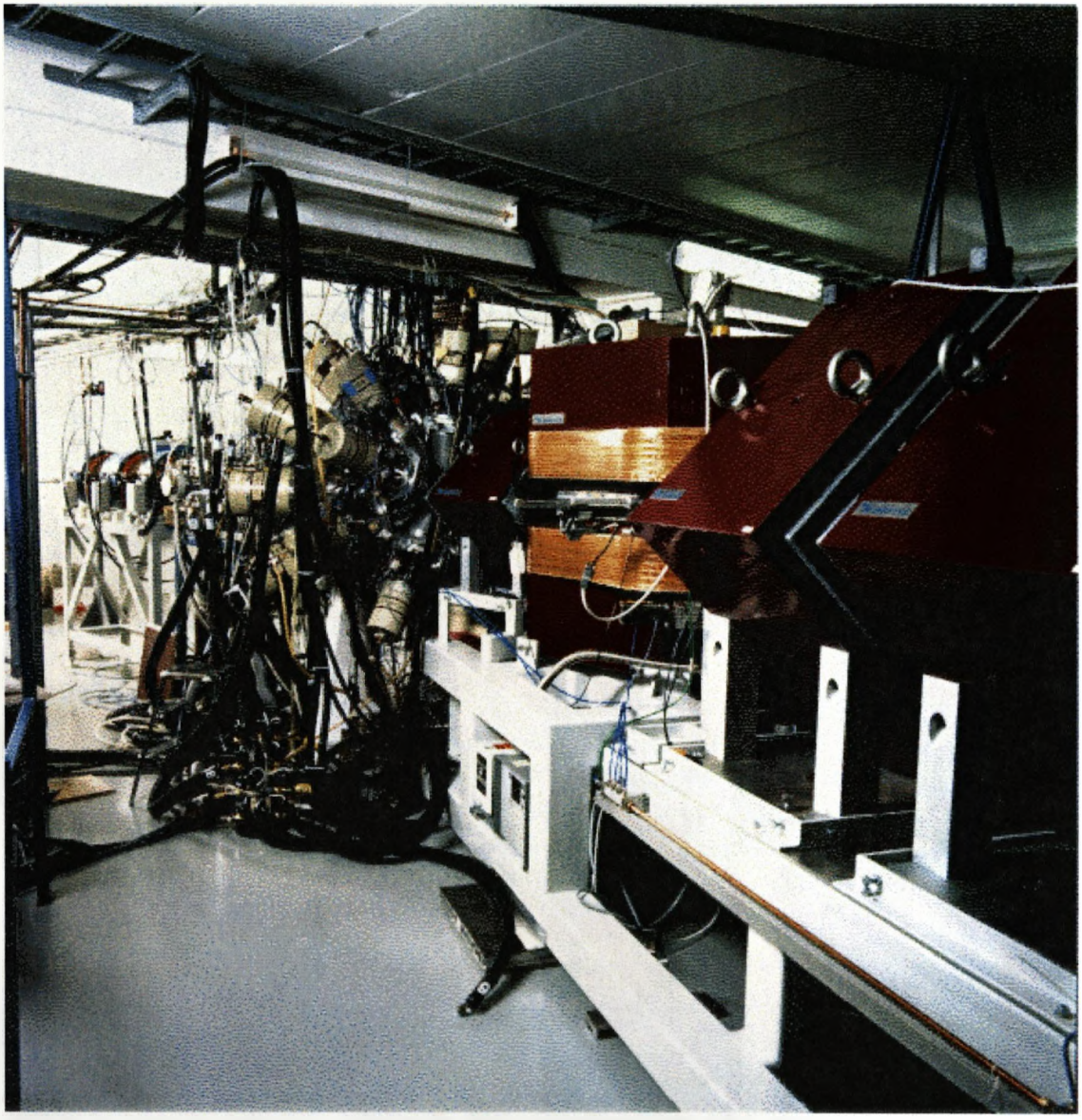

**Figure** 3.2: Photograph of the RITU plus JUROSPHERE device used in the present work.

through the RITU device of approximately 27%. The spectrum labelled "$\gamma$-singles" is the total spectrum of prompt $\gamma$ rays collected in the JUROSPHERE array. By demanding that an observed $\gamma$ ray is in coincidence with a fusion-evaporation residue detected in the RITU silicon-strip detector, the spectrum labelled "Recoil-$\gamma$" is obtained. This spectrum is dominated by transitions in the ground-state band of $^{176}$Pt, which is the major fusion-evaporation channel produced in the reaction. Fusion-evaporation residues from other reaction channels also contribute to this spectrum. In order to isolate the $\gamma$ rays that are associated with $^{176}$Hg residues, a recoil-$\alpha$ correlation is performed. Here, two successive events are selected; the first corresponding to a recoil implant in the Si-strip detector at a position (x,y) and at time, t. A search is made for subsequent events with an energy corresponding to that of the $^{176}$Hg $\alpha$-decay, at the same (x,y) position in the detector, within a time $\Delta$T. This time, known as the *search time* (in this case 100 ms), normally corresponds to around three half-lives of the decay of interest. The resulting spectrum is labelled "$\alpha$-Recoil-$\gamma$". Here, only transitions in $^{176}$Hg are observed. It can also be seen that these $\gamma$ rays are buried in the background of the recoil-$\gamma$ spectrum. Thus the recoil-decay-tagging technique allows weak reaction channels to be selected from an extremely large background.

## 3.3 Heavy-Ion Fusion-Evaporation Reactions

As mentioned in the previous section, the nuclei studied in this work were produced via heavy-ion fusion-evaporation reactions. In such a reaction, the target and projectile nuclei fuse together, forming a *compound nucleus*. This idea of compound nucleus formation was first suggested by Niels Bohr in 1936 [Bohr 36]. In order that the compound nucleus be formed, two criteria must be satisfied:

- the projectile must have an energy large enough to overcome the Coulomb barrier, given by equation 3.1

$$E_{CB}(MeV) = \frac{1.44 Z_1 Z_2}{1.16\left(A_1^{1/3} + A_2^{1/3} + 2\right)} \tag{3.1}$$

where $Z_1$, $A_1$ are the atomic number and mass of the projectile and $Z_2$, $A_2$ are the atomic number and mass number of the target;

- the angular momentum transfer should be small, so that the centrifugal repulsion caused by the rapid rotation of the nucleus does not overcome the short-range attraction of the nuclear force.

### 3.3.1 Decay of the Compound Nucleus

When formed, the compound nucleus will be in a state of extreme excitation. For the reactions used in this work, the compound nucleus typically has an excitation energy of around 40 MeV, with a maximum angular momentum of around 25-35 $\hbar$. The compound nucleus loses this excitation energy in various ways, shown schematically for a four neutron evaporation channel in figure 3.3. For the heavy nuclei studied here, the most probable decay mode of the compound nucleus is fission. This is due to the fact that the nucleus is no longer stable against the centrifugal repulsion mentioned above. If the compound nucleus does not undergo fission, the majority of the excitation energy is removed by particle emission (protons, neutrons, alpha particles). Charged particle evaporation (protons, alpha particles) is normally suppressed by the Coulomb barrier, but for the neutron deficient nuclei produced in this work, alpha particle evaporation along with neutron evaporation forms a large part of the fusion-evaporation cross section. The evaporation of particles carries away large amounts of excitation energy (at least 8–10 MeV), but a small amount of angular momentum. Thus the evaporation of particles gives a steep descent towards the ground state, as shown in figure 3.3.

When the excitation energy is below the particle evaporation threshold (approximately 8 MeV above the yrast line) the nucleus continues to de-excite through $\gamma$-ray emission. The nucleus is still relatively excited, and decays by emission of *statistical* or *cooling* $\gamma$ rays. These are usually high energy dipole transitions, carrying away large amounts of excitation energy, but again very little angular momentum. These $\gamma$ rays are normally not resolved in a $\gamma$-ray spectroscopy experiment.

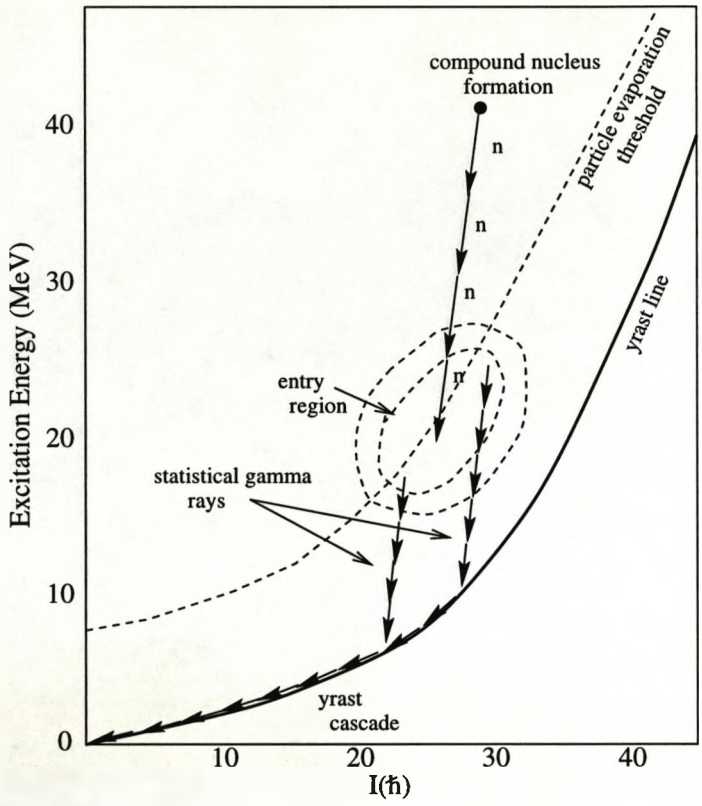


**Figure** 3.3: A schematic of the decay of the compound nucleus. In this example, four neutrons are first emitted, carrying away a large amount of excitation energy, but little angular momentum. When below the particle evaporation threshold, de-excitation continues to the ground state through $\gamma$-ray emission.

As the cooled nucleus approaches the yrast region, $\gamma$-ray emission proceeds through transitions of lower energy, carrying more angular momentum, to the ground state. It is these *yrast-like* transitions that are of particular interest to the $\gamma$-ray spectroscopist, since they carry enough intensity to be isolated in a $\gamma$-ray spectrum, and can reveal the properties of the nucleus being studied.

## 3.4 Detection of Nuclear Radiations

The majority of detectors used in nuclear physics today operate in a similar manner. The basic principle is that radiation enters the detector, interacts with the atomic

electrons of the detector material and then releases them from their atomic orbits. These electrons can then be swept out of the detector with the application of an external electric field, creating an electrical pulse that can then be processed by electronic devices. The design and choice of material for a particular detector is dependent upon its application. For instance, if the energy of the incident radiation has to be measured, the detector is required to produce an output signal which is proportional to the incident energy. Also, the incident radiation should produce a large number of electrons, so that small losses or statistical fluctuations do not greatly affect the ability to measure the energy. Another important factor here is the physical size of the detector. If we wish to accurately measure the incident energy, then all this energy must be deposited in the detector. The range of the incident radiation is dependent upon the detector material and the type of radiation.

The interaction of the various types of nuclear radiation with matter will be discussed in the following sections.

## 3.5 Alpha Spectroscopy

### 3.5.1 Theory of Alpha Decay

The majority of isotopes of the elements above and some of the neutron-deficient isotopes below Pb decay by emission of $\alpha$-particles. The monoenergetic nature of the emitted $\alpha$-particles allows nuclear structure information to be deduced through spectroscopic measurements. The $\alpha$-decay process can be represented by

$$ {}^{A}_{Z}X_{N} \rightarrow {}^{A-4}_{Z-2}Y_{N-2} + \alpha, \tag{3.2} $$

where $X$ and $Y$ are known as the mother and daughter nuclides, respectively. Conservation of energy and linear momentum leads to the definition of the $\alpha$-decay Q-value,

$$ Q_{\alpha} = (m_X - m_Y - m_{^4He})\, c^2 = T_Y + T_{\alpha} \tag{3.3} $$

where $m_X$, $m_Y$ and $m_{^4He}$ are the atomic masses of the mother nucleus, daughter nucleus and the helium atom, respectively. $T_Y$ and $T_{\alpha}$ are the kinetic energies of the

daughter nucleus and $\alpha$-particle. An additional screening correction to $Q_\alpha$ may be added to account for influence of the electron cloud on the emitted $\alpha$ particle

$$E_{scr} = \left(65.3Z^{7/5} - 80Z^{2/5}\right) eV \tag{3.4}$$

where $Z$ is the proton number of the daughter nucleus. This correction is at most around 47 keV ($Z$=110) and is often neglected. The $\alpha$-decay process can occur spontaneously if $Q_\alpha > 0$, though the effect of the Coulomb barrier means that the rate of $\alpha$ emission does not become appreciable until the value of $Q_\alpha$ rises to several MeV. The probability per second that a nucleus will decay, $\lambda$, is known as the *decay constant*, and is related to the half-life, $T_{1/2}$, by

$$\lambda = \frac{ln2}{T_{1/2}}. \tag{3.5}$$

A particular isotope may emit $\alpha$-particles of more than one energy, if excited states in the daughter nucleus are populated by the decay. Each decay to a particular state has a different decay constant, known as the partial decay constant $\lambda_i$. The ratio of the partial to total decay constant gives the $\alpha$-decay branching ratio, $b_\alpha$, and the partial half-life of a particular decay is given by

$$\tau_{1/2} = \frac{ln2}{\lambda_i} = \frac{T_{1/2}}{b_\alpha}. \tag{3.6}$$

The range of $\alpha$-decay half-lives is extremely large, over twenty orders of magnitude, and the half-life is closely related to the $\alpha$-decay energy. In simple terms the higher the $\alpha$-decay energy, the shorter the $\alpha$-decay half-life. Geiger and Nuttall [Geiger 11] showed that a reasonable straight line is obtained if the logarithm of the half-life is plotted against the logarithm of the range of $\alpha$-particles in air. The range is related to the energy, and thus the $\alpha$-decay Q-value. The relationship is then given by

$$\tau_{1/2} = a + \frac{b}{\sqrt{Q_\alpha}} \tag{3.7}$$

where $a$ and $b$ are empirically determined constants that are different for each element. A Geiger-Nuttall plot for even-even $\alpha$-decaying isotopes is shown in figure 3.4; a

similar plot produced in the course of this work is shown in figure 5.7. It can be seen that several points lie some distance from the curves to which they are joined by a line. These decays either involve a closed shell nucleus, or are to an excited state in the daughter nucleus. The ratio of the actual half-life to that predicted by the empirical line is known as the *hindrance factor*. Hindrance factors are discussed further below.

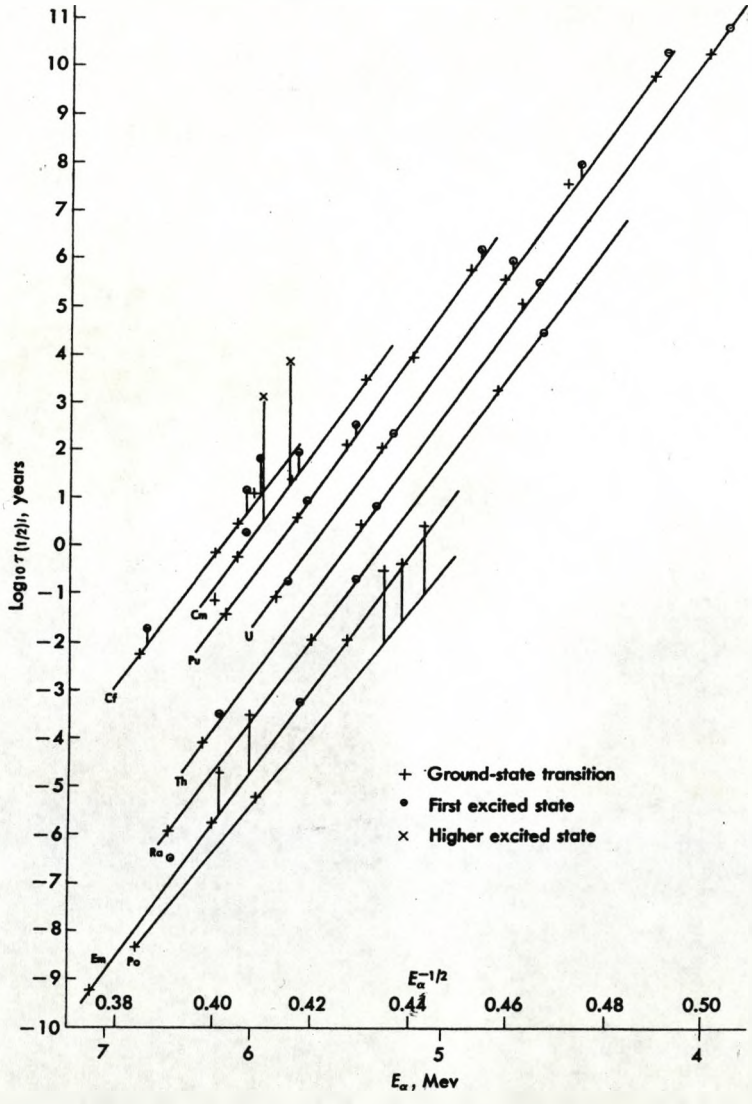


**Figure** 3.4: A Geiger-Nuttall plot for even-even $\alpha$-decaying isotopes. Taken from [Preston 62]

### One-body Model

The one-body model of $\alpha$-decay assumes that the $\alpha$-particle is preformed in the nucleus, and confined to the nuclear interior by the Coulomb potential barrier. In the classical picture, if the kinetic energy of the $\alpha$-particle is less than the potential energy represented by the barrier height, the $\alpha$-particle cannot leave the nucleus. In the quantum-mechanical picture, however, there is a finite probability that the $\alpha$-particle will tunnel through the barrier and leave the nucleus. This treatment of the $\alpha$-decay process was one of the first successful applications of quantum theory to nuclear physics, and was presented independently by Gamow [Gamow 28] and Condon and Gurney [Condon 28]. The $\alpha$-decay constant is then a product of the frequency of collisions with the barrier, or "knocking frequency", and the barrier penetration probability, $P$

$$\lambda = \left(\frac{v_\alpha}{2R_i}\right) P, \tag{3.8}$$

where $v_\alpha$ is the velocity of the $\alpha$-particle in the nucleus. The barrier penetration probability, $P$, can be calculated from the WKB integral

$$P = exp\left[-2\int_{R_i}^{R_o}\left[\left(\frac{2M_\alpha}{\hbar^2}\right)\left(V(r) + \frac{2Ze^2}{4\pi\epsilon_0 r} + \frac{\hbar^2}{2mr^2}l(l+1) - Q_\alpha\right)\right]^{1/2} dr\right], \tag{3.9}$$

where $R_i$ and $R_o$ are the inner and outer turning points for a classical $\alpha$-particle trajectory, $V(r)$ is the nuclear potential, $Ze$ is the charge of the daughter nucleus and $l$ is the orbital angular momentum carried by the emitted $\alpha$-particle. The angular momentum carried by the $\alpha$-particle is in the range $(I_i + I_f) < l < (|I_i - I_f|)$, where $I_i$ and $I_f$ are the total angular momenta of the initial and final nuclear states, respectively. The term $(\hbar^2 l(l+1)/2mr^2)$ in equation 3.9 represents the additional centrifugal contribution to the barrier that acts to reduce the tunnelling probability if the angular momentum carried by the $\alpha$-particle is non-zero. Decays involving a change in angular momentum can be strongly hindered by the centrifugal barrier.

### Reduced Widths and Hindrance Factors

As mentioned earlier, this approach assumes that the $\alpha$-particle is preformed in the

nucleus. The probability of forming an $\alpha$-particle in a particular nucleus is, however, dependent upon the nuclear structure. This preformation probability may result in a reduction in the $\alpha$-decay probability. The preformation probability is also known as the reduced $\alpha$-decay width or spectroscopic factor. It is possible to calculate the reduced $\alpha$-decay width using shell model wave-functions. Such calculations were first performed by Mang [Mang 57, Mang 60], who hypothesised that the probability of formation of the $\alpha$-particle is proportional to the overlap of the final state wavefunctions with those of the initial state. Another method to obtain information concerning the reduced $\alpha$-decay width is that given by Rasmussen [Rasmussen 59]. Here, the reduced $\alpha$-decay width, $\delta^2$ is given by

$$\delta^2 = \frac{\lambda h}{P} \tag{3.10}$$

where $h$ is Planck's constant. The barrier penetrability, $P$, is evaluated through numerical integration of equation 3.9. The values thus obtained may then be normalized to that for the ground state $\alpha$-decay of $^{212}$Po, or expressed in keV.
The hindrance factor for decays to excited states can be defined as

$$HF = \frac{\delta^2_{g.s.}}{\delta^2_{exc.}}, \tag{3.11}$$

where $\delta^2_{g.s.}$ and $\delta^2_{exc.}$ are the reduced $\alpha$-decay widths for the ground state to ground state and ground state to excited state decays, respectively. This method also considers any hindrance that may occur due to centrifugal effects, and the obtained hindrance factor can yield information on the difference in nuclear structure of the initial and final states.

### 3.5.2 Recoil Separators

Over the past 20 years, recoil separator devices have been used to good effect in the pursuit of new heavy elements and neutron-deficient isotopes. The performance and design of these is mainly governed by two aspects: (i) the need for maximum possible transmission of fusion-evaporation products and (ii) high mass resolution. In practice,

a compromise between these two is taken. For instance, the Fragment Mass Analyser (FMA) at the Argonne National Laboratory [Davids 89], is a device with excellent mass resolution (typically one part in 300) but suffers from low transmission efficiency ($\leq$ 10 to 20%). The poor efficiency in separators of this type, which operate with the field region in a vacuum, is mainly due to the fact that only two or three charge states of the recoils can be collected, whilst the recoiling nuclei have a wide distribution of charge states. In order to overcome this problem, the field region can be filled with a dilute gas such as helium, an idea proposed by Cohen and Fulmer [Cohen 58]. The effect of filling the field region with gas is shown schematically in figure 3.5. In this

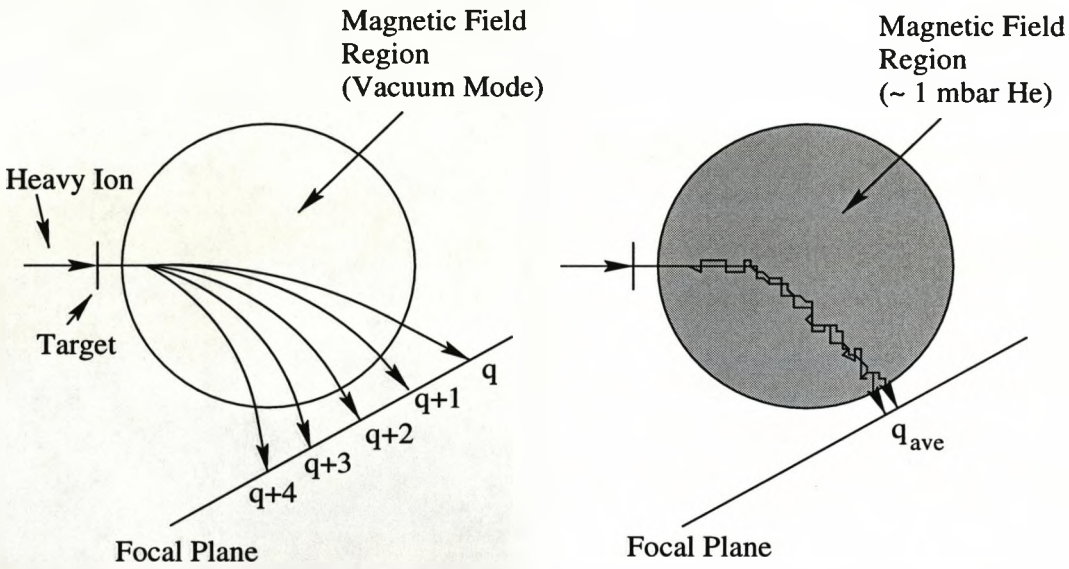


**Figure** 3.5: The effect of filling the field region with dilute gas in a recoil separator.

case, multiple scattering of the recoiling ions in the dilute gas means that they will follow a trajectory through the separator corresponding to that of $q_{ave}$, the average charge state of the ions exiting the target, provided that the mean free path of the recoils between charge changing collisions is small compared to the flight distance through the separator. The acceptance of essentially all charge states thus leads to much higher transmission. The trajectory of the primary beam is usually sufficiently different from that of the recoiling nuclei, giving suppression factors on the order of $10^{-12}$–$10^{-15}$.

The first recoil separator of this type to be constructed was SASSY [Ghiorso 88] at the Lawerence Berkeley National Laboratory, California. The performance of gas-filled recoil separators can be described (to first order[1]) by the simple formula for magnetic rigidity

$$B\rho = \frac{mv}{q_{ave}} = \frac{mv}{[(v/v_0)\, eZ^{1/3}]} = \frac{0.0227A}{Z^{1/3}} Tm \tag{3.12}$$

where $A$, $Z$ and $v$ are the mass number, proton number and velocity of the recoiling ion, respectively, and $v_0$ is the Bohr velocity $= 1/137c$ m/s. The expression $q_{ave} = (v/v_0)eZ^{1/3}$ is obtained using the Thomas-Fermi model of the atom. In can be seen that $q_{ave}$ is proportional to the velocity of the ions, thus charge and velocity focusing is achieved and the device acts as a mass separator. The mass resolution for these devices is typically around 10%. The design of gas-filled recoil separators is normally such that primary beam is separated immediately behind the target. This is in order to minimise the widening of the beam as it travels through the separator. To achieve this, a dipole bending magnet is placed behind the target, followed by two quadrupole magnets which focus the ion beam into the focal plane. This simple design is used in SASSY [Ghiorso 88], and the JINR device in Dubna, Russia [Oganessian 91].

### 3.5.3 The RITU Gas-filled Recoil Separator

The gas-filled recoil separator RITU (Recoil Ion Transport Unit) [Leino 95] was constructed at the Physics Department of the University of Jyväskylä in 1992-3. A schematic of the RITU device is shown in figure 3.6.

RITU differs from most gas-filled recoil separators in that it has an additional strongly vertical-focusing quadrupole magnet in front of the dipole magnet. This leads to better matching of the recoil ion beam to the angular acceptance of the

[1]Equation 3.12 shows that to first order $B\rho$ is independent of the velocity and of the initial charge state distribution of the recoiling ions. However, it has been shown that the average charge of the recoiling ion is determined by the ions' atomic shell structure. It is also known that, contrary to equation 3.12, there is a velocity dependence of $B\rho$. Further discussion of these higher-order effects can be found in reference [Ghiorso 88].

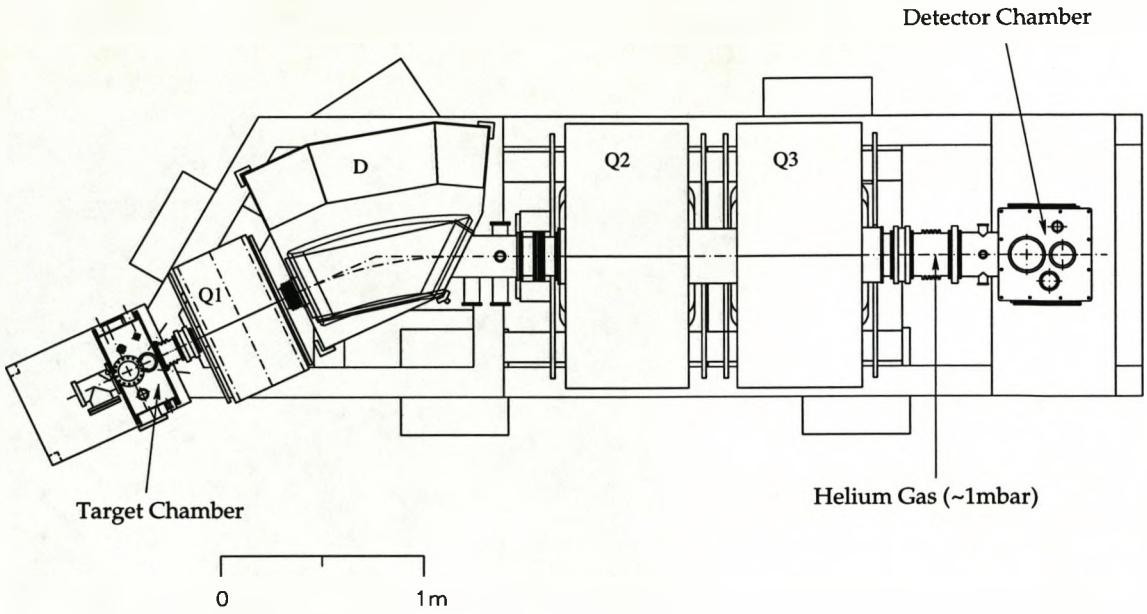


**Figure** 3.6: The RITU gas-filled recoil separator.

dipole magnet, and gives an increase in transmission efficiency of approximately 30%. An additional benefit is improved mass resolution when the device is operated in vacuum mode ($A/\Delta A \simeq 100$). The magnetic field region is filled with a constant flow of helium gas, regulated by a mass flow valve such that the whole gas volume is changed every thirty minutes, in order to keep impurities to a minimum. The interplay between charge state focusing and multiple scattering means that as the gas pressure is varied, an optimum is reached where the image size at the focal plane is minimised. Typical pressures used are 0.5 to 3 mbar. The gas-filled region is separated from the high beam-line vacuum by thin (0.1 to 1 mg/cm$^2$) carbon or nickel foils. It should be noted that in $\gamma$-ray spectroscopy measurements, the separating foil should be kept as thin as possible, to avoid a contribution to the $\gamma$-ray background.

RITU was originally designed in order to attempt the study of heavy elements, thus the device is particularly suited to studies of nuclei populated with asymmetric reactions ($^{22}$Ne + $^{208}$Pb, for example). When the reaction used is symmetric (e.g. $^{58}$Ni + $^{58}$Ni), the magnetic rigidity of the beam is close to that of the fusion-evaporation products, and the primary beam suppression factor is reduced. Substantial reduc-

tion in primary beam suppression means that the focal plane Si detector may be destroyed. The transmission efficiency is influenced strongly by angular, charge state and velocity dispersions, which act to broaden the angular distribution and lateral spread of the recoiling ions. A quantitative analysis of the factors which contribute to these dispersions can be found in [Uusitalo 96].

### 3.5.4 Interaction of Heavy Charged Particles with Matter

The interaction of heavy charged particles in matter is primarily governed by the long range Coulomb force. In a simplistic picture, it can be said that since the nucleus occupies only around $10^{-15}$ of the atomic volume, interaction with atomic electrons is around $10^{15}$ times more likely than interaction with the nucleus. The effects of interaction with the nucleus only become important for high $Z$ and/or low energy ($\leq$ 1 MeV/u) ions. The energy loss of an $\alpha$ particle in a single head-on collision with an atomic electron is very small when compared with its kinetic energy. For example, the maximum energy loss of a 5 MeV $\alpha$ particle is approximately 3 keV in a head-on collision, and less than this if the collision is glancing. Therefore, it can be seen that the $\alpha$ particle must endure many such collisions before depositing its full energy in the detector. As the Coulomb force acts over a large range, the heavy ion will feel the effect of many atomic electrons simultaneously, and the energy loss will thus be continuous. Also of importance is the fact that the energy required to ionize an atom is approximately 10 eV, and that liberated electrons with kinetic energies in the keV range also ionize atoms.

These concepts are elegantly contained in the Bethe-Bloch formula, which describes the energy loss per unit length for a charged particle in an absorbing medium

$$-\frac{dT}{dx} = \frac{4\pi z^2 \alpha^2 (\hbar c)^2}{m_e v^2} N_a B, \; B = Z_a \left[ \ln \left( \frac{2 m_e v^2}{I\left(1 - v^2/c^2\right)} \right) - \frac{v^2}{c^2} \right]. \tag{3.13}$$

Here $v$ and $z$ are the velocity and charge state of the incident ion, $N_a$ and $Z_a$ are the number density and atomic number of the absorber material, $m_e$ is the rest mass of the electron and $\alpha$ is the fine structure constant. The parameter $I$ is a

representation of the average excitation energy of the atomic electrons, incorporating all excitation and ionization processes, and is determined empirically. It can be seen from the above expression that the stopping power is greatest for high-density, high-$Z$ materials, and for ions in higher charge states.

### 3.5.5 The RITU Focal-Plane Si-Strip Detector

Since the RITU recoil separator has insufficient mass resolution to unambiguously identify a given isotope, the nuclei implanted must be identified by another means. Often such identification can be made using time-of-flight and energy loss techniques. In the present work, nuclei are identified through correlated alpha-decay chains. Such correlations are possible using a position sensitive silicon-strip detector.

The detector at the focal plane of the RITU device is a 16-element strip detector, measuring 80 mm in the horizontal direction by 35 mm in the vertical direction. The detector works in much the same manner as the Ge detectors described in section 3.6.4. The p-type contact is formed by implantation of boron atoms into the n-type silicon. The bias is supplied using conventional batteries, and the detector is fully depleted at around $-40$ V. At the edges of the strips are aluminium contacts, which are connected to the printed circuit board by gold-plated springs. Each strip is 5 mm wide in the horizontal direction. Position sensitivity in the vertical direction is attained through charge division. This is possible because the detector is fabricated with a resistive layer. A signal is taken from both ends of an individual strip, and the two signals are summed to obtain the total energy deposited in the detector. Because of the resistive layer, the signal obtained from one end of the detector is proportional to the vertical position at which the event occurred. If the signal from one end of the detector is divided by the total energy deposited in the detector, the vertical position of the event can be determined.

## 3.6 Gamma-Ray Spectroscopy

### 3.6.1 Interaction of Gamma Rays with Matter

The total attenuation coefficient for a $\gamma$- or X-ray travelling through a medium has contributions from scattering, photoelectric absorption and pair production processes. For the purposes of this work, photonuclear and other such small effects are neglected. These three main processes are discussed below.

#### Compton Scattering

Figure 3.7 schematically shows the process of Compton scattering. In this case,

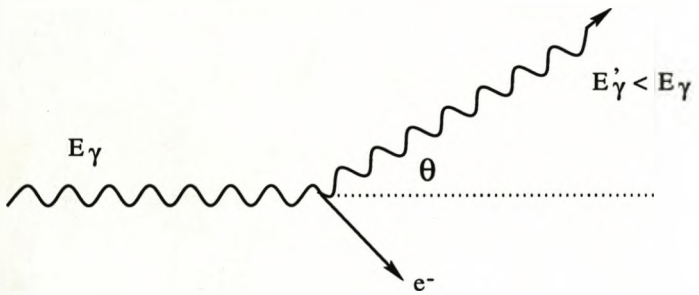


**Figure** 3.7: The process of Compton scattering.

an incident $\gamma$ ray scatters from an outer shell electron in the absorber material at an angle $\theta$, and some of the $\gamma$-ray energy is imparted to the electron. Conservation of energy and momentum leads us to the following expression for the energy of the scattered photon:

$$E'_\gamma = \frac{E_\gamma}{1 + (E_\gamma / m_0 c^2)\,(1 - \cos\theta)}, \tag{3.14}$$

where $E_\gamma$ is the incident photon energy, $E'_\gamma$ is the energy of the scattered photon, $\theta$ is the scattering angle and $m_0 c^2$ is the electron rest mass energy. The kinetic energy of the electron after the collision is given by

$$T_e = E_\gamma - E'_\gamma = \frac{E_\gamma^2\,(1 - \cos\theta)}{m_0 c^2 + E_\gamma\,(1 - \cos\theta)}. \tag{3.15}$$

It can be seen that, since all scattering angles are possible, the electron energy ranges from zero for $\theta = 0°$ to $2E_\gamma^2/(m_0 c^2 + 2E_\gamma)$ for $\theta = 180°$, and that the photon never

loses the whole of its energy in any one collision. The scattered photon can then continue through the absorber and interact again or scatter out of the absorber material completely. This process, where the scattered photon escapes, is very important for the $\gamma$-ray spectroscopist. If the full energy of the incident photon is not absorbed in the detector, then there is a continuous background in the energy spectrum, known as the Compton continuum. This continuum extends up to an energy corresponding to the maximum energy transfer, where there is a sharp cut-off point, known as the Compton edge. The problems that this causes and the solutions employed are discussed in section 3.6.5.

Compton scattering is the most probable process for photons in the intermediate energy range and the probability decreases rapidly with increasing energy. The probability is also dependent on the number of electrons available for the photon to scatter from, and hence increases with increasing $Z$.

### Photoelectric Absorption

The process of photoelectric absorption is shown in figure 3.8. An incident photon

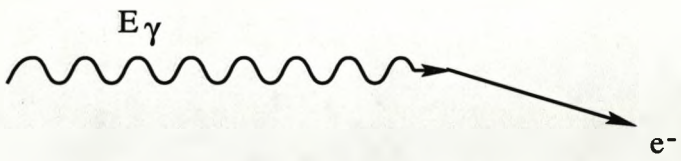


**Figure** 3.8: The process of photoelectric absorption.

is completely absorbed by an atom in the absorber material, and one of the atomic electrons is ejected. This ejected electron is known as a photoelectron. The electron must be bound to the atom, to conserve energy and momentum. The kinetic energy of the photoelectron is given by

$$T_e = E_\gamma - B_e \tag{3.16}$$

where $B_e$ is the binding energy of the atomic electron. The vacancy left in the atomic structure by the ejected electron is filled by one of the electrons from a higher

shell. This transition is accompanied by an emission of an X-ray. These X-rays are also absorbed by the detector. Photoelectric absorption is the most favourable process for the $\gamma$-ray spectroscopist, since the incident photon deposits all of its energy into the detector, but it is only dominant for low energy photons ($< 200$ keV). The interaction is again dependent upon $Z$, and an approximate expression for the absorption probability $\tau$ is

$$\tau \propto \frac{Z^n}{E_\gamma^{3.5}}. \tag{3.17}$$

Here $n$ is normally between 4 and 5 depending on the absorber material. This dependence on $Z$ explains the choice of high-$Z$ materials such as lead for shielding purposes.

### Pair Production

The third important $\gamma$-ray interaction is the process of pair production, shown in

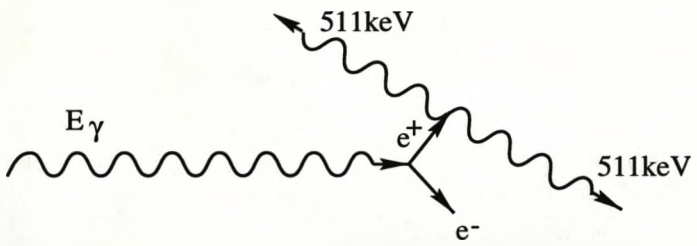


**Figure** 3.9: The process of pair production/annihilation.

figure 3.9. If the incident photon energy is greater than 1.022 MeV (twice the electron rest mass) in the presence of an atomic nucleus an electron/positron pair can be produced. Any residual energy is distributed evenly between the electron and positron as kinetic energy. As the positron slows to thermal energies through interaction with the absorbing medium, it can annihilate with one the atomic electrons producing two $\gamma$ rays of energy 511 keV. These $\gamma$ rays can then either be absorbed or escape the detector. This is evidenced by the so-called *escape peaks* observed in $\gamma$-ray spectra. If one of the 511 keV photons escapes the detector, then a peak is observed at $E_\gamma - m_0c^2$ (single escape peak). If both escape, then a peak is observed at $E_\gamma - 2m_0c^2$ (double escape peak). The process of pair production only becomes important for high energy

$\gamma$ rays ( 5 - 10 MeV) which are outside the energy range of interest in the present work.

### 3.6.2 Electromagnetic Transition Rates

The motion of protons in the nucleus gives rise to charge and current distributions; charge distributions can be described by electric multipole moments and current distributions by magnetic multipole moments. The electromagnetic radiation field produced when the nucleus emits radiation in the form of $\gamma$ rays can be described in terms of a multipole expansion [Blatt 52, De Shalit 74, Ring 80]. If the nucleus decays from a state of spin $I_i$ to state of spin $I_f$, the total transition probability can be determined by

$$T_{fi} = \frac{8\pi\,(L+1)}{\hbar L\,((2L+1)!!)^2}\left(\frac{E_\gamma}{\hbar c}\right)^{2L+1} B\,(\sigma L, I_i \rightarrow I_f) \tag{3.18}$$

where the values of $B\,(\sigma L)$ are known as the *reduced transition probabilities* and are given by

$$B\,(EL, I_i \rightarrow I_f) = \frac{1}{2I_i+1}|\,\langle\, f \,||\, \hat{Q} \,||\, i \,\rangle\,|^2 \tag{3.19}$$

for the electric case, and

$$B\,(ML, I_i \rightarrow I_f) = \frac{1}{2I_i+1}|\,\langle\, f \,||\, \hat{M} \,||\, i \,\rangle\,|^2 \tag{3.20}$$

for the magnetic case, where $\hat{Q}$ and $\hat{M}$ are the electric and magnetic multipole operators, respectively. Here it is assumed that the wavelength of the emitted radiation is long compared to the dimensions of the nucleus. In order to account for the different possible orientations of the angular momentum, $L$, an average over the initial $m$-state values and a sum over the final $m$-state values is taken. A derivation of these expressions can be found in reference [Ring 80].

#### Weisskopf Estimates

The transition rates, under the assumption that the transition is due to a single

proton moving from one shell model state to another, can be estimated from

$$T(EL) = \frac{8\pi(L+1)}{\hbar L((2L+1)!!)^2}\frac{e^2}{4\pi\epsilon_0\hbar c}\left(\frac{E_\gamma}{\hbar c}\right)^{2L+1}\left(\frac{3}{L+3}\right)^2 cR^{2L} \tag{3.21}$$

and

$$T(ML) = \frac{8\pi(L+1)}{\hbar L((2L+1)!!)^2}\left(\mu_p - \frac{1}{L+1}\right)^2\left(\frac{\hbar}{m_p c}\right)^2\left(\frac{se^2}{4\pi\epsilon_0\hbar c}\right)\left(\frac{E_\gamma}{\hbar c}\right)^{2L+1}\left(\frac{3}{L+2}\right)^2 cR^{2L-2}. \tag{3.22}$$

In the above, $\mu_p$ is the magnetic moment of the proton and $m_p$ is the proton mass. The wavefunctions of the states are those obtained using a square well potential. By taking $R = R_0 A^{1/3}$, and by setting the $\left(\mu_p - \frac{1}{L+1}\right)^2$ term in equation 3.22 to be equal to 10, estimates can be made for the lower multipole orders. These are known as the *Weisskopf Estimates*, and are given in table 3.1.

| Weisskopf Estimates | |
|---|---|
| $T(E1) = 1.0 \times 10^{14} A^{\frac{2}{3}} E^3$ | $T(M1) = 5.6 \times 10^{13} E^3$ |
| $T(E2) = 7.3 \times 10^{7} A^{\frac{4}{3}} E^5$ | $T(M2) = 3.5 \times 10^{7} A^{\frac{2}{3}} E^5$ |
| $T(E3) = 3.4 \times 10^{1} A^{2} E^7$ | $T(M3) = 1.6 \times 10^{1} A^{\frac{4}{3}} E^7$ |
| $T(E4) = 1.1 \times 10^{-5} A^{\frac{8}{3}} E^9$ | $T(M4) = 4.5 \times 10^{-6} A^{2} E^9$ |

Table 3.1: Single-particle or Weisskopf estimates. The units are $s^{-1}$ when the $\gamma$-ray energy $E$ is expressed in MeV.

Clearly, these estimates are not realistic calculations of the transition rates, but provide values that can be compared to those measured experimentally.

## Collective Transition Rates

The collective electric and magnetic transition probabilities for rotational nuclei have been deduced by Bohr and Mottelson [Bohr 75]. In this work, it is the $E1$ and $E2$ transition probabilities that are of importance. These are given by

$$B(E1; I_i \rightarrow I_f) = \frac{3}{4\pi} e^2 D_0^2 \langle\, I_i K_i 10 \mid I_f K_f \,\rangle^2, \tag{3.23}$$

and

$$B\left(E2; I_i \rightarrow I_f\right) = \frac{5}{16\pi} e^2 Q_0^2 \langle\, I_i K_i 20 \mid I_f K_f \,\rangle^2 \tag{3.24}$$

where $Q_0$ and $D_0$ are intrinsic electric quadrupole and dipole moments, respectively. $K$ is the projection of the total angular momentum onto the symmetry axis. The ratio of the intrinsic electric dipole to electric quadrupole moment can be extracted from experimental data using the ratio of reduced transition probabilities $B(E1)/B(E2)$. If the intensity of the $E1$ transition is $i_{E1}$ and that of the $E2$ transition $i_{E2}$, then the $B(E1)/B(E2)$ ratio can be calculated using

$$\frac{i_{E1}}{i_{E2}} = \frac{1.587 \times 10^{15} E^3_{\gamma(E1)} B\left(E1\right)}{1.223 \times 10^{9} E^5_{\gamma(E2)} B\left(E2\right)}, \tag{3.25}$$

and the $B(E1)/B(E2)$ ratio obtained is used to extract the ratio of the intrinsic electric dipole to quadrupole moment, $|D_0/Q_0|$, through the equations 3.23 and 3.24 in the following form

$$\frac{B\left(E1\right)}{B\left(E2\right)} = 2.4 \left[\frac{D_0}{Q_0} \frac{\langle\, I_i K_i 10 \mid \left(I_i - 1\right) K_f \,\rangle}{\langle\, I_i K_i 20 \mid \left(I_i - 2\right) K_f \,\rangle}\right]^2. \tag{3.26}$$

Table 3.2 shows the collective transition rate estimates given in terms of the reduced transition probabilities for the lowest multipoles. The estimates are obtained by multiplying out the constant terms in equation 3.18.

| Collective Transition Rates | |
|---|---|
| $T(E1) = 1.59 \times 10^{15} B(E1) E^3$ | $T(M1) = 1.76 \times 10^{13} B(M1) E^3$ |
| $T(E2) = 1.22 \times 10^{9} B(E2) E^5$ | $T(M2) = 1.35 \times 10^{7} B(M2) E^5$ |
| $T(E3) = 5.67 \times 10^{2} B(E3) E^7$ | $T(M3) = 6.28 \times 10^{0} B(M3) E^7$ |
| $T(E4) = 1.69 \times 10^{-4} B(E4) E^9$ | $T(M4) = 1.87 \times 10^{-6} B(M4) E^9$ |

Table 3.2: Transition rates expressed in terms of the reduced transition probabilities. The units are: $T(\sigma L)$ – $s^{-1}$, $B(EL)$ – $e^2 fm^{2L}$, $B(ML)$ – $\mu_n^2 fm^{2L-2}$, and $E$ – MeV.

## Selection Rules

For a given transition the total angular momentum must be conserved. This means

that the initial angular momentum, $I_i$, must equal $I_f + L$, and the three terms form a closed vector triangle. The angular momentum selection rule is thus

$$|I_i - I_f| \leq L \leq I_i + I_f \quad \forall \quad L \neq 0. \tag{3.27}$$

Since the photon has an intrinsic spin of 1, a transition in which $I_i = I_f$, $L = 0$ cannot occur. A *stretched transition* is one in which the photon carries the difference between the angular momentum of the initial and final states. In addition to the angular momentum selection rule, there is the parity selection rule, which determines the electric or magnetic nature of the emitted radiation. The parity of the radiation field is given by

$$\begin{aligned} \pi(ML) &= (-1)^{L+1} \\ \pi(EL) &= (-1)^{L}. \end{aligned} \tag{3.28}$$

Thus even-multipole electric and odd-multipole magnetic transitions have even parity, and occur when $\pi_i = \pi_f$, whilst odd-multipole electric and even-multipole magnetic transitions have odd parity and occur when $\pi_i = -\pi_f$.

### 3.6.3 Internal Conversion

A competing electromagnetic process to $\gamma$-ray emission is that of internal conversion. In this process, the excitation energy of the nucleus is transferred to one of the atomic electrons, causing it to be emitted from the nucleus. The kinetic energy of the emitted electron depends upon the electron binding energy, $B_e$ and the transition energy $(E_i - E_f)$

$$T_e = (E_i - E_f) - B_e. \tag{3.29}$$

Electrons in different atomic orbitals have different binding energies, thus it is possible that for a given transition there are several possible electron energies. Consideration of equation 3.29 shows that if the transition energy is smaller than the electron binding energy for a particular shell, then the electrons in that shell cannot be emitted. Conversion electrons are thus labelled by the atomic shell from which they originated.

The principal atomic quantum numbers $n = 1, 2, 3$ correspond to the K, L, and M shells, respectively. It is also possible to resolve the shell substructure, thus conversion electrons from the L shell can be labelled $L_I$, $L_{II}$, or $L_{III}$, if they originated from the $2s_{1/2}$, $2p_{1/2}$ or $2p_{3/2}$ atomic orbitals, respectively. The vacancy left in the atomic shell by emission of a conversion electron is filled by one from a higher shell, and the difference in energy between the two shells appears in the form of an X-ray. This characteristic X-ray emission is often useful for the $\gamma$-ray spectroscopist when determining the $Z$ of the nucleus from which $\gamma$ rays under investigation were emitted. The internal conversion coefficient, $\alpha$, is defined as the ratio of internal conversion decay probability to the $\gamma$-decay probability

$$\alpha = \frac{\lambda_e}{\lambda_\gamma}. \tag{3.30}$$

The total decay probability is then

$$\lambda_t = \lambda_\gamma (1 + \alpha). \tag{3.31}$$

The internal conversion coefficient depends on the energy of the transition, the atomic number of the nucleus and principal atomic quantum number in approximately the following way:

$$\alpha \propto \frac{Z^3}{n^3 E_\gamma^{2.5}}. \tag{3.32}$$

Internal conversion coefficients are also larger for magnetic transitions than for electric transitions, and increase with increasing multipolarity. Measured $\gamma$-ray intensities must be corrected in order to obtain the total transition intensities, using equation 3.31 and tabulated values of internal conversion coefficients. In the course of this work, the values of Rösel, Fries, Alder and Pauli were used [Rösel 78].

### 3.6.4 Germanium Detectors

Discrete-line $\gamma$-ray spectroscopy requires a detection system that offers excellent energy resolution. Today, practically all $\gamma$-ray spectroscopy experiments employ high-resolution germanium detectors. The germanium detector, similar to other semiconductor detectors, is a large reverse-biased p-n junction diode. At the junction between

the p-type and n-type material, the migration of electrons from the n-type material and holes from the the p-type material gives rise to a region of net zero charge. This region is known as the *depletion region.* The net positive charge on one side of the junction, and the net negative charge on the other side, sets up an electric field gradient across the depletion region. Any $\gamma$ rays interacting with the germanium, through the processes described in section 3.6.1, will produce electron-hole pairs in the depletion region, which will then be swept to the edges of the detector because of the electric field gradient, constituting an electric current. Since the depletion region is the active part of the Ge detector, the active volume is required to be as large as possible. If a reverse-bias is applied, the width of the depletion region can be increased. The width is proportional to $\left(\frac{V}{N}\right)^{\frac{1}{2}}$. Here, $V$ is the bias voltage applied and $N$ is the impurity concentration of the germanium. Natural purity germanium can only maintain a depletion region of a few millimetres before electrical breakdown occurs. Therefore at a given bias voltage the only way to increase the width of the depletion region is to reduce the impurity concentration, $N$. This fact led to the introduction of *lithium-drifted* germanium detectors known as Ge(Li) detectors. These detectors are manufactured by adding lithium donor atoms to the Ge material. The donor lithium atoms exactly balance the acceptor impurities, resulting in a very low net impurity level. This allows the depletion region to be extended over the whole of the lithium drifted region. Advances in manufacturing techniques have, however, allowed extremely pure Ge crystals to be grown. This *high-purity germanium*, or HPGe, has impurity concentrations of around one part in $10^{12}$, allowing depletion depths of several centimetres to be achieved. High-purity germanium also has the advantage over Ge(Li), in that it can be stored at room temperature. Ge(Li) detectors must be stored at 77 K, to avoid a redistribution of the drifted lithium, which effectively destroys the detector.

The active volume of a HPGe detector can be further increased by changing the shape of the crystal. If the crystal is "bulletised" (has the corners rounded off), then the electric field inside will be more uniform allowing active volumes of approximately

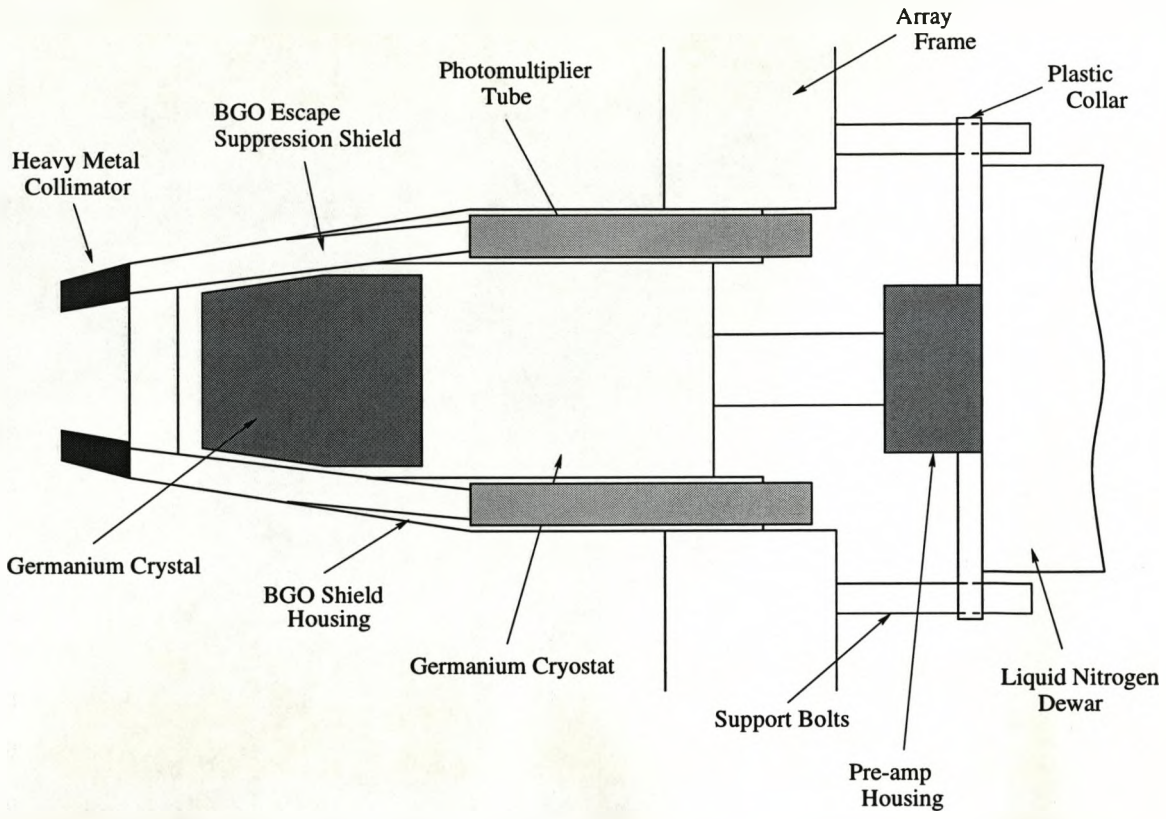


**Figure** 3.10: Anatomy of a EUROGAM PhaseI-type germanium detector.

400 $cm^3$ to be achieved. In $\gamma$-ray spectroscopy experiments, the germanium detectors used have the $n^+$ contact on the inside and the $p^+$ contact on the outside. The reason for this is that the $n^+$ contact is much thicker than the $p^+$ contact and may attenuate the incident radiation. This, along with the fact that p-type material is more susceptible to neutron damage, is why n-type material is used in $\gamma$-ray spectroscopy experiments.

The energy required to create an electron-hole pair in Ge is approximately 3 eV,thus an incident $\gamma$ ray, with an energy of several hundred keV, produces a large number of such pairs, leading to good resolution and low statistical fluctuations. These are desirable properties as discussed earlier. HPGe detectors are operated at temperatures of around 77 K, in order to reduce noise from electrons which may be thermally excited across the small band gap in Ge (0.67 eV) at room temperature. This is

achieved through thermal contact of the Ge crystal with a dewar of liquid nitrogen, using a copper rod, known as a cold finger.

### 3.6.5 Compton Suppression

As discussed in section 3.6.1, Compton scattering means that many $\gamma$ rays which enter the Ge detector will not deposit their full energy, leading to a large *Compton continuum.* In order to reduce the contribution of scattered $\gamma$ rays the Ge detector can be surrounded by an inorganic scintillator detector. The two detectors are operated in anti-coincidence, which means that if an event occurs at the same time in both detectors, then the event is rejected. The majority of *escape suppression shields*, as they are known, use bismuth germinate (BGO). The reason for this choice is that BGO has excellent timing properties, which is desirable for coincidence work, and high density (7.3 g/cm$^3$), so that a relatively small amount of material is needed in order to stop fully the scattered photons. This fact becomes important when we wish to closely pack many detectors around a target to form an array (see section 3.6.6). An example of the effect of Compton suppression is shown in figure 3.11.

The figure shows a spectrum of emitted $\gamma$ rays following the $\beta^-$ decay of $^{60}$Co to $^{60}$Ni. The most important features are labelled. The *Compton edge* corresponds to the situation described earlier of maximum energy loss when $\theta = \pi$ in the Compton scattering equation 3.14. The *photopeak* is of particular interest to the $\gamma$-ray spectroscopist. This corresponds to the situation when the incident $\gamma$ ray deposits its full energy in the Ge detector. An important quantity is the peak-to-total ratio, which is the ratio of the number of counts in the photopeak to the total number of counts in the spectrum, above an energy of around 100 keV. It can be seen from figure 3.11 that escape suppression improves this ratio considerably, since the number of counts in the Compton continuum region is reduced, whilst the number of counts in the photopeak is not affected appreciably (see inset). It is preferable that the peak-to-total ratio is as high as possible, and typical values for current escape-suppressed spectrometers are around 0.5 to 0.6.

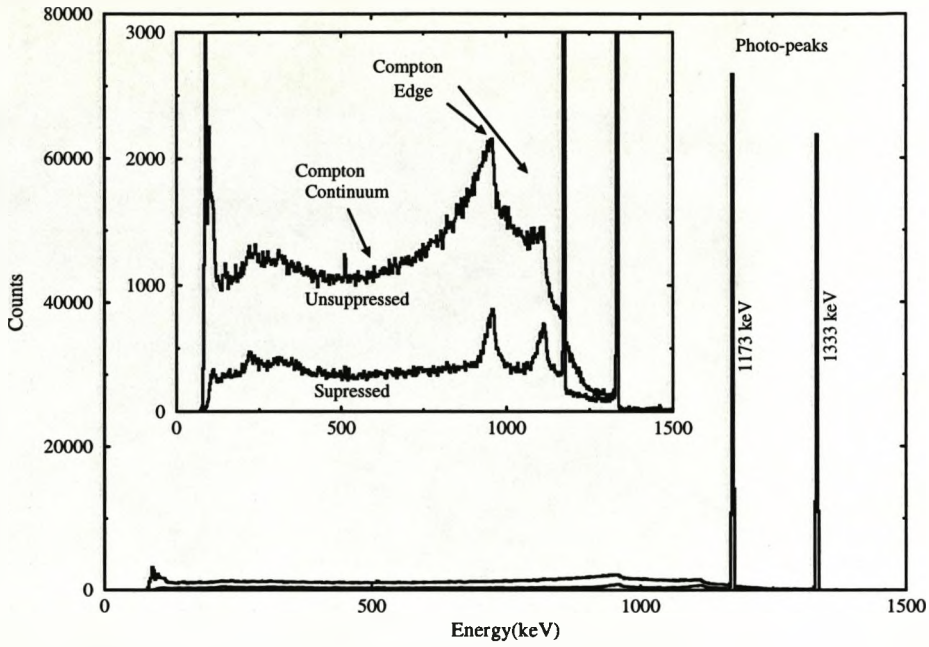


**Figure** 3.11: Spectrum of $\gamma$ rays emitted following $\beta$-decay of $^{60}$Co to $^{60}$Ni. The upper spectrum was obtained with an unsuppressed Ge detector, the lower one with the Ge detector inside an escape suppression shield.

### 3.6.6 Arrays of Ge detectors

Several escape-suppressed spectrometers, described in the previous section, can be mounted around a target to form an *array*. Most of today's multi-detector Ge arrays are designed to measure the energies and coincidence relationships of many $\gamma$-rays emitted in a cascade from high-spin states. Such measurements require as many $\gamma$ rays as possible to be detected. The power of an array to collect $\gamma$ rays is defined by the *total photopeak efficiency*. This has led to the development of so-called "third-generation" arrays, such as GAMMASPHERE and EUROGAM. These arrays consist of around 80-100 Ge detectors, covering as much of the $4\pi$ solid angle around the target as possible. An important quantity in the discussion of large arrays of Ge detectors is the *resolving power*, R, which provides a measure of the spectrum quality obtainable with a particular array. The resolving power is defined as

$$R = \left( \frac{S_{E_\gamma}}{\Delta E_\gamma} \right) PT \tag{3.33}$$

where $\Delta E_\gamma$ is the full-width at half-maximum resolution of the measured $\gamma$ rays, $S_{E_\gamma}$ is the average energy separation between consecutive $\gamma$ rays in the cascade, and $PT$ is the peak-to-total ratio. Inspection of equation 3.33 shows that the only way to improve the resolving power is to either increase the peak-to-total ratio, $PT$, or to reduce the energy resolution, $\Delta E_\gamma$. In practice, it is difficult to increase the peak-to-total ratio. $\Delta E_\gamma$ has four major contributing factors. These are:

- the intrinsic resolution of the detector, $\Delta E_{in}$, which is a property of the individual detector;
- Doppler broadening due to the opening angle of the detectors, $\Delta E_D$, which can be improved by using "segmentation", or clusters of smaller detectors;
- Doppler broadening due to the angular spread of the recoils, $\Delta E_R$, which can be improved using a "kinematic correction";
- Doppler broadening due to the velocity distribution of the recoils, $\Delta E_V$.

These factors contribute as follows:

$$\Delta E_\gamma^2 = \Delta E_{in}^2 + \Delta E_D^2 + \Delta E_R^2 + \Delta E_V^2. \tag{3.34}$$

In order to observe a peak in a given spectrum, it must be resolvable in a complex spectrum, stand above the background and be statistically significant. The limit of observation of an array, $\alpha_0$, is the minimum fractional intensity of the total reaction cross section that be observed with the array. This limit is dependent on the total photopeak efficiency and the resolving power. The peak-to-background ratio in an $n$-fold (number of coincident $\gamma$ rays) spectrum can be determined from the following expression:

$$\left(\frac{N_p}{N_b}\right)_n = \alpha_0 \left(0.76R\right)^n \tag{3.35}$$

here it is assumed that the number of $\gamma$ rays in the cascade, $M_\gamma$, is much greater than the fold $n$, and that $N_p << N_b$ [Nolan 94]. It is well documented (see, for example,

refs. [Nolan 94, Beausang 96]) that the limit of observation for a given resolving power decreases rapidly with increasing fold, whilst for a given photopeak efficiency the limit of observation increases with fold. Thus, an optimum fold must be used to obtain the lowest possible limit of observation. With the latest generation of germanium arrays, the smallest limit of observation that can be achieved is around $1 \times 10^{-4}$, with an optimum fold of 4. This means that, if the total reaction cross section is 1 barn, nuclei produced with cross sections of around 100 $\mu$b can be studied. However, as discussed in the introduction to this chapter, many nuclei which we wish to study can only be produced with cross sections of less than 10 $\mu$b, meaning that at least an order of magnitude improvement in sensitivity would be needed if a stand-alone Ge detector array is used. This improvement is possible, if the reaction channels of interest are selected from the total set of open channels. This *channel selection* can be performed using ancillary devices, such as recoil separators (See reference [Ennis 92] for a quantative discussion of the principles of channel selection). A recoil separator will select only those nuclei produced via fusion-evaporation reactions, of which the desired reaction channel may form a significant fraction. Selection of the channels of interest has the effect of lowering the limit of observation. This is illustrated in figure 3.12 for the JUROSPHERE, EUROBALL AND GAMMASPHERE arrays.

The figure shows the fractional intensity of the $\gamma$-ray peak of interest against f(R), where f(R) is defined as

$$f(R) = \left[\frac{\sigma}{\sigma_{total}}\right] \times \epsilon_{recoil}. \tag{3.36}$$

In the above equation, $\sigma$ is the total cross section of the selected channels, $\sigma_{total}$ is the total reaction cross section and $\epsilon_{recoil}$ is the efficiency of the channel selection device. In the production of this figure it is assumed that the total reaction cross section is 1 barn, and that a 2 pnA beam is incident on 1 mg/cm$^2$ A=208 target for five days. Also, the peak-to-background ratio must be greater than 0.2 and the number of counts in the peak must be greater than 100 or more than twice the square root of the background count. The optimum fold for a given f(R) is also shown.

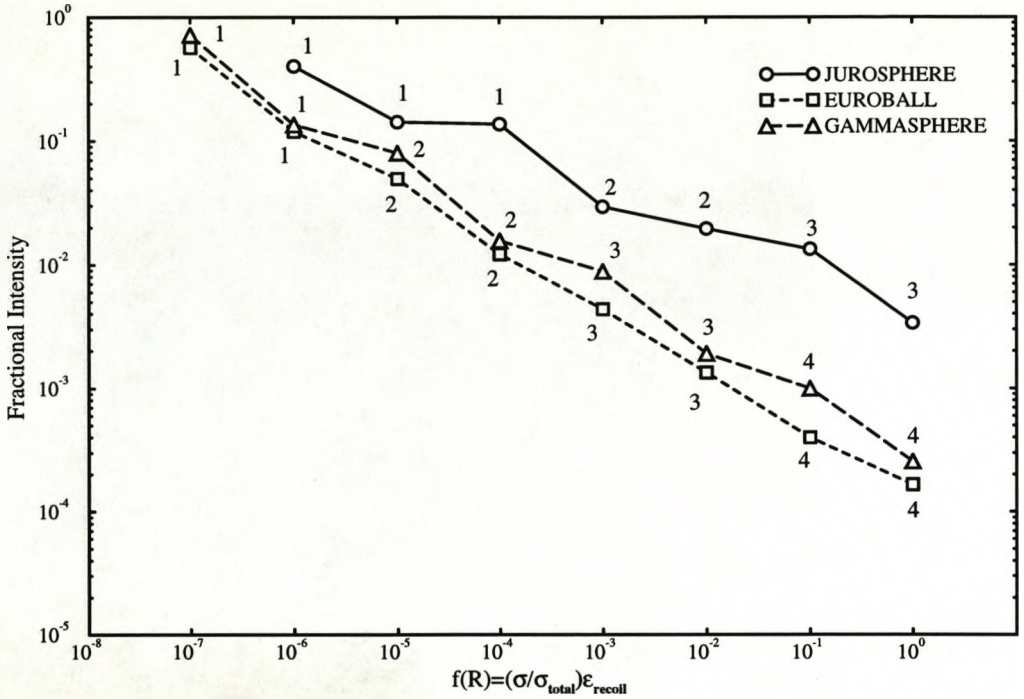


**Figure** 3.12: Fractional intensity of the $\gamma$ ray of interest as a function of f(R), where f(R)=$(\sigma/\sigma_{total}) \times \epsilon_{recoil}$, for several arrays currently in operation. The assumptions made in the production of this figure are discussed in the text.

### 3.6.7 The JUROSPHERE Array

The recoil-decay-tagging experiment described in this work utilised the JUROSPHERE Ge detector array, situated at the Accelerator Laboratory of the University of Jyväskylä, Finland during March to November 1997. At the time of the experiment, the array consisted of 12 Eurogam Phase-I [Nolan 90] and 10 TESSA-type [Nolan 85] Compton-suppressed germanium detectors. The maximum number of detectors that can be placed in the array frame is 15 Eurogam Phase-I and 10 TESSA detectors, with a total photopeak efficiency of 1.7% at 1.33 MeV. The individual Eurogam Phase-I-type detectors have an efficiency of approximately 70% (relative to a 3 inch $\times$ 3 inch sodium-iodide detector) at 1.33 MeV; the TESSA-type detectors have a relative efficiency of approximately 25% . The Phase-I detectors are arranged in two rings; five at an angle of 157.6° and ten at 133.6° to the beam direction. The TESSA detectors

are mounted in two rings of five detectors at angles of 79° and 101° to the beam direction. The specifications of the array are summarised in table 3.3; a schematic is shown in figure 3.13.

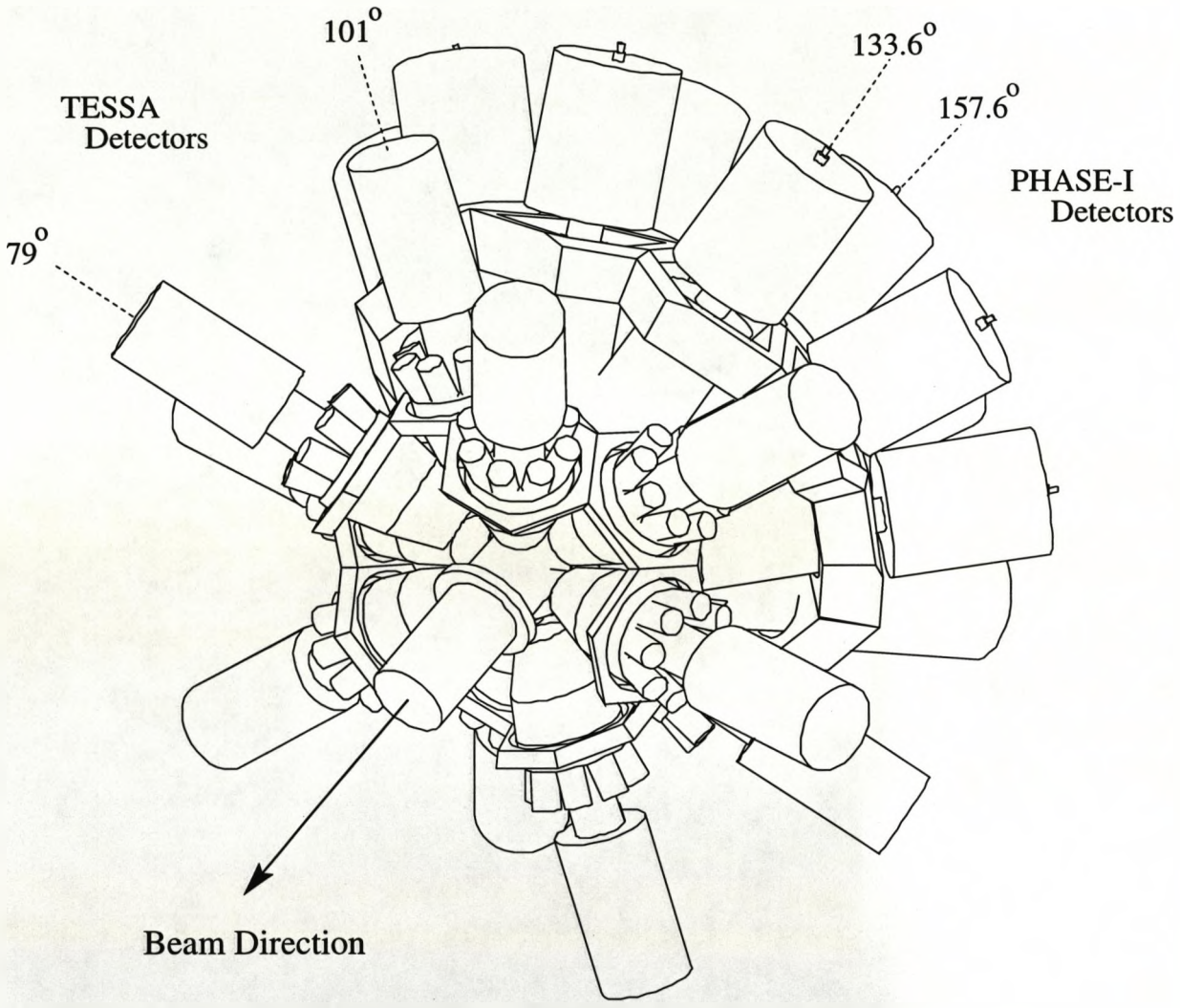


**Figure** 3.13: A schematic drawing of the JUROSPHERE Ge array.

The detection efficiency of the array is dependent upon the energy of the incident $\gamma$ rays. At energies above 300 keV, the efficiency $\epsilon$ can be approximated by the following function:

$$\epsilon = cE_{\gamma}^{-x} \tag{3.37}$$

where $0.5 \leq x \leq 0.6$ and c is a constant. The efficiency at lower energies is lower due

| Detector Type(Number) | $\theta^{\circ(a)}$ | $\phi^{\circ(b)}$ |
|---|---|---|
| TESSA(5) | 79 | 0, 72, 144, 216, 288 |
| TESSA(5) | 101 | 36, 108, 180, 252, 324 |
| PHASE-I(5) | 157.6 | 36, 108, 180, 252, 324 |
| PHASE-I(10) | 133.6 | 18, 54, 90, 126, 162, |
| | | 198, 234, 270, 306, 342 |

Table 3.3: The JUROSPHERE array specifications. $^{(a)}$ defined with respect to the beam direction. $^{(b)}$ $\phi$=0° is defined as vertically upwards, $\phi$ increases in a clockwise direction when the array is viewed from a position upstream.

to the fact that the charge collection is poor for low-energy incident radiation. The relative efficiency curves for the detection of single $\gamma$-ray events in the JUROSPHERE array are shown in figure 3.14.

These are produced by comparison of measured transition intensities to known relative transition intensities for particular $\gamma$-ray sources. In this case, the source used was a mixture of $^{133}$Ba and $^{152}$Eu, and was placed at the target position subsequent to the in-beam experiment. The EFFIC (Oak Ridge) and EFFIT (Radware) computer codes were used to obtain the relative intensities and to fit the curves, respectively. The maximum of the curve corresponding to the TESSA-type detectors is at lower energy than that of the Phase-I detectors; this is due to the smaller crystal size of the TESSA-type detectors. The charge collection efficiency is better in the small crystals at low energy than in the larger Phase-I crystals. The performance of the JUROSPHERE array is compared to that of the third generation germanium arrays EUROBALL and GAMMASPHERE in figure 3.12. It can be seen that the limit of observation for the JUROSPHERE array with no channel selection is approximately $3 \times 10^{-3}$ with an optimum fold of 3, compared to around $1 \times 10^{-4}$ with an optimum fold of 4 for the third generation arrays. Thus, operated alone the JUROSPHERE device has around an order of magnitude less sensitivity. However, the coupling of an efficient

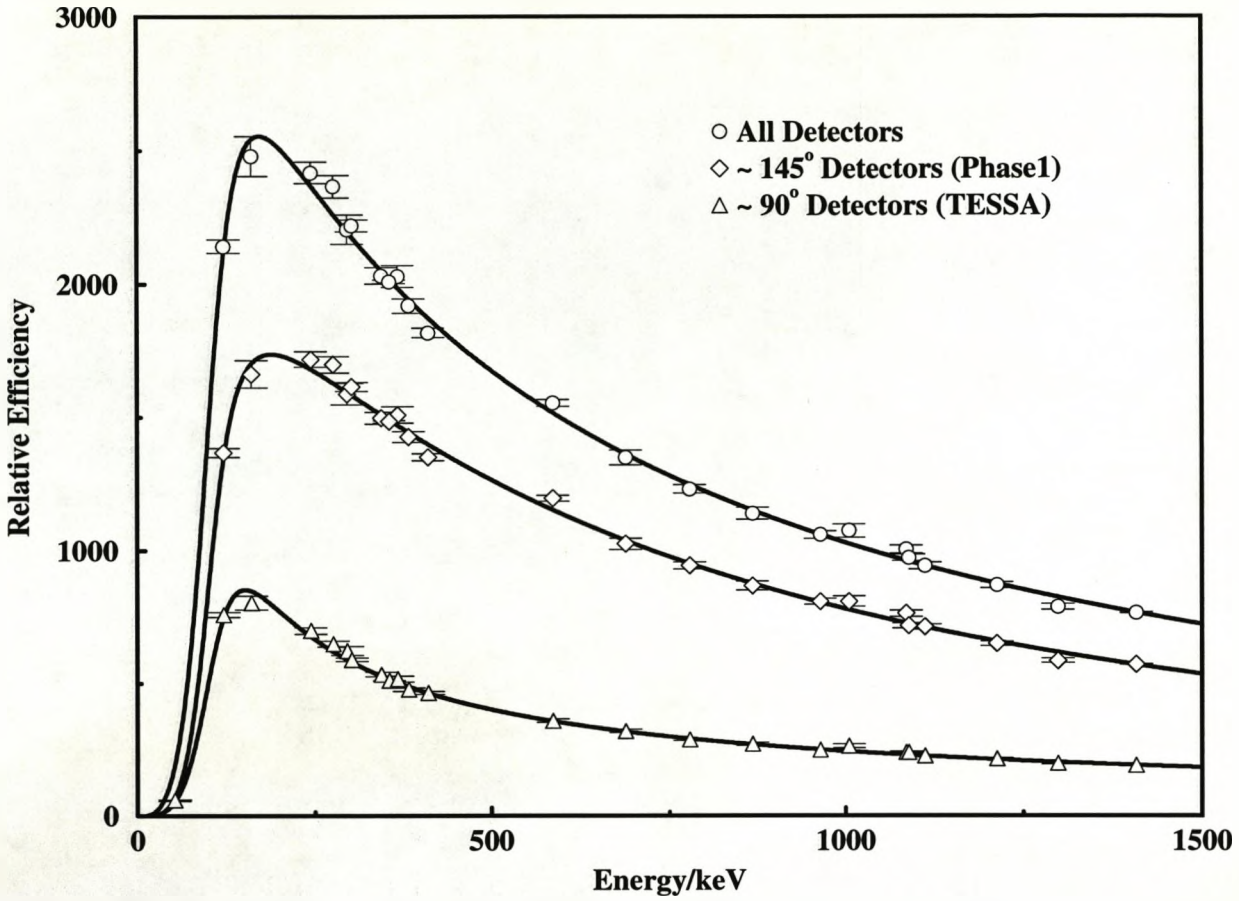


**Figure** 3.14: Single-fold efficiency curves for the JUROSPHERE Ge array, produced from measurements involving a mixed $^{133}$Ba and $^{152}$Eu $\gamma$-ray source.

recoil separator, such as RITU, to JUROSPHERE leads to much higher sensitivity, as discussed in section 3.6.6. The efficiency of the RITU device is such that in certain cases, the JUROSPHERE-plus-RITU device may be more sensitive than that of a device such as GAMMASPHERE-plus-FMA. To illustrate this point, consider the reaction $^{208}$Pb($^{22}$Ne,4n)$^{226}$U. It is assumed that the $^{226}$U exit channel constitutes $1 \times 10^{-5}$ of the total reaction channel, and that the transmission efficiencies of RITU and the FMA are 10% and 1% respectively. The values of f(R) are thus $1 \times 10^{-6}$ for JUROSPHERE-plus-RITU and $1 \times 10^{-7}$ for GAMMASPHERE-plus-FMA. Figure 3.12 shows that the limit of observation is lower by a factor of two for the former device, at an optimum fold for both devices of 1.

# Chapter 4

# First Observation of Excited States in $^{226}$U

This chapter presents a discussion of an experiment designed to identify excited states in $^{226}$U for the first time. The experiment was carried out at the Accelerator Laboratory of the University of Jyväskylä, Finland, during April 1997. Firstly, the experimental details and analysis techniques employed are discussed, followed by presentation and discussion of the results obtained.

## 4.1 Experimental Details

The experiment utilised the JUROSPHERE array of Compton-suppressed germanium detectors, coupled to the RITU gas-filled recoil separator. The properties of the JUROSPHERE and RITU devices are discussed in sections 3.6.7 and 3.5.3, respectively. In order to produce $^{226}$U nuclei the reaction $^{208}$Pb($^{22}$Ne,4n)$^{226}$U was employed. Production cross sections have been measured at different bombarding energies for the $^{22}$Ne + $^{208}$Pb reaction in previous work [Andreyev 89]. The measured production cross sections for the $xn$ and $\alpha xn$ channels against laboratory bombarding energy (at the centre of the target) are shown in figure 4.1. The maximum production cross section for the $4n$ channel is approximately 6$\mu$b at a bombarding energy of 110 MeV, com-

pared with a maximum of approximately 300$\mu$b for the $\alpha xn$ channels. In the present

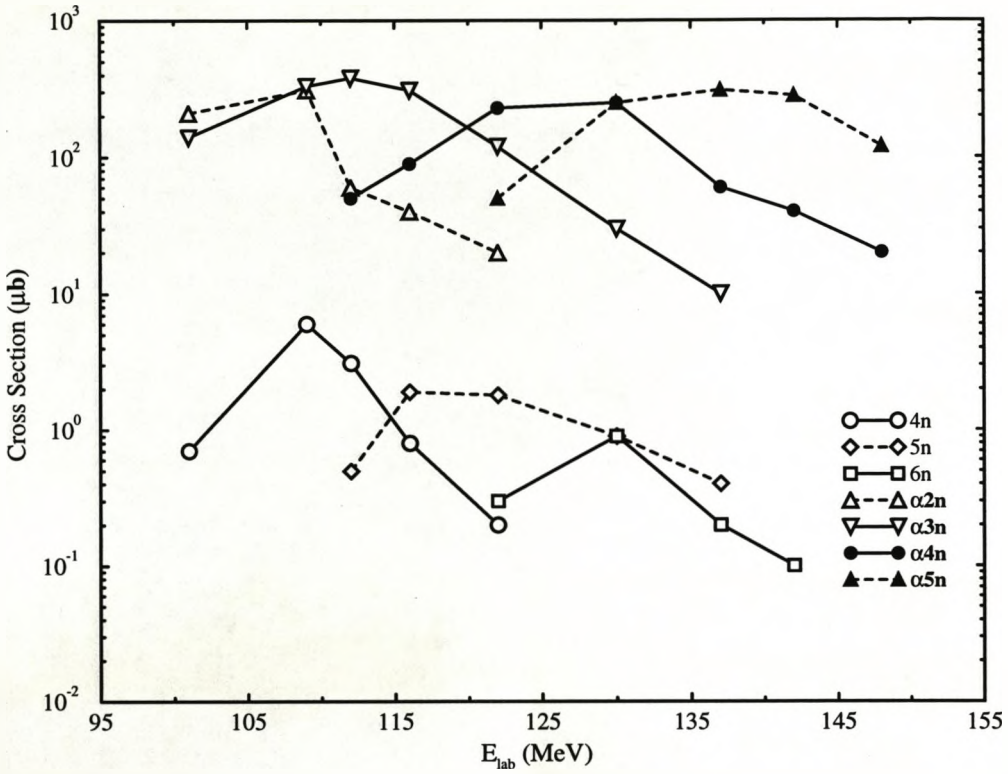


**Figure** 4.1: Production cross section as a function of centre-of-target laboratory bombarding energy for the reaction $^{22}$Ne + $^{208}$Pb. Data are taken from reference [Andreyev 89]. Lines are drawn to guide the eye.

work, the $^{22}$Ne beam was delivered by the K=130 MeV cyclotron at a laboratory energy of 112 MeV, and bombarded a 250$\mu$g/cm$^2$ $^{208}$Pb target. In this experiment, the helium gas filling the RITU device was separated from the beam-line vacuum by a 100$\mu$g/cm$^2$ C foil. Energy losses through the C foil and the front of the target give a residual centre-of-target beam energy of approximately 111 MeV, close to the peak cross section shown in figure 4.1. The charge state of the beam was $5^+$, and the average beam intensity was approximately 16 pnA. The total irradiation time was approximately 320 hours. In order to observe any $\gamma$ rays emitted from excited states populated by $\alpha$ decay, a TESSA-type detector was placed behind the RITU focal-plane Si-strip detector.

### 4.1.1 Electronics and Data Acquisition

Block diagrams of the signal-processing electronics used in the experiment are shown in figures 4.2 and 4.3. The main purpose of the system is to record the energy, time and position of events detected in both the germanium array and the focal plane Si-strip detector. In the present case, the signal-processing system is also used to perform a preliminary selection of events of interest, such that only those $\gamma$-rays which are detected "in coincidence" with events in the RITU focal plane detector are recorded.

#### RITU Electronics

A schematic showing the coupling of one of the RITU focal plane Si detector strips to the electronics is presented in figure 4.2. As discussed in section 3.5.5, the detector consists of 16 strips, which in this measurement were coupled to form 8 strips. Both ends of a particular strip are connected to a charge-sensitive preamplifier, which

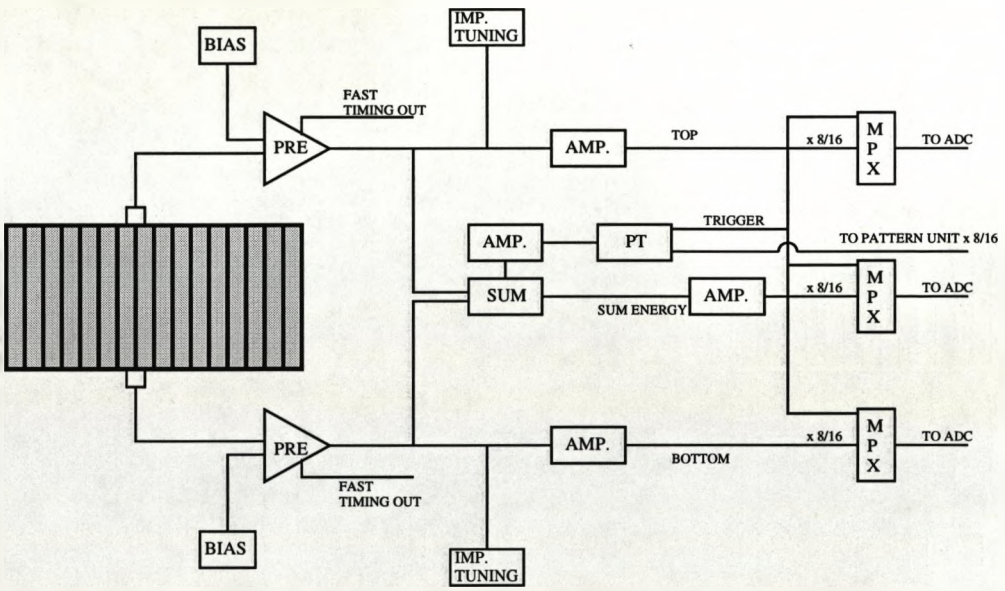


**Figure** 4.2: Block diagram showing the coupling of the RITU detector to the pulse-processing electronics. In this figure, PRE represents a pre-amplifier, AMP a linear amplifier, PT the pattern trigger and MPX a multiplexer.

provide two outputs; one is a fast timing signal, the other is used to determine the

energy of detected events. The signals from both ends of the strip (known as the *top* and *bottom* position signals) are summed to provide the total energy of the event, and ratio of the signal from one end of the detector to the total energy signal is used to determine the vertical position at which the event occurred. The sum signal is split into two, one of which is to provide a trigger. Thus, each strip has four output signals which are then passed to linear amplifiers[1]. The amplifiers used for the energy signal have $2\mu$s shaping times; those for the top and bottom signals have $0.5\mu$s shaping times. The top, bottom and energy outputs are then passed to multiplexers. There is one multiplexer for each of the three output types. Outputs of a particular type from all 8 strips are fed into one multiplexer. The multiplexers give a single output when triggered by an appropriate signal. This is provided by a pattern trigger which produces NIM pulses from an analogue output given by a $0.3\mu$s shaping time amplifier. The trigger signals (one for each strip) are then "daisy-chained" across the multiplexers, thus only the outputs from one strip at a time may be read out. The multiplexer output is then fed to an ADC (Analogue-to-Digital Converter) which can then be read out by the acquisition system (see next page). The use of multiplexers is made possible by the low total count rate in the strip detector, which is typically less than 100 Hz. The use of multiplexers reduces the number of ADCs that are needed. The triggering pulses are also fed to a bit-pattern unit (see figure 4.3), which provides identification of the strip number in which a particular event occurred. The majority of the modules used in the RITU electronics were designed and built at GSI, Darmstadt.

### JUROSPHERE Electronics

The signal-processing electronics for the germanium detectors operate in a similar manner to the RITU electronics, in that the energy, time and the identity number of

[1]In some cases, the energy of recoil implants is very high (> 20 MeV) and the position and energy signals are further split into two. The signals are then amplified in two different chains, one with high-gain and one with low-gain amplification. The low-gain amplification channel is for recoil implants; the other for high-resolution decay measurements. For the reactions used in this work, the recoil implants have low energy, thus only one amplification range is needed.

the detector in which an event occurred are recorded. The system, which uses NIM-standard nuclear spectroscopy modules, is represented schematically in figure 4.3. The rejection of events which occur when a $\gamma$-ray Compton scatters out of the germanium detector is also performed by the system. The signal from the germanium detectors is split into two, one channel is used to determine the total energy deposited in the detector, the other is for timing purposes. The energy signal is input to a spectroscopy amplifier, with a shaping time of $2\mu$s. The output from the spectroscopy amplifier is then fed to an ADC, from where it can be processed by the data acquisition system. The timing signal is fed to a timing filter amplifier or TFA. The TFA provides a fast pulse, which is then passed to a constant fraction discriminator (CFD). The CFD gives a logic signal as output, provided the input analogue signal is above a certain threshold. Normally this threshold is set so that it is just above the noise level. The width of the output logic signal can be adjusted, and is normally set to around 50 ns. The logic signal from the CFD is then passed on to a coincidence unit, which has two other inputs. These are: (i) a signal from the spectroscopy amplifier which is present when the amplifier is not processing an event ("not-busy"), and (ii) a signal from the BGO suppression shield, which is used to veto events that correspond to Compton scattering. The width of the logic signal from the BGO channel is made wider than that for the germanium detector, since the germanium detectors have poorer timing qualities. The not-busy signal is used to reject "pile-up" events, that is if two $\gamma$-rays are detected by an individual detector in a short space of time (such that the energy of the two $\gamma$-rays is summed in the amplifier), then the event is not processed by the system. The coincidence box only gives an output if the "not-busy" and TFA output signal are both present. This output is then used to gate the ADC, so that the energy is read out only when the ADC gate is present. The output from the coincidence box (signal width approximately 100 ns) is also fed to a multiplicity logic unit (MLU) and to a fan in/fan out unit (FIFO). The MLU only gives an output logic signal if the number of inputs present at the same time, n, is greater than a certain threshold. In this case the threshold was set to $n \geq 2$, and the output from the MLU was used

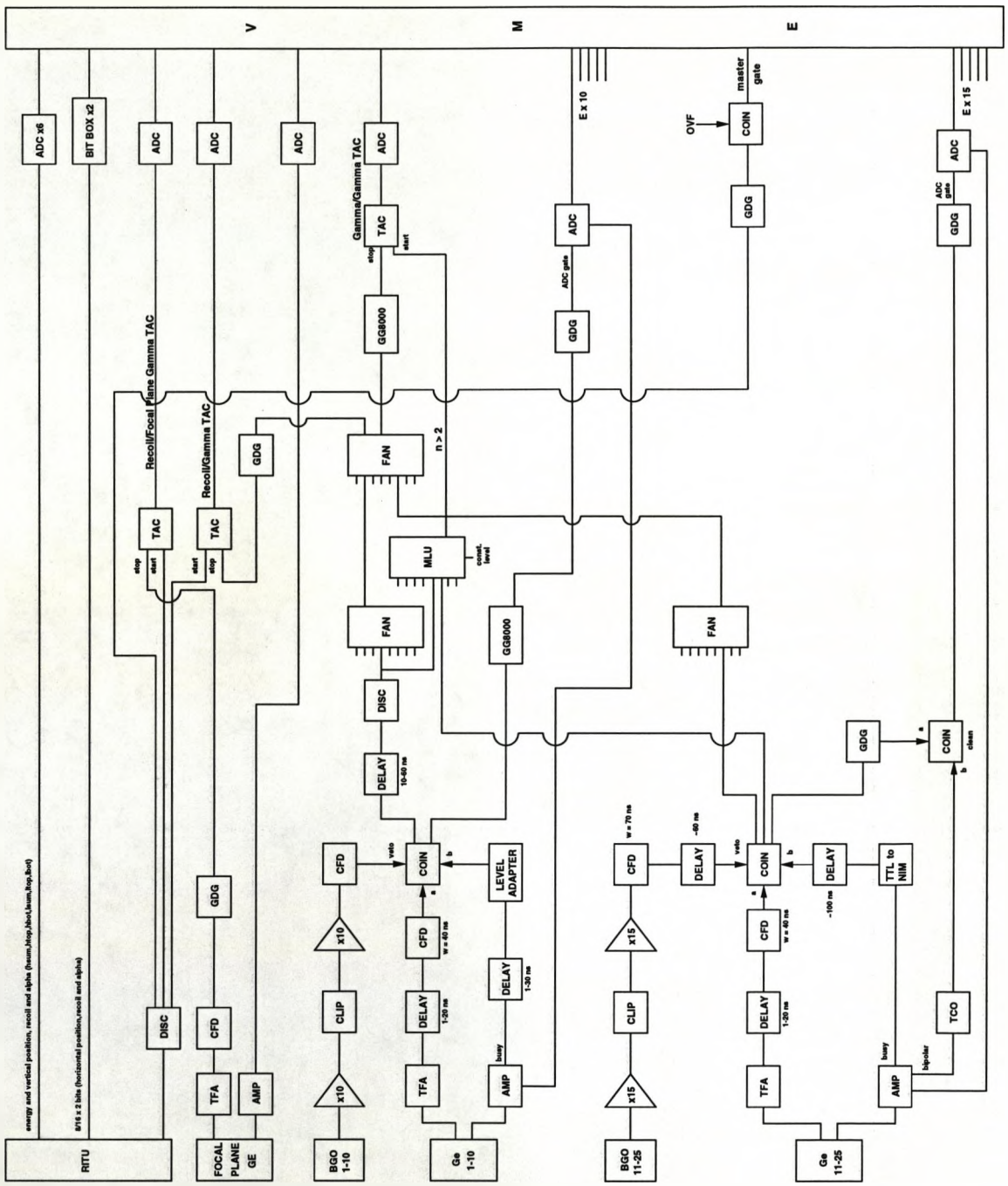


**Figure** 4.3: Block diagram of the electronics set-up used in the recoil-decay tagging experiment described in this chapter. See text for details.

to start the $\gamma$-$\gamma$ time-to-amplitude converter (TAC). The FIFO is used to provide a logical OR of all the germanium detectors, and gives a signal that a $\gamma$ ray has been detected. The output from the FIFO is then used as a stop signal for the recoil-$\gamma$ and $\gamma$-$\gamma$ TACs. The TACs record the time difference between the start and stop signals that are fed to them. The recoil-$\gamma$ TAC is started by a signal generated from a logical OR of the fast timing outputs of the RITU strip detector. In the offline analysis it is used to select those $\gamma$-ray events that are in prompt coincidence with recoil events.

## Data Acquisition

The further processing of events is controlled by the data acquisition system. Each ADC is connected to a VME interface card which allows the continuous histogramming of singles data. This means that the data are simply read out as they arrive at the ADC. These data are used for online monitoring and are not recorded onto magnetic tape. The coincidence data are read out when the master trigger conditions are fulfilled. In the experiment described here, the master trigger signal is generated from the logical OR of the RITU detector fast timing outputs described above. The master trigger signal (with a width of approximately 10 $\mu$s) is then fed to a FERA ADC interface card which enables the read-out of any coincident ADCs. Thus, the germanium detector ADCs are only read out when they are in coincidence with a recoil implant. This reduces the amount of data that is written to tape[2]. In this case, the majority of $\gamma$-ray events detected correspond to fission, and are not of interest in the present work. The FERA interface card passes the data to the high-speed memory and subsequently to the event builder. The event builder converts the data into EUROGAM format. The formatted event is then sent through an ethernet link to the tapeserver, and recorded onto magnetic tape. The control of the acquisition system and online monitoring is performed using a SUN workstation and the MIDAS analysis package.

[2]The reduction in the amount of data written to tape can be seen from comparison of the total event rate with the master trigger rate. The total event rate was approximately 120 kHz, whereas the master trigger rate was approximately 40 Hz.

## 4.2 Analysis

The data obtained in the experiment described in this chapter were essentially analysed in two steps. Firstly, the RITU Si-strip focal plane data are corrected for the position-energy dependence, and calibrated "internally"; secondly, the recoils and $\gamma$ rays of interest are selected through the correlation method. The techniques employed and spectra obtained are discussed further below.

### 4.2.1 Position-Energy Corrections

As discussed in section 4.1.1, the RITU Si-strip detector energy is obtained through a sum of the top and bottom detector signals. This means that the observed energy is dependent on the vertical position of the event in the detector, due to impedance differences in the connections at either end of the strip. A correction factor for this position dependence must be determined for each strip, before any energy calibrations can be made. The correction factor can be determined either by using a strong $\alpha$ line produced in the reaction, or by using an external source. In this work, all the position-energy corrections were performed "internally" using $\alpha$ lines produced during the experiment. A 2-dimensional matrix is produced, where the vertical (y) position of the event is plotted on the x-axis, against the $\alpha$ energy on the y-axis. Events of the same energy then form a line, the gradient of which is fitted. This gradient is then used to correct the energy in the following manner:

$$E_\alpha\,(new) = E_\alpha\,(old) + [m \times y]\,, \tag{4.1}$$

where

$$y = C \times \frac{bottom\ energy\ signal}{sum\ energy\ signal}. \tag{4.2}$$

In the above, $m$ is the fitted gradient from the 2-dimensional matrix, $y$ is the vertical position in the strip and $C$ is a constant which determines the maximum number of pixels in the y-direction, and is usually chosen to be 900 or 1024. It should be noted however, that the position resolution in the y-direction is such that the effective number of pixels is much lower than this value.

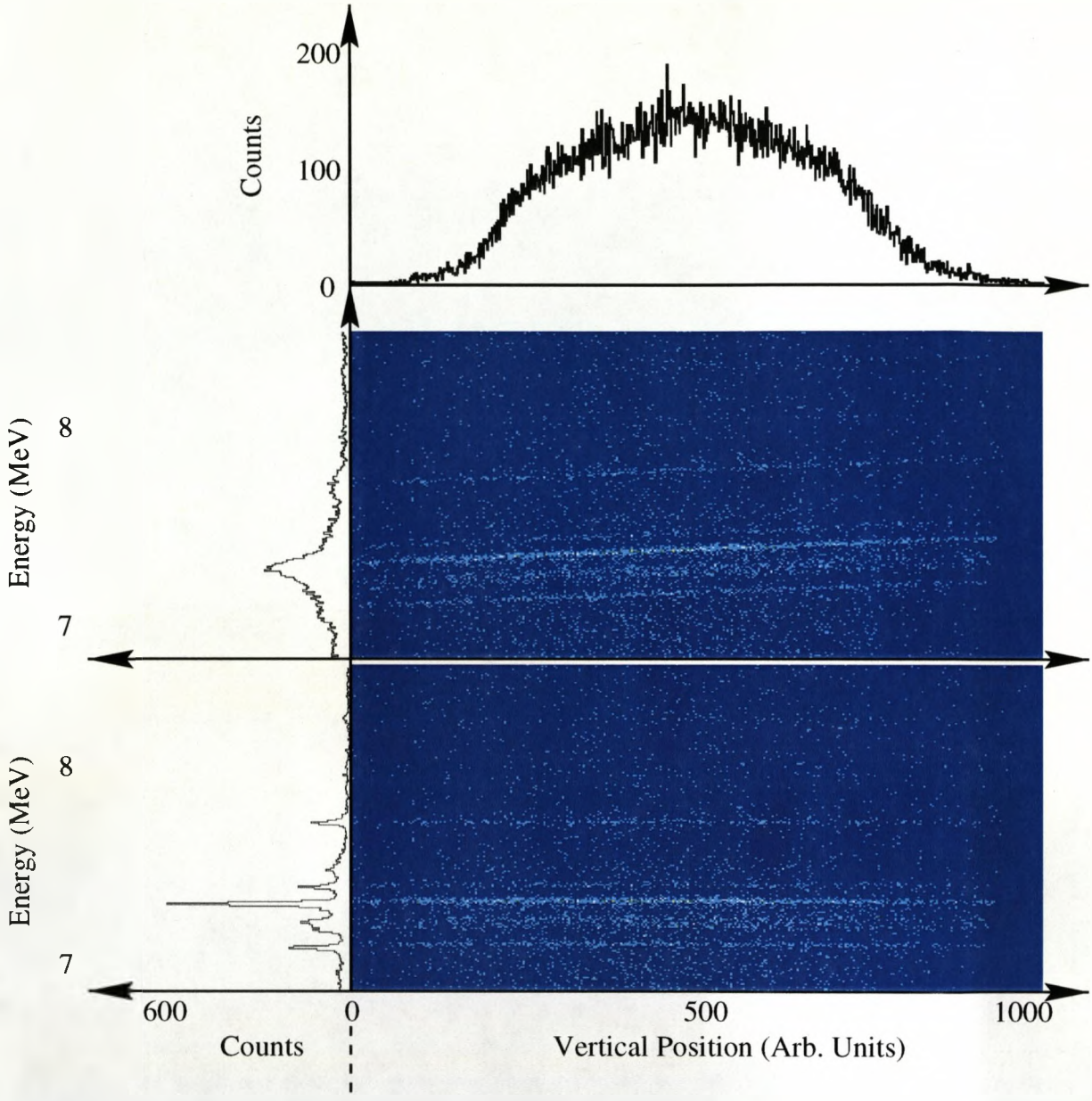


**Figure** 4.4: The position-energy corrections. The observed $\alpha$ energy is dependent on the vertical position at which the event occurred in the Si-strip detector. On the right-hand side is a 2-dimensional plot of the y-position against $\alpha$-particle energy. To the left are projections showing the $\alpha$-particle energy spectra. The upper part of the figure shows the spectra obtained before correction; the lower part that after correction. The improvement in energy resolution should be noted.

The effect of performing these position-energy corrections on the $\alpha$ spectra is shown in figure 4.4. The 2-dimensional plot in the upper part of the figure shows that obtained with no position-energy correction; the position dependence can clearly be observed. To the left and above the matrices are the $\alpha$ energy and y-position spectra, respectively. The poor energy resolution in the raw energy spectrum is improved greatly after the correction is applied. The FWHM energy resolution is typically around 30 keV for 7 MeV $\alpha$ decays after correction.

### 4.2.2 Energy Calibrations

The energy calibration of the RITU Si-strip detector can be performed again by using either an external source which provides more than one $\alpha$-decay line, or "internally" using known activities produced in the reaction. Using an external source suffers from the problem of energy losses due to the source and detector windows, the extent of which is dependent on the angle of incidence at the detector. Thus, in this work the detector is calibrated internally. This method is limited by the fact that the $\alpha$ decay lines that can be used often lie in a small energy region. Since the $\alpha$ decay occurs within the detector, the observed energy is a sum of the kinetic energy of the $\alpha$ particle plus the recoil energy given to the residual nucleus in the decay. In some cases, it is necessary to make a correction for the different recoil energy given to the residual nucleus (if, for example, the $\alpha$-decay line of interest lies several MeV from the calibration region). The $\alpha$-decay lines used in the calibration of RITU Si-strip detector spectra shown in this chapter were: $^{224}$Th 7.170(10) MeV, $^{211}$Po 7.4503(5) MeV, $^{219}$Ra 7.675(5) MeV, $^{222}$Th 7.982(8) MeV and $^{215}$Rn 8.674(8) MeV [Akovali 98, Browne 92, Artna-Cohen 91].

#### The RITU Si-strip Detector Spectrum

The total RITU Si-strip detector spectrum after correction for the position-energy dependence and energy calibration is shown in figure 4.5. The broad distribution of events centred at approximately 5 MeV corresponds to the implantation of fusion-evaporation residues. The inset to figure 4.5 shows an expansion of the $\alpha$-decay

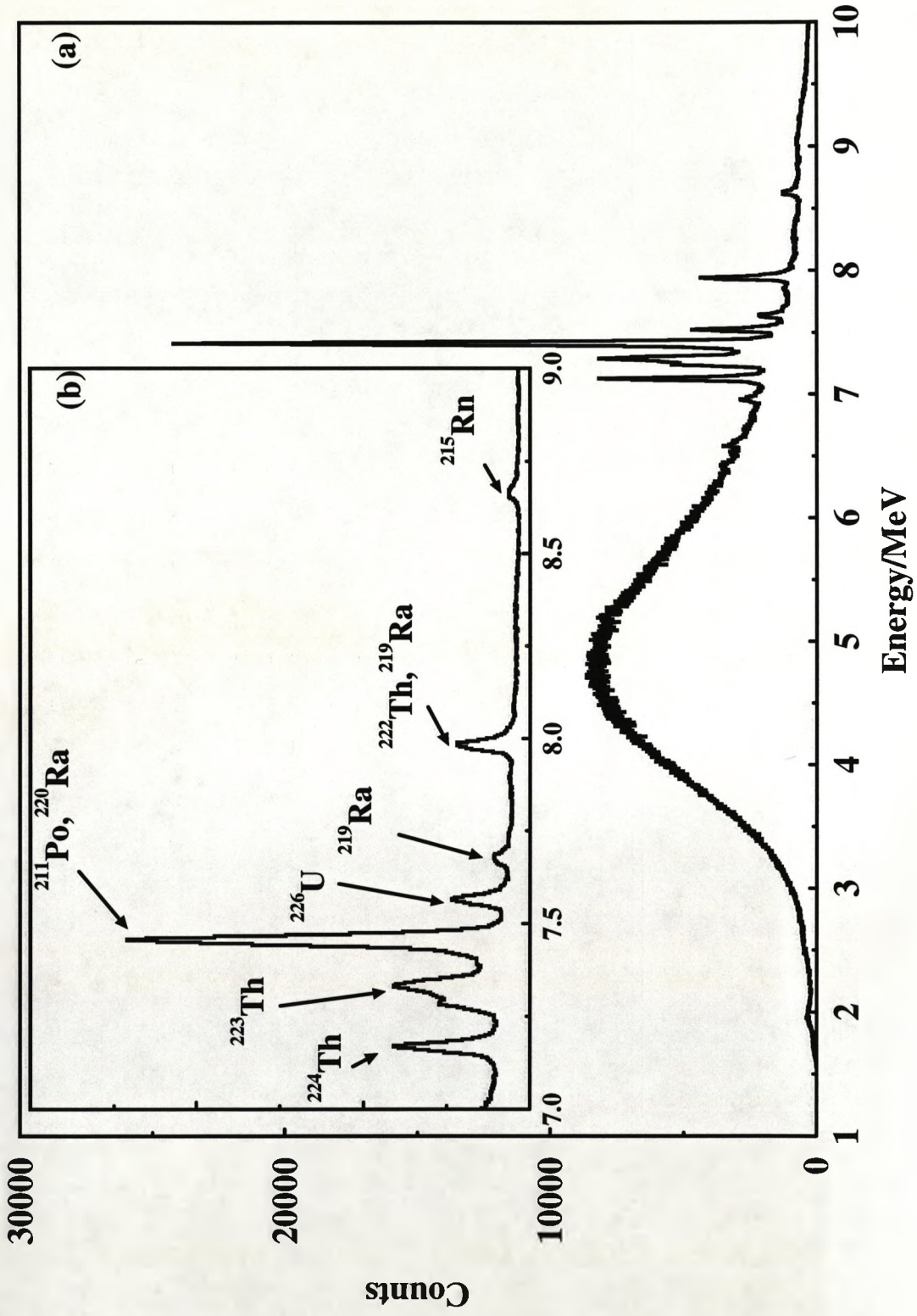


**Figure** 4.5: (a) Total RITU focal plane Si-strip detector spectrum for the reaction $^{22}$Ne + $^{208}$Pb at a centre-of-target bombarding energy of 111 MeV. The energy calibration is based on the known $\alpha$ activities produced. (b) Expansion of the $\alpha$ decay region.

region. It can be seen that the spectrum is dominated by the decay of implants from the $\alpha xn$ channels to isotopes of thorium. However, the angular acceptance of the RITU device means that the efficiency for collection of evaporation residues after $\alpha xn$ emission is greatly reduced when compared to that for the $xn$ channels (see cross section measurements, section 4.1). This suppression of the $\alpha xn$ channels is due to the effect of $\alpha$-particle emission on the recoil cone. The data obtained in the experiment do not allow a direct measurement of the transmission efficiency of the RITU device (for example, from comparison of total singles and recoil-gated prompt $\gamma$-ray spectra). However, the suppression factor may be estimated from a comparison of the $\alpha$-decay yields of $^{226}$U and $^{224}$Th. The yield of $^{226}$U, assuming a transmission efficiency of 10% for the $^{226}$U recoils, is consistent with a cross section of approximately 6 $\mu$b. The cross section measurements given in figure 4.1 show that the production of $^{224}$Th should be approximately a factor of 50 greater than $^{226}$U. The $\alpha$-decay yield of $^{224}$Th is however, only a factor of three greater than that of $^{226}$U. Thus the transmission efficiency for $^{224}$Th recoils is estimated to be less than 1%.

The energy of the $^{226}$U ground state to ground state $\alpha$ decay line was previously measured as 7.570(20) MeV [Andreyev 89]. Using the data presented here, a value of 7.565(5) MeV is obtained. The total number of events in the energy region corresponding to the 7.565(5) MeV $^{226}$U$\rightarrow^{222}$Th ground state to ground state $\alpha$ decay is $\simeq 6\times10^{4}$. The number in the fusion-evaporation product distribution is $\simeq 5\times10^{6}$.

### 4.2.3 The Correlation Method

In order to extract the $^{226}$U fusion-evaporation residues, the method of delayed coincidences, alternatively named the correlation method, was employed. This technique was first used to identify previously unknown isotopes of Pa in experiments performed using the velocity filter SHIP at GSI, Darmstadt [Schmidt 79]. The use of delayed coincidences is made possible by the position sensitivity of the RITU Si-strip detector, together with the fact that each event in the detector is labelled with a 1 $\mu$s resolution time stamp. Pairs of successive events are selected, with the constraint that the events

must occur at the same position in the detector, within a specified time window. This time window is known as the "search-time", and is normally selected to correspond to about 3 half-lives of the decay in question. Further selection of events of interest can be made by demanding that only events within certain energy ranges are allowed to enter the correlation. For the case of $^{226}$U, the first event corresponds to the observation of a recoil (energy range approximately $2 \rightarrow 7$ MeV), the second a subsequent event whose energy lies within the range ($7527 \rightarrow 7606$) keV. This energy corresponds to the 7.565(5) MeV $^{226}$U$\rightarrow^{222}$Th ground state to ground state $\alpha$ decay. The search time used was 800 ms, yielding approximately 25000 correlated recoil-$\alpha$ pairs. The position sensitivity of the RITU detector can be determined through analysis of the accidental correlations. In this particular experiment the position sensitivity was such that the detector was effectively divided into 60 pixels. The accidental correlations will be discussed further below. Prompt $\gamma$ rays associated with the correlated $^{226}$U fusion-evaporation residues are extracted from the data by selecting only those events which form the prompt part of the recoil-$\gamma$ TAC spectrum. The resulting spectrum is shown in figure 4.11.

An indication of the selectivity of the correlation technique is given by figure 4.6. The upper panel shows the total Si-strip detector spectrum in the region 7.0 to 8.5 MeV. It can be seen that the $\alpha$-decay peaks sit on a large background, which is due to the high-energy tail of the fusion-evaporation distribution, scattered beam particles and escaping $\alpha$ particles from higher energy peaks. The middle panel shows those events which are correlated to an event in the fusion-evaporation distribution within a search time of 800 ms. The background under the $\alpha$-decay peaks is reduced considerably. The lower panel shows events extracted in a similar manner, with the additional constraint that the fusion-evaporation residue must have an associated prompt $\gamma$ ray.

## Accidental Correlations

In any analysis which employs the use of delayed coincidences, there exists the possi-

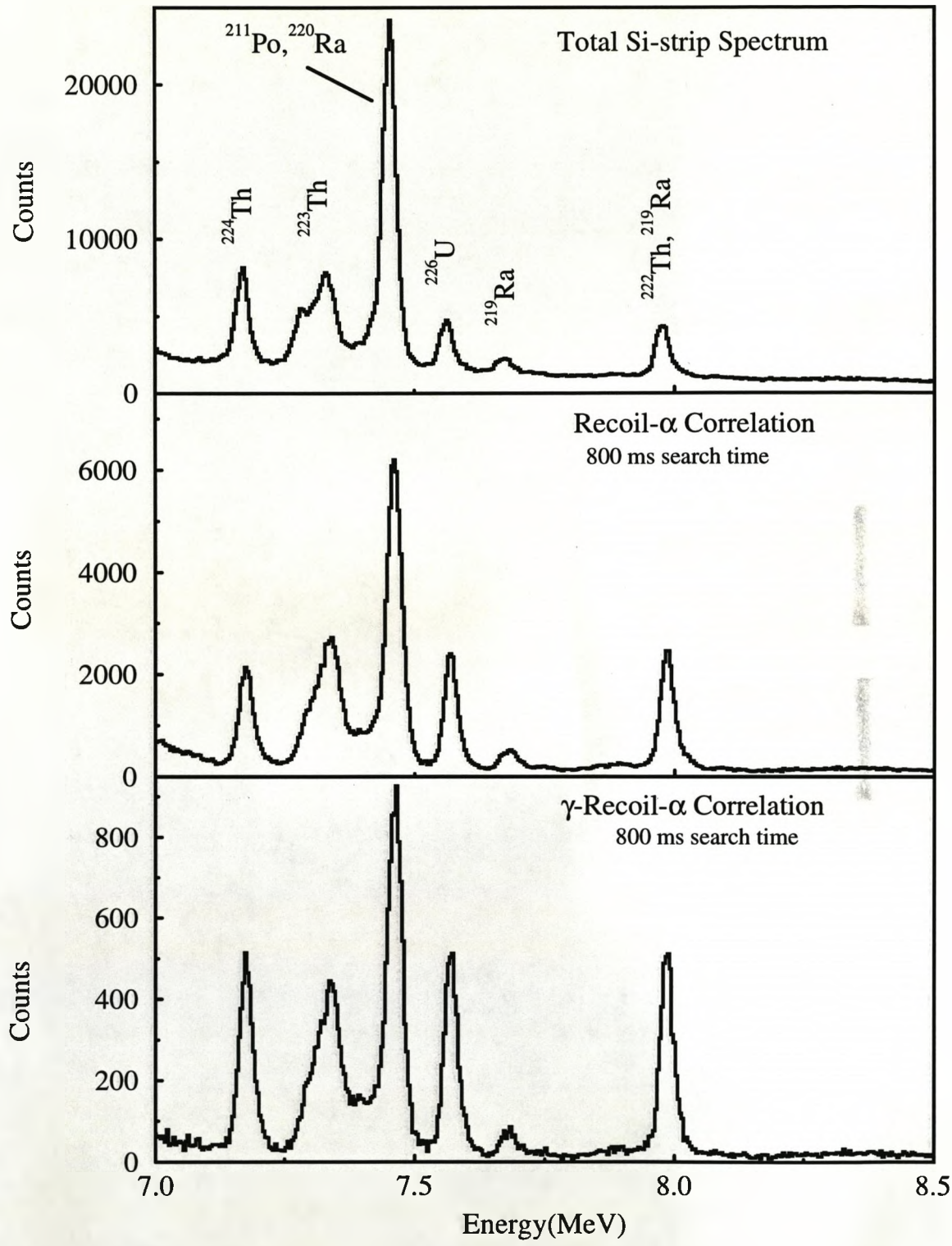


**Figure** 4.6: Reduction in background through use of the correlation technique. Upper panel: total Si-strip spectrum. Note the large background under the $\alpha$-decay peaks. Middle panel: those events correlated to an event in the fusion-evaporation residue distribution within a search time of 800 ms. Lower panel: as in middle panel, but with the additional condition that the fusion-evaporation residue must have an associated prompt $\gamma$ ray.

bility that a pair of events which satisfy the search criteria may not be a true recoil-$\alpha$ or $\alpha$-$\alpha$ pair. If the half-life of the decay under investigation is comparable to the average time between events in a particular pixel of the detector, then the accidental correlations may become significant. The accidental correlations mainly arise through two sources: (i) the dead time of the acquisition system resulting in non-observation of the recoil implant, and thus the observed $\alpha$ decay is associated with a recoil implant that occurred earlier in the pixel; (ii) the observed $\alpha$ decay does not belong to the last recoil implant in the pixel, but to a recoil which was implanted earlier in the pixel [Leino 81]. A careful investigation of these accidental correlations is necessary in order to ascertain the degree to which the accidental correlations contribute to the final $\gamma$-ray spectrum. The number of accidental correlations per pixel expected for a given set of search criteria can be estimated using the following formula:

$$N_{acc} = DR_{recoil}R_{decay}T \tag{4.3}$$

where $D$ is the duration of the experiment, $R_{recoil}$ is the average counting rate per pixel of accepted recoil implants, $R_{decay}$ is the corresponding rate per pixel of accepted decay events and $T$ is the search time. The actual number of accidental correlations can also be determined from the experimental data. This is achieved by performing the search for correlated events with the same search criteria as that for the normal search, but searching for pairs of events such that they occur in adjacent strips in the detector. Using this technique the number of accidentally correlated events associated with the search criteria detailed above was found to be approximately 3500. Thus approximately 14% of the total number of correlated events correspond to accidental correlations. The number of accidentally correlated events is then used with formula 4.3 in order to deduce the effective number of pixels given above.

In order to determine the effect of the accidental correlations on the $\gamma$-ray spectrum, a prompt recoil-$\gamma$ coincidence was also demanded of those recoils satisfying the accidental correlation search criteria. The number of $\gamma$-ray events found was approximately 90. The total number of $^{226}$U $\alpha$-decay tagged $\gamma$-ray events was approximately 4000. Thus the effect of the accidental correlations is small when a recoil-$\gamma$ coinci-

dence is demanded. The contribution is effectively reduced to 2% compared to 14% if the recoil-$\gamma$ coincidence is not demanded.

### 4.2.4 Determination of the $^{226}$U $\alpha$-Decay Half-Life

In order to correctly determine the half-life of the $\alpha$ decay of $^{226}$U, a correlation was performed with a search time of 36 seconds. Using a search time of this length allows the full decay curve to be fitted. The spectrum obtained is shown in figure 4.7. The

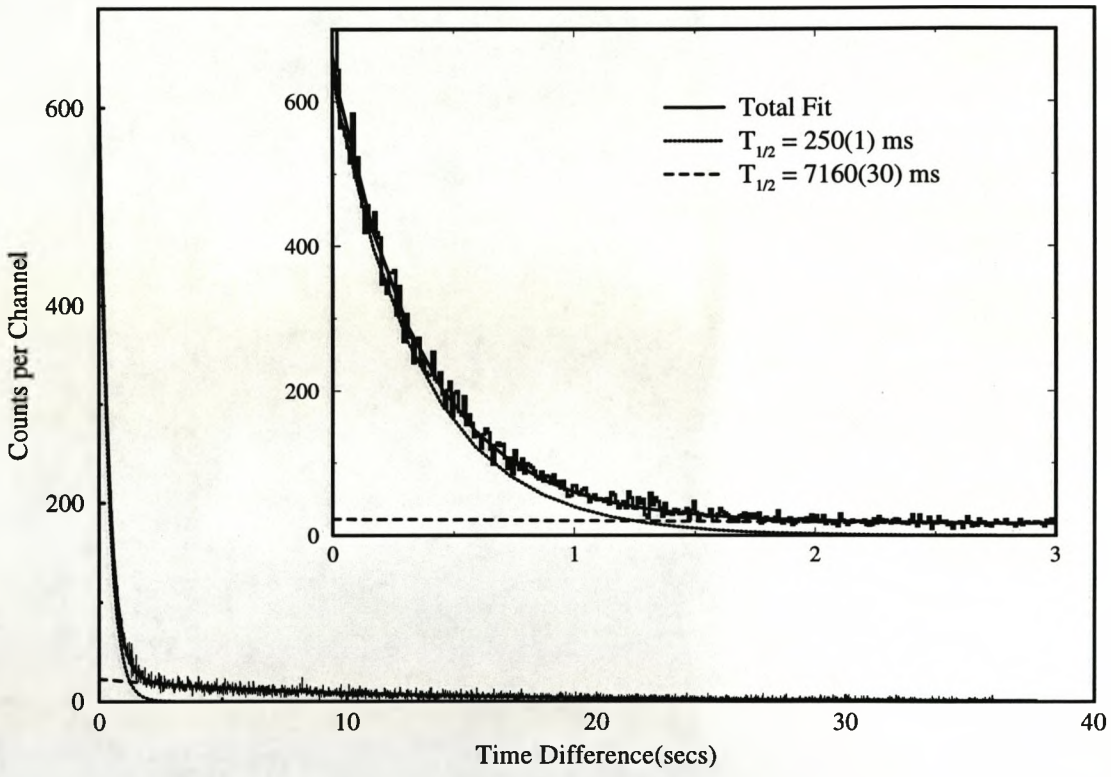


**Figure** 4.7: Time difference spectrum of all correlated recoil-$\alpha$($^{226}$U) events within a maximum search interval of 36 seconds. The fits shown are obtained using a least-squares two-component exponential fit. The inset shows an expansion of the region from 0 to 3 seconds.

accidental correlations also play an important role when determining the half-life for a particular decay. If the time difference between correlated events is plotted, the accidental correlations produce a long-lived exponential component in the decay

curve.

This additional component must always be taken into account when determining the real half-life for the decay. The apparent half-life for this additional component is determined by the average count rate of accepted recoil and $\alpha$ events [Leino 81]. The real half-life is determined through use of the following equation:

$$\lambda_{obs} = \lambda_{real} + r \tag{4.4}$$

where $\lambda_{obs}$ is the observed decay constant, $\lambda_{real}$ is the real decay constant and $r$ is the average counting rate per pixel of the accepted recoil and $\alpha$ events. The average counting rate per pixel, $r$, obtained from the experimental data was 0.08 $s^{-1}$, which gives a "half-life" of $ln2/r$ = 8662 ms. The "half-life" of the additional component can also be determined from the spectrum of time differences. The value obtained, 7160 ms, compares reasonably well to that from the detector counting rate. Using the half-life values given from decay curve fits over various time ranges, together with equation 4.4, the real half-life for the $\alpha$ decay of $^{226}$U was extracted. The value obtained: $T_{1/2}$ = 260(10) ms for the $E_\alpha$ = 7565(5) keV transition, is consistent with those previously published, see table 4.1.

| $E_\alpha$ (keV) | $T_{1/2}$ (ms) | Reference |
|---|---|---|
| 7565(5) | 260(10) | This Work |
| 7570(20) | 200(50) | [Andreyev 89] |
| 7566(20) | $160^{+21}_{-17}$ | [Enqvist 97]† |

Table 4.1: Previously published values of the $^{226}$U ground-state to ground-state $\alpha$-particle energy and half-life. († These data were recently re-evaluated, producing a half-life of 250(40) ms [Kuusiniemi 99].)

## 4.3 JUROSPHERE Gamma-Ray Spectra

### 4.3.1 The Recoil-$\gamma$ TAC

The prompt $\gamma$ rays collected by the JUROSPHERE array of Ge detectors are associated with the recoil events in the RITU Si-strip detector through use of a time-to-amplitude converter, or TAC. The TAC is started by a logic signal which indicates the presence of an event in the Si-strip detector and stopped by a similar signal which indicates the presence of an event in the JUROSPHERE array. Though the master trigger is set up such that events are only read out when there is an event in the Si-strip detector, the width of the coincidence gates in the electronics means that it is possible for events which are not in genuine prompt coincidence to be read out. The truly prompt events form a peak in the recoil-$\gamma$ TAC spectrum. The prompt $\gamma$ rays can be extracted by selecting only those events which form the peak. Two examples of TAC spectra obtained in this measurement are shown in figure 4.8. The upper panel shows those TAC events associated with all Si-strip detector events in the energy region corresponding to the fusion-evaporation products. The master trigger conditions dictate that the recoil-$\gamma$ TAC is also started by events such as $\alpha$ decays and scattered beam particles. Therefore such events contribute to the total TAC spectrum. Their effect can be reduced through use of energy coincidence gates on the Si-strip detector spectrum and the correlation technique. The TAC spectrum corresponding to those fusion-evaporation events correlated to the 7.565 MeV $\alpha$ decay of $^{226}$U is shown in the lower panel of figure 4.8. An additional reduction in the background can be obtained by applying a transformation to the TAC events. The upper panel of figure 4.9 shows a matrix with the recoil energy on the y-axis and the associated TAC events on the x-axis (essentially an energy versus time-of-flight plot). It can be seen that there is a correlation between the recoil energy and the TAC spectrum. Correcting for this dependence results in a reduction of the background under the prompt TAC peak. The result of such a correction is shown in the lower panels of figure 4.9. The lowermost panel shows a projection of the corrected matrix onto the x-axis. Note that the width

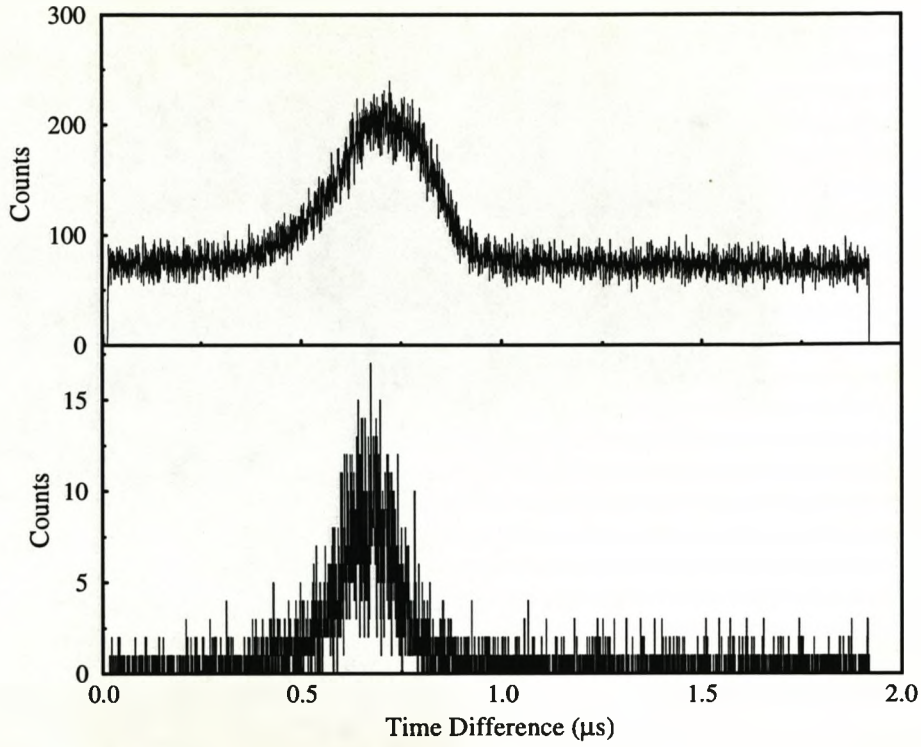


**Figure** 4.8: Recoil-$\gamma$ TAC spectra. Upper panel: TAC events in coincidence with all fusion-evaporation residues. Lower panel: TAC events in coincidence with those fusion-evaporation residues correlated to the 7.565 MeV $\alpha$ decay of $^{226}$U within a search time of 800 ms. The full range of the TAC was set to 2 $\mu$s.

of the prompt peak is reduced. Using the prompt events in the corrected recoil-$\gamma$ TAC spectrum gives an improvement of approximately 10% in the peak-to-total ratio of the final $\gamma$-ray spectrum.

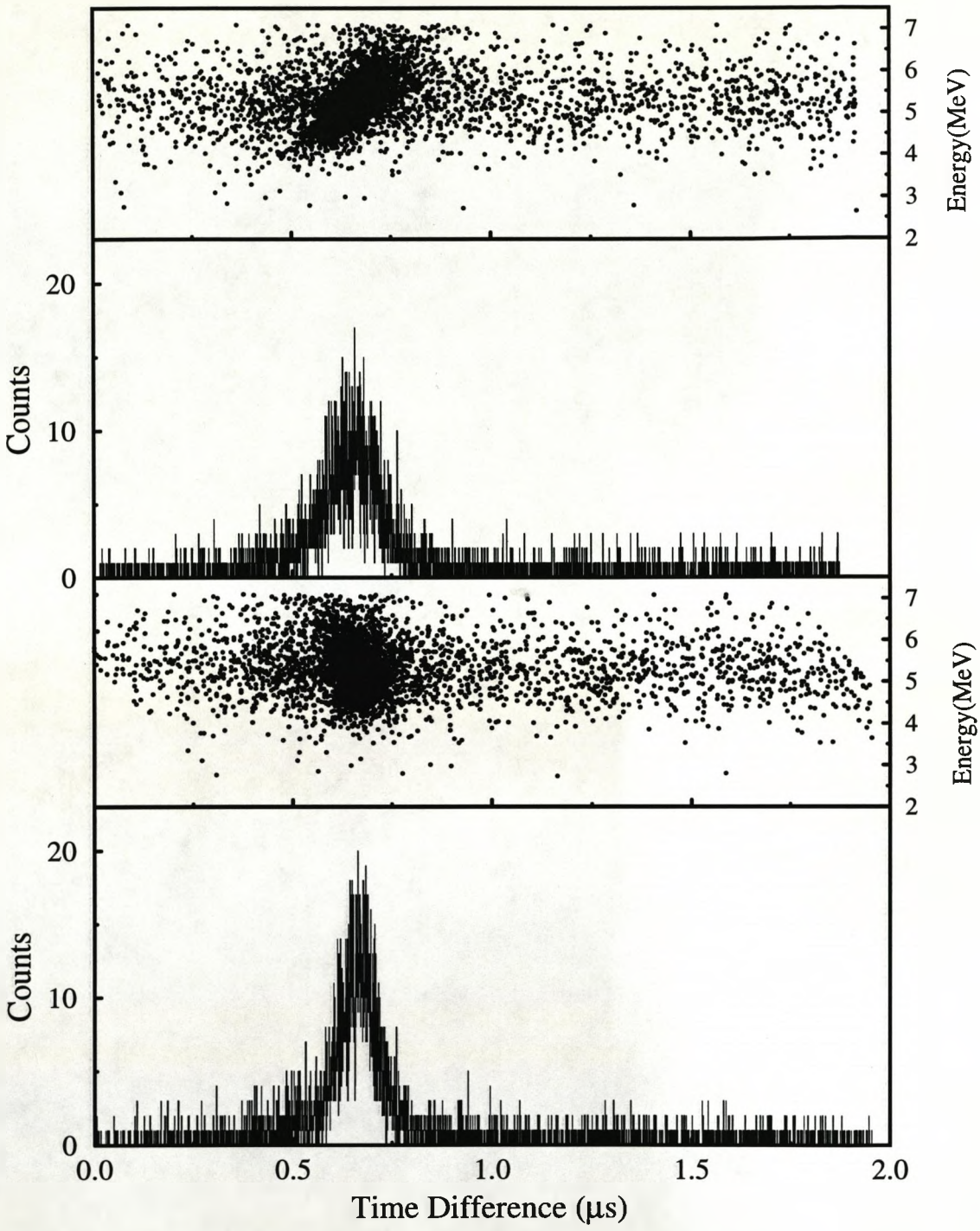


**Figure** 4.9: Upper panels: Matrix of recoil energy against recoil-$\gamma$ TAC events and corresponding recoil-$\gamma$ TAC spectrum. Applying a transformation to the TAC events reduces the background under the prompt recoil-$\gamma$ TAC peak. Lower panels: Corrected matrix and corresponding recoil-$\gamma$ TAC spectrum.

A spectrum of prompt single-fold $\gamma$-ray events associated with all events in the fusion-evaporation distribution is shown in figure 4.10. In this spectrum, no subtraction is made to remove events due to the background under the prompt peak. Peaks marked with open squares correspond to transitions in $^{223}$Th, those with filled squares to transitions in $^{224}$Th and those with stars to transitions assigned to $^{226}$U (see sections 4.3.2 and 4.5). X-ray transitions are marked by the appropriate chemical symbol. Here again the dominance of the $\alpha xn$ channels to isotopes of Th can be seen.

### 4.3.2 The $^{226}$U Gamma-Ray Spectrum

The spectrum of $\gamma$-ray energies which are in prompt coincidence with recoils correlated to the $\alpha$ decay of $^{226}$U is shown in figure 4.11. The search parameters used to generate this spectrum are those discussed in section 4.2.3. This spectrum was calibrated using known $\gamma$-ray transitions from a mixed $^{133}$Ba and $^{152}$Eu source. An additional angle-dependent correction is applied to account for the Doppler shift in the energy due to the recoil velocity. It can be seen that there is a regular, rotational-like sequence of transitions with energies 168.7, 233.3, 283.6, 325.6, 362.2 and 393 keV. In addition to this sequence, there is a set of relatively intense, irregular transitions at lower energies (140.6 185.7, 191.1, 197.0 keV, for example). Structures such as these are typical of those seen for nuclei which are known to have strong octupole correlations (see for example the spectra in refs. [Smith 95, Ackermann 93, Cocks 99]).

#### Analysis of Background Contributions

The total $^{226}$U $\gamma$-singles spectrum shown in figure 4.11 is not corrected for background from adjacent $\alpha$ peaks. In order to ascertain the contribution from the tails of nearby $\alpha$ peaks, the spectrum shown in figure 4.12 was created. This spectrum was generated in an identical manner to that of figure 4.11, but demanding that the events subsequent to a recoil implant must have an energy in the ranges (7487 $\rightarrow$ 7527) keV and (7606 $\rightarrow$ 7646) keV. Peaks marked with an 'X' correspond to transitions assigned to $^{226}$U, and those marked with an asterisk correspond to transitions in $^{224}$Th. The

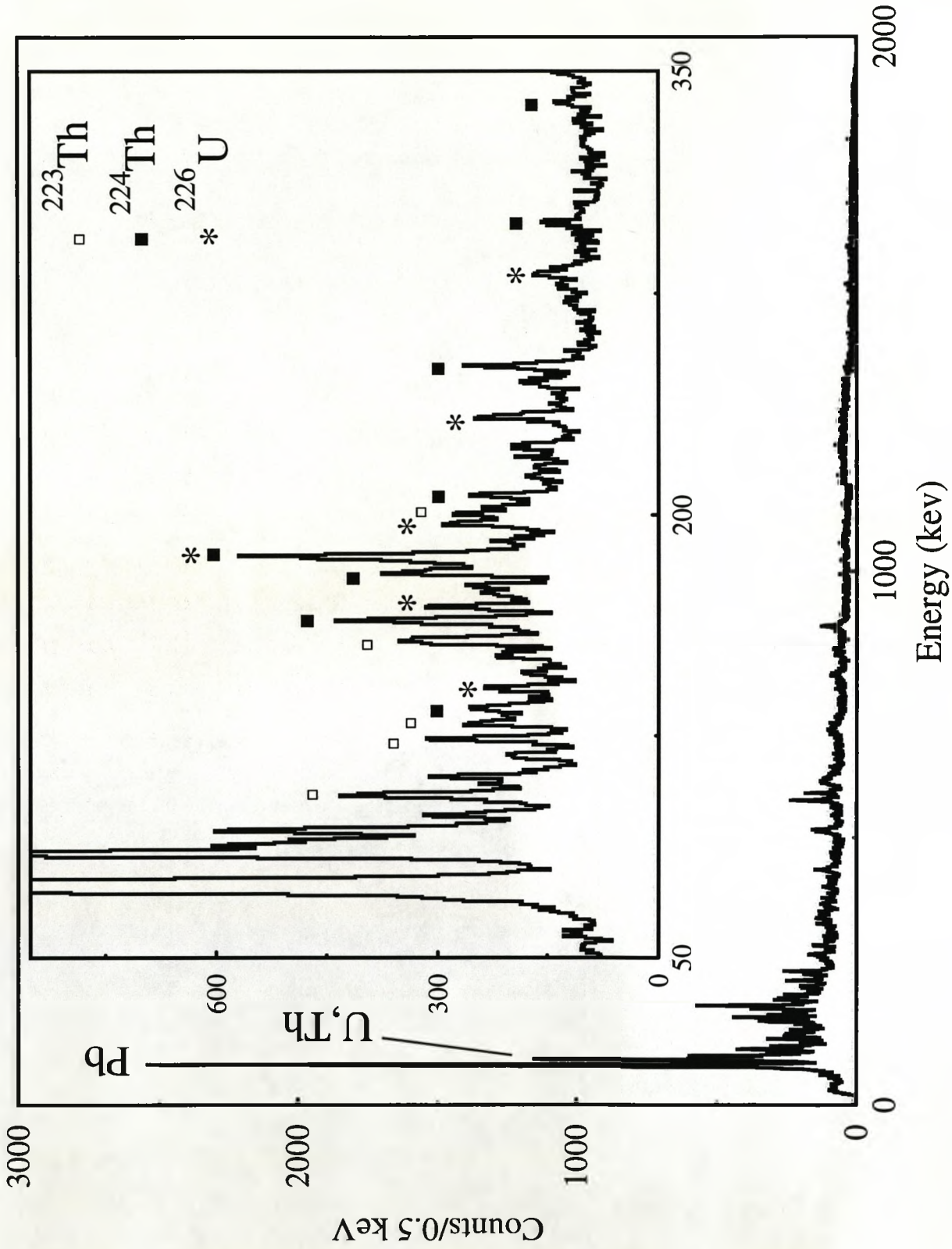


**Figure** 4.10: Total spectrum of singles $\gamma$ rays collected by the JUROSPHERE Ge detector array. All $\gamma$ rays are in prompt coincidence with a fusion-evaporation event in the RITU focal plane Si-strip detector. The inset shows an expansion of the 50 to 350 keV region. Chemical symbols denote X-rays from the given element.

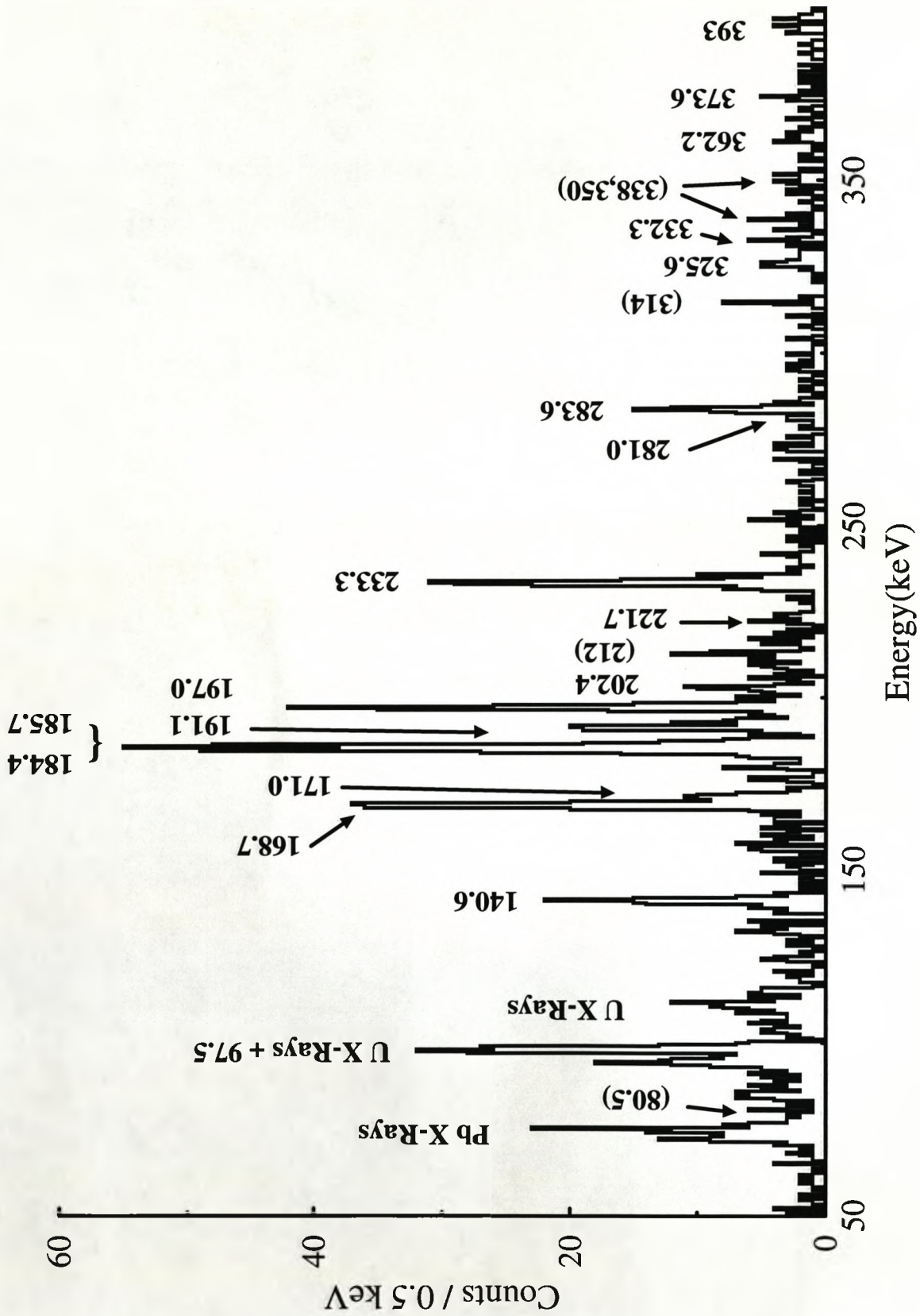


**Figure** 4.11: Single fold $\gamma$-ray energy spectrum in coincidence with fusion-evaporation events correlated to the $\alpha$ decay of $^{226}$U.

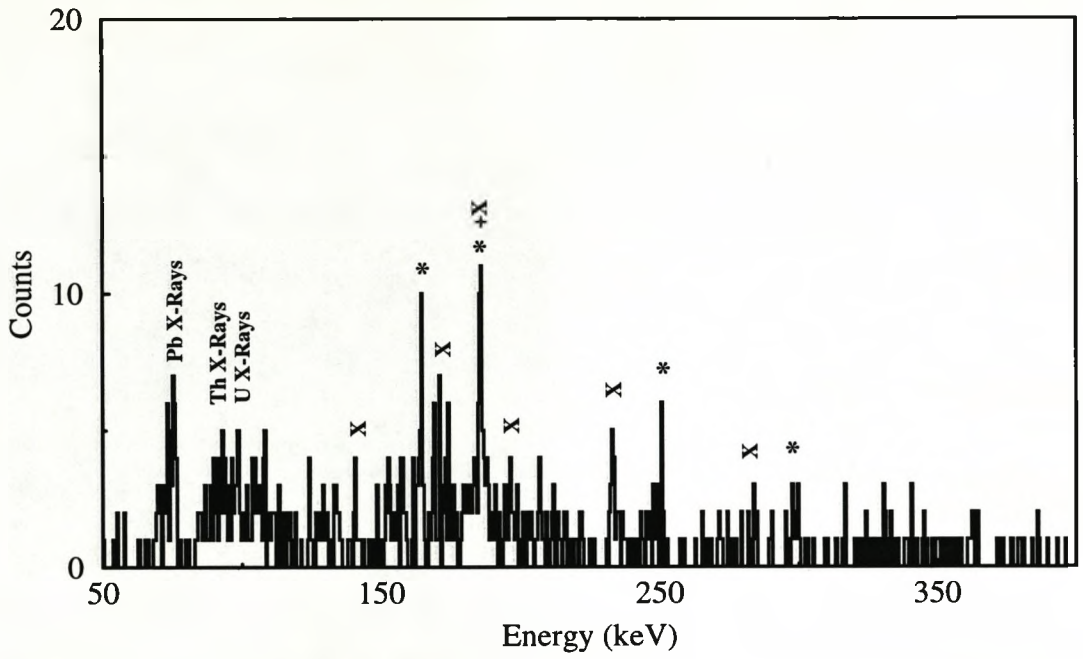


**Figure** 4.12: Spectrum of prompt $\gamma$-rays coincident with recoils correlated to the background on either side of the $^{226}$U $\alpha$-decay peak. Peaks labeled with an 'X' correspond to transitions in $^{226}$U, those with an asterisk to transitions in $^{224}$Th. See text for details.

observation of transitions in $^{224}$Th is due to the contribution from the tail of the $\alpha$-decay peak of the $^{224}$Th daughter nucleus, $^{220}$Ra. Here the second event in the recoil-$\alpha$-$\alpha$ chain, the $\alpha$ particle from the decay of $^{224}$Th, escapes from the detector and is not registered. Thus, it can be seen that the contribution from nearby $\alpha$ peaks is extremely small.

The spectrum shown in figure 4.11 is also not corrected for the contribution from background events under the prompt recoil-$\gamma$ peak. An estimation of the contribution of events of this type can be obtained by producing spectra of $\gamma$ rays which are coincident with events on either side of the prompt TAC peak. Such spectra are shown in figure 4.13. The upper panel of this figure shows $\gamma$ rays coincident with events to the left-hand or "fast" side of the prompt peak. The lower panel shows $\gamma$ rays coincident with events to the right-hand or "slow" side of the prompt peak. The gating conditions used to produce these spectra are such that the total gate width is

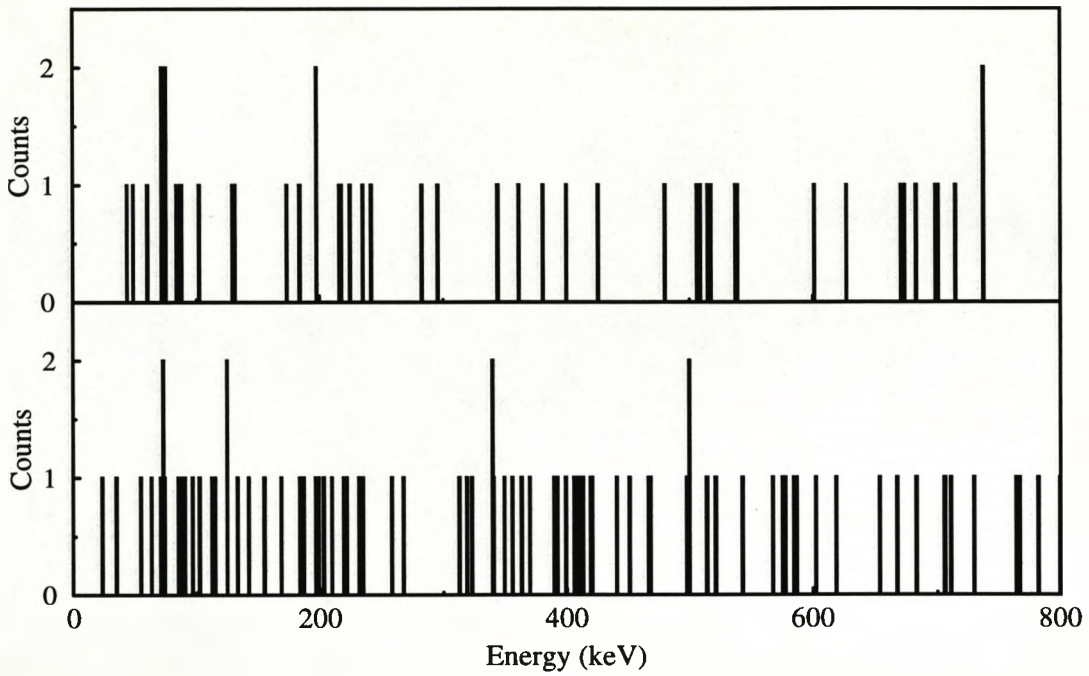


**Figure** 4.13: $\gamma$-ray spectra generated through gating on events on either side of the prompt TAC peak. Upper panel: $\gamma$-ray events coincident with events to the left-hand side of the prompt peak. Lower panel: $\gamma$-ray events coincident with TAC events to the right-hand side of the prompt peak. The total TAC gate size for the spectra is normalised to that used to produce 4.11 on an equivalent channels basis.

normalised to that used to produce the prompt spectrum on an equivalent channels basis. It can be seen from these spectra that the contribution is again very small. Also, it is interesting to note that the large intensity of Pb X-rays is not accounted for by these spectra of randomly coincident $\gamma$ rays. Thus, the Pb X-rays which appear in figure 4.11 are genuinely in prompt coincidence with $^{226}$U recoils, presumably due to atomic collisions as the residual nucleus recoils through the remainder of the target.

## 4.4 The $\alpha$-Tagged $\gamma$-$\gamma$ Coincidence Data

It is of course possible that more than one $\gamma$ ray is recorded in coincidence with a given recoil. The $\gamma$ rays that are emitted in a cascade de-exciting the nucleus can

provide an insight into the structure of the level scheme. The fold distributions for the recoil-gated and $^{226}$U $\alpha$-tagged $\gamma$-ray data are presented in table 4.2. Events

| Fold | 1 | 2 | 3 | 4 | 5 | 6 |
|---|---|---|---|---|---|---|
| No. Events (Recoil-gated) | 191532 | 30585 | 3540 | 325 | 25 | 3 |
| No. Events ($^{226}$U $\alpha$-tagged) | 2929 | 523 | 67 | 3 | - | - |

Table 4.2: Fold distributions for the recoil-gated and $^{226}$U $\alpha$-tagged $\gamma$-ray data obtained in the present experiment.

of fold two or greater can be "unpacked" into a set of fold two data, and the data incremented into a 2-dimensional "matrix". By selecting an energy range on one axis (known as a "gate"), a spectrum of $\gamma$-rays coincident with the $\gamma$-rays of the selected energy can be produced. This is known as a gated projection. The $^{226}$U $\alpha$-tagged $\gamma$-$\gamma$ coincidence data obtained in this study were limited, corresponding to approximately 10% of the total $\gamma$-ray singles data. It is possible to obtain an improvement in the level of statistics by using those $\gamma$-$\gamma$ data which are coincident with any recoil event in the Si-strip detector. However, these data also include those events which are coincident with the recoils from the more abundant $\alpha xn$ channels corresponding to isotopes of thorium (see figure 4.10). The transition energies in the thorium isotopes are similar to those in $^{226}$U, thus the $\gamma$-ray lines attributed to $^{226}$U were obscured by those from the thorium isotopes. Typical spectra projected from the $\alpha$-tagged 2-dimensional matrix are shown in figure 4.14. The transition energies used as gates are shown in the upper right hand corner of each spectrum. Though the spectra contain few counts, it is possible to deduce which transitions are coincident with the gating transitions. A single count cannot be unambiguously assigned as being a photopeak, but a cluster of two or more counts is statistically unlikely to correspond to background. In the spectra shown in figure 4.14, italic labels denote a cluster of two or more counts, while

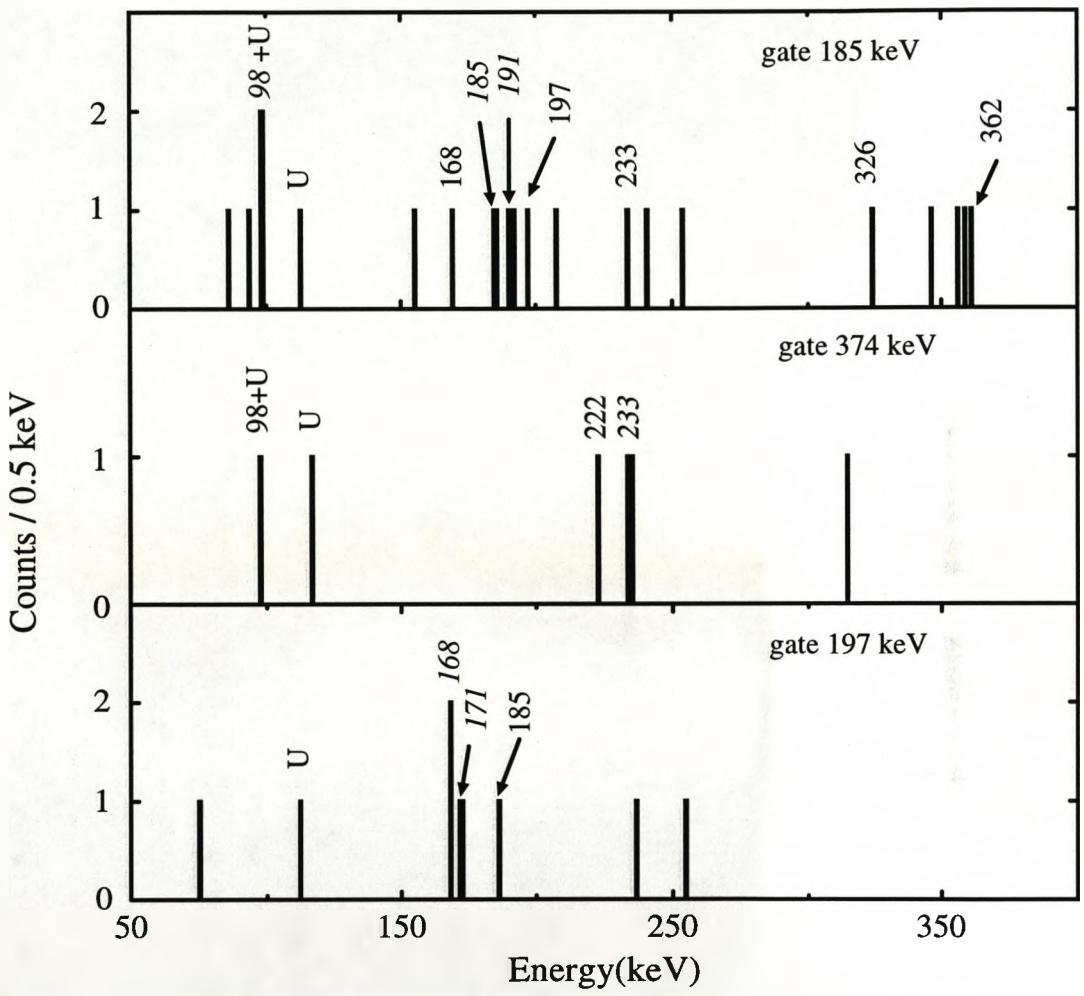


**Figure** 4.14: Sample projections from the $\alpha$-tagged $\gamma$-$\gamma$ coincidence data. The transition energy used as a gate is shown in the upper right hand corner of each panel. Italic labels denote two or more counts; those in normal font correspond to other transitions assigned in the level scheme. Counts not labelled are assumed to be background.

those in normal lettering correspond to photopeaks observed in the total $\gamma$-ray singles spectrum shown in figure 4.11. Those counts which are not labelled are assumed to be background. Following these assumptions, the deduced peak-to-total ratio is then the same as that for the $\gamma$-ray singles spectrum. Through an analysis such as this, it is possible to deduce a table of coincidences, shown in table 4.3. Using this information, together with the assumptions discussed in the following section, it was possible to deduce the level scheme of $^{226}$U for the first time.

| Gate (keV) | 169 | 171 | 185 | 191 | 197 | 233 | 374 |
|---|---|---|---|---|---|---|---|
| Coincident Transitions | 197 | 197 | 98, 185, 191 | 185, 233 | 168, 171 | 191, 374 | 233 |

Table 4.3: Table of coincidences obtained using the $^{226}$U $\alpha$-tagged $\gamma$-$\gamma$ data.

## 4.5 Deduced Level Scheme of $^{226}$U

The partial decay scheme deduced from the observed transitions in $^{226}$U is shown in figure 4.15. This scheme was produced through energy sum and intensity balance arguments. The measured transition energies, intensities and deduced multipolarities can be seen in table 4.4.

The tentative spins and parities are assigned through systematics of the $N = 134$ isotones and the assumption that the observed smoothly changing difference in transition energy for the sequence of transitions (80.5), 168.7, 233.3, 283.6, 325.6, 362.2 and 393 keV is characteristic of a band of $E2$ transitions based on the known $0^+$ ground state. This assumption presumes that there is no significant alignment or band crossing below a rotational frequency of around $\hbar\omega \simeq 0.2$ MeV. Such smooth alignment properties are also observed in the radium and thorium isotopes with $N \simeq 134$. A discussion of the reasons for these smooth alignment properties can be found in section 4.6. The assignment of 80.5 keV for the $2^+ \rightarrow 0^+$ transition is based on the

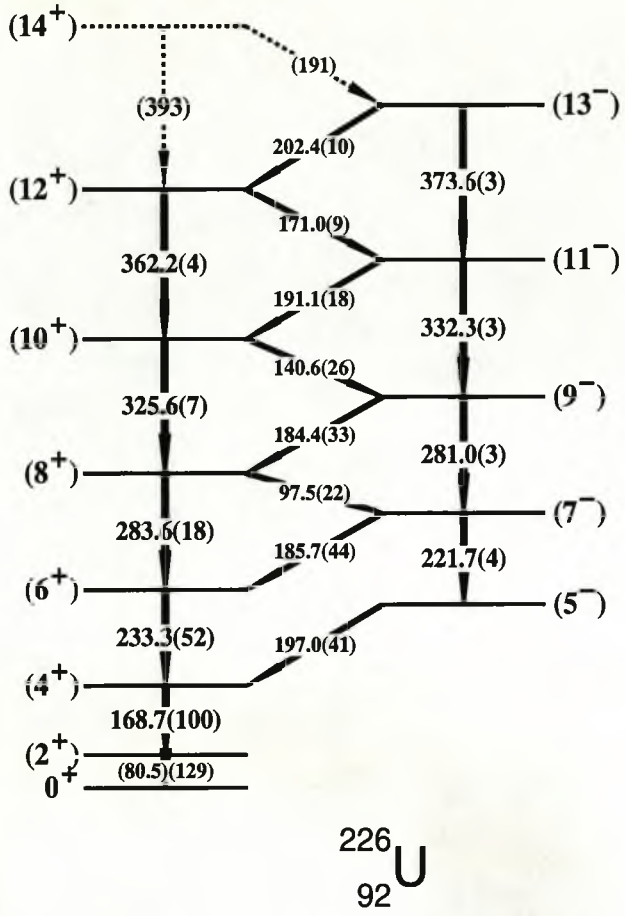


**Figure** 4.15: Partial level scheme of $^{226}$U. The figures in brackets are the measured transition intensities normalised to that of the $4^+ \rightarrow 2^+$ transition. The errors in the intensities and transition energies are detailed in table 4.4.

systematic trend of this transition energy in the heavier isotopes of uranium and in the isotopes of thorium, and the observation of a candidate peak with approximately the correct intensity. An experiment to determine the excitation energy of the $2^+$ state through the $\alpha$ decay of $^{230}$Pu is described in the next chapter. The transitions of energies 221.7, 281.0, 332.3 and 373.6 keV are assigned to be a band of electric quadrupole transitions based on the state tentatively assigned $I^\pi = 5^-$. The transitions of energies 197.0, 185.7, 97.5, 184.4, 140.6, 191.1, 171.0 and 202.4 keV are ordered and assigned dipole character through their energy sum with respect to the transitions assigned $E2$ character. The assignment of $E1$ character for these transi-

| $I_i^{\pi_i}$ | $I_f^{\pi_f}$ | Mult. | Energy (keV) | Intensity ($\gamma$) | Intensity (total) |
|---|---|---|---|---|---|
| $2^+$ | $0^+$ | E2 | (80.5(5)) | 17(6) | 530(190) |
| $4^+$ | $2^+$ | E2 | 168.7(6) | 170(30) | 410(70) |
| $6^+$ | $4^+$ | E2 | 233.3(3) | 149(12) | 214(17) |
| $8^+$ | $6^+$ | E2 | 283.6(4) | 60(12) | 74(15) |
| $10^+$ | $8^+$ | E2 | 325.6(4) | 24(5) | 28(6) |
| $12^+$ | $10^+$ | E2 | 362.2(4) | 14(5) | 16(4) |
| $7^-$ | $5^-$ | E2 | 221.7(5) | 10(3) | 15(5) |
| $9^-$ | $7^-$ | E2 | 281.0(4) | 10(4) | 12(5) |
| $11^-$ | $9^-$ | E2 | 332.3(4) | 11(4) | 13(5) |
| $13^-$ | $11^-$ | E2 | 373.6(4) | 10(3) | 11(3) |
| $5^-$ | $4^+$ | E1 | 197.0(2) | 154(14) | 170(15) |
| $7^-$ | $6^+$ | E1 | 185.7(5) | 160(50) | 180(50) |
| $8^+$ | $7^-$ | E1 | 97.5(5) | 60(20) | 90(30) |
| $9^-$ | $8^+$ | E1 | 184.4(5) | 120(34) | 130(40) |
| $10^+$ | $9^-$ | E1 | 140.6(3) | 89(9) | 109(11) |
| $11^-$ | $10^+$ | E1 | 191.1(4) | 67(12) | 74(13) |
| $12^+$ | $11^-$ | E1 | 171.0(4) | 33(10) | 38(11) |
| $13^-$ | $12^+$ | E1 | 202.4(4) | 37(6) | 41(7) |

Table 4.4: Table of the measured transition energies, intensities and deduced multipolarities. The $\gamma$-ray intensities are corrected using the energy-dependent total efficiency curve presented in figure 3.14. The total transition intensities are corrected using tabulated values of internal conversion coefficients [Rösel 78], assuming the multipolarity given.

tions is based on intensity balance arguments, after correction for internal conversion. For example, the total transition intensity feeding into the state assigned $I^{\pi} = (9^{-})$ would be an order of magnitude larger than that feeding out of the state, if the inter-band transitions feeding into and out of this state were magnetic dipole in nature. The assignment of a transition of energy 97.5 keV is deduced from the fact that the observed relative intensities of the 94.7 and 98.4 keV uranium X-rays are not consistent with the published values [Salem 74]. It is possible that the unassigned peak at 212 keV (see figure 4.11) could be the $3^{-} \rightarrow 2^{+}$ transition, and this assignment would be in good agreement with the systematic trend of this transition energy in the $N = 134$ isotones. However, as there is no observed candidate for the $5^{-} \rightarrow 3^{-}$ transition, this assignment is not made here. Also observed in the $\gamma$-ray energy spectrum is a peak at 314 keV, which cannot be placed in the partial level scheme presented.

## 4.6 Rotational Alignment Properties

The experimental aligned angular momentum, $i_x$, for the positive- and negative- parity bands of $^{226}$U is plotted as a function of rotational frequency, $\hbar\omega$, in figure 4.16. The rotational frequency is obtained using equation 1.7, and the experimental alignment using equation 1.34 (see chapter 1). The reference aligned angular momentum of the core is calculated using Harris parameters of $\mathcal{J}_0 = 31\ \hbar^2 MeV^{-1}$ and $\mathcal{J}_1 = 26\ \hbar^4 MeV^{-3}$. These parameters are the same as those used by Cocks *et al.* [Cocks 97], determined by fitting the low-spin transitions in $^{222}$Ra. Though there may be some mass dependence in the Harris parameters, it is neglected here. In figure 4.16, open circles represent the data for the positive-parity band, open diamonds the data for the negative-parity band. It can be seen that the aligned angular momentum is higher in the negative-parity band than the positive-parity band at low rotational frequencies, and the two become similar at higher rotational frequencies. The behaviour of the aligned angular momentum is smooth as a function of rotational frequency for both bands. As mentioned previously, smooth alignment properties such as these

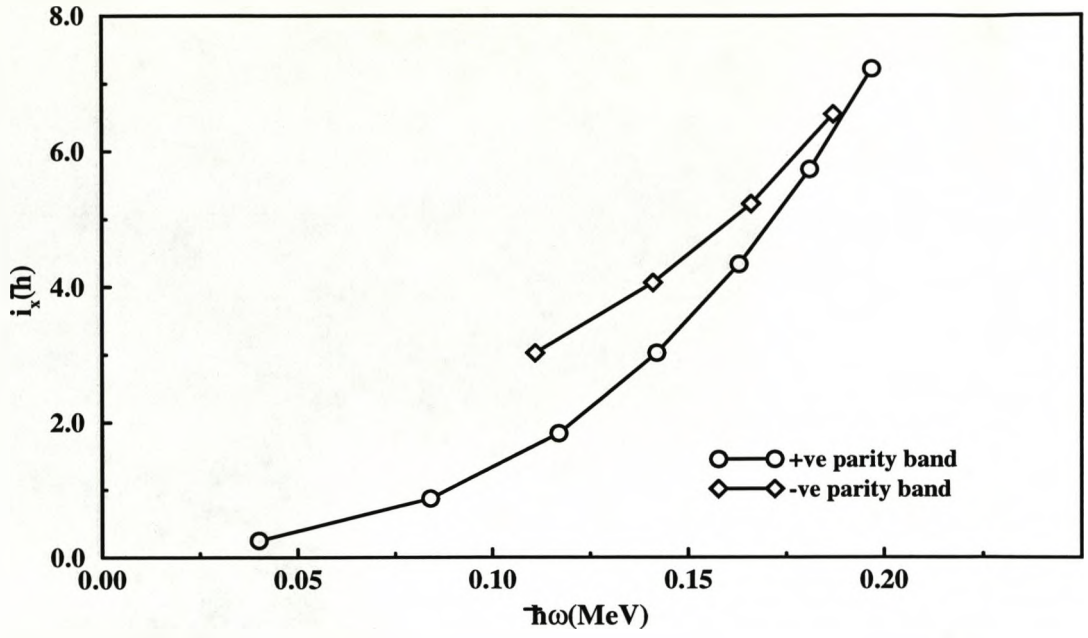


**Figure** 4.16: Plot of the aligned angular momentum as a function of rotational frequency for $^{226}$U. A reference aligned angular momentum for the core with Harris parameters of $\mathcal{J}_0 = 31\ \hbar^2 MeV^{-1}$ and $\mathcal{J}_1 = 26\ \hbar^4 MeV^{-3}$ has been subtracted.

are also observed in several isotopes of Ra and Th (e.g. $^{222,224,226}$Ra and $^{224,226}$Th, see [Cocks 99] for alignment plots). In these nuclei, the octupole couplings between the unique-parity orbitals and the normal-parity orbitals are strong, which results in a fragmentation of the aligned angular momentum over many quasiparticle states. This further means that the rotational frequency of the first band crossing is increased (see, for example, [Nazarewicz 85, Butler 96]). Figure 4.17 shows the difference in experimental aligned angular momentum, $\Delta i_x = i_x^- - i_x^+$, between the negative- and positive- parity bands as a function of rotational frequency, $\hbar\omega$, for the $N = 134$ isotones: $^{226}$U, $^{224}$Th, $^{222}$Ra and $^{220}$Rn. The plots were produced using the prescription described in section 2.2.2. The data used for $^{226}$U are taken from the present work, and those for $^{224}$Th and $^{222}$Ra, $^{220}$Rn from references [Ackermann 93, Cocks 97] respectively. The dashed lines at 0 and 3 $\hbar$ show the limits of $\Delta i_x$ expected for an octupole-deformed and an octupole-vibrational nucleus, respectively. Plots such as these can give further insight into the structure of the nucleus in question at different

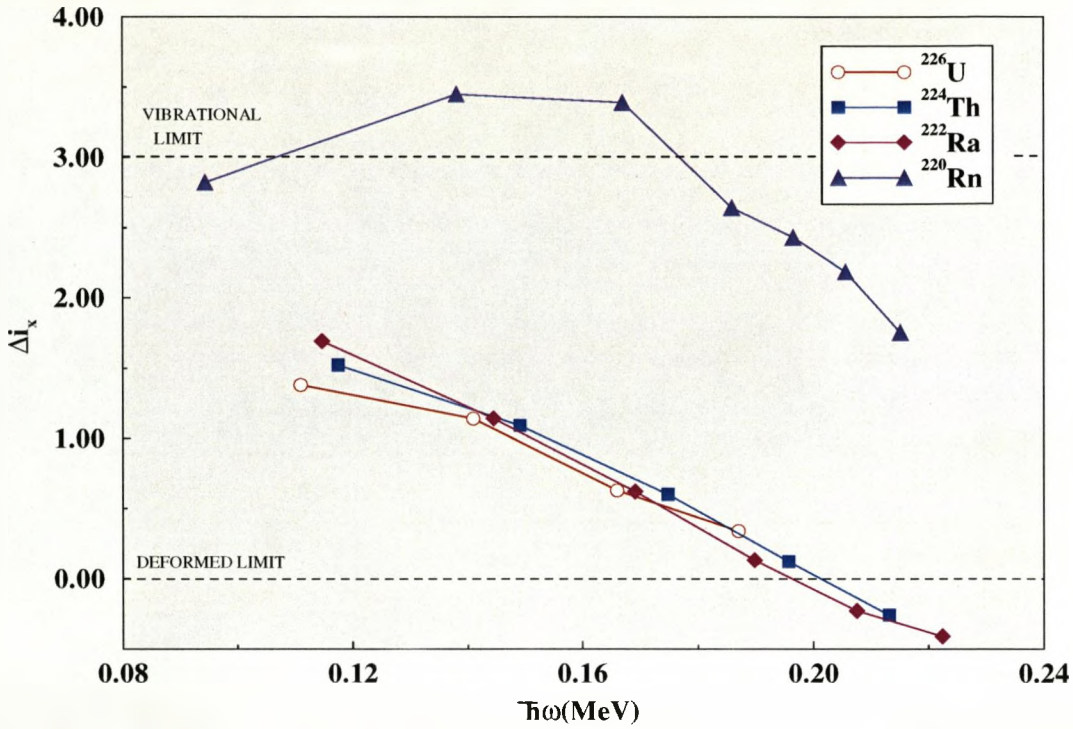


**Figure** 4.17: Plot of the difference in aligned angular momentum, $\Delta i_x = i_x^- - i_x^+$ against rotational frequency for the even-even $N = 134$ isotones, $Z = 86$ - 92. Data for $^{224}$Th and $^{222}$Ra, $^{220}$Rn are taken from refs. [Ackermann 93, Cocks 97] respectively.

rotational frequencies. It can be seen that the behaviour of $\Delta i_x$ for $^{226}$U follows closely that of $^{224}$Th and $^{222}$Ra. At low values of $\hbar\omega$, $\Delta i_x$ has a value of approximately 1.5 $\hbar$ and tends towards zero with increasing rotational frequency. The nuclei $^{224}$Th and $^{222}$Ra are considered to be octupole-deformed, as discussed earlier. Behaviour such as this may indicate that the octupole strength is enhanced as a function of rotational frequency. This enhancement, according to refs. [Nazarewicz 87, Egido 90], is due to increased moments of inertia for the octupole shape (which arises from a reduction in the pairing correlations) and increased octupole mixing between the opposite-parity single-particle states, which come closer together with increasing rotational frequency. This is in contrast with the observed behaviour of $^{220}$Rn, which is considered to be octupole-vibrational in nature. Here, the value of $\Delta i_x$ is approximately three over the full measured frequency range. This is consistent with the description of the

negative-parity states in terms of the coupling of an aligned octupole phonon to the positive-parity states. Further discussion of the alignment properties of several Rn, Ra and Th isotopes can be found in refs. [Cocks 97, Cocks 99] and references therein. From the observed behaviour of $\Delta i_x$ we can infer that $^{226}$U can be described as a rotating body with a reflection-asymmetric shape.

## 4.7 Measurement of Intrinsic Dipole Moment

The magnitude of the ratio of the intrinsic dipole to intrinsic quadrupole moment $|D_0/Q_0|$, was extracted from the experimental data through measurement of the $E1/E2$ $\gamma$-ray branching ratios, and the rotational model formulae given in equations 3.25 and 3.26 [Butler 96]. The values obtained are presented in table 4.5. They

| $I_i^{\pi_i}$ | $\lvert D_0/Q_0 \rvert$ ($10^{-4}$ fm$^{-1}$) |
|---|---|
| $7^-$ | 5.5(1.1) |
| $8^+$ | 6.9(1.3) |
| $9^-$ | 8.7(2.1) |
| $10^+$ | 10.5(1.2) |
| $11^-$ | 9.0(1.8) |
| $12^+$ | 8.2(1.7) |
| $13^-$ | 8.6(1.5) |
| Weighted Mean | 7.9(0.5) |

Table 4.5: Values of the ratio of the intrinsic electric dipole to intrinsic electric quadrupole moment, $|D_0/Q_0|$. These are extracted from the data using the measured $E1/E2$ $\gamma$-ray branching ratios, and rotational model formulae.

are approximately constant within errors, giving a weighted mean value of $7.9(5) \times 10^{-4}$ fm$^{-1}$. However, due to the somewhat large nature of the error in these values, it is also possible that the values are consistent with the linear dependence on

spin of $|D_0/Q_0|$ observed by Ackermann *et al.* [Ackermann 93] for $^{224}$Th.

Assuming that the tentatively assigned $2^+ \rightarrow 0^+$ transition is correct, an estimate [Grodzins 62] for the intrinsic quadrupole moment can be made. The experimental values [Raman 87] of $Q_0$ for the Th isotopes in this mass region, and the heavier U isotopes can be reproduced by requiring that $T_\gamma(E2; 2 \rightarrow 0) = (2.9 \pm 0.3) \times 10^{10} E_\gamma^4 Z^2 A^{-1}$ compared to the value $T_\gamma(E2; 2 \rightarrow 0) = (4 \pm 2) \times 10^{10} E_\gamma^4 Z^2 A^{-1}$ given in reference [Grodzins 62]. This yields a value for the intrinsic quadrupole moment of $^{226}$U equal to 740(80) fm$^2$, and a value for the magnitude of the intrinsic dipole moment, $|D_0|$, of 0.58(7) fm. Though there are very few theoretical estimates of this quantity available for $^{226}$U, the experimental value obtained compares reasonably well to that calculated from the liquid drop plus shell correction approach employed in [Butler 91] (0.45 fm; see section 2.2.3 for a description of the method employed in the calculations). The measurement of the intrinsic dipole moment presented here is also comparable to the largest experimentally measured values in $^{222,224}$Th of 0.38 and 0.52 fm, respectively (see refs. [Ward 83, Ackermann 93]).

# Chapter 5

# Fine Structure in the Alpha Decay of $^{230}$Pu

## 5.1 Introduction

In this chapter, the results of an experiment to populate the first excited $2^+$ state in $^{226}$U via the $\alpha$ decay of $^{230}$Pu are presented. In the recoil-decay tagging measurement, it was not possible to confidently determine the excitation energy of this state due to large internal conversion and the low efficiency of the JUROSPHERE array at low ($< 100$ keV) energies. In the heavier isotopes of Pu, the branching ratio for the $\alpha$ decay into the $2^+$ state of the daughter isotope is around 30%, therefore it is reasonable to assume that the branching ratio may be similar in the case of $^{230}$Pu. A measurement of the excitation energy of the $2^+$ state in $^{226}$U allows the absolute excitation energies of the higher lying states to be deduced. A determination of the relative branching ratios to the ground and $2^+$ states also provides information which can be used to improve the systematics of the behaviour of the reduced $\alpha$-decay width in the region.

## 5.2 Experimental Details

For this study the RITU gas-filled separator was again employed, though no Ge array was placed at the target position. The Si-strip detector at the focal plane of RITU was used in 16-strip mode, which leads to improved granularity and resolution. The improved granularity reduces the contribution from accidental correlations. The pulse-processing electronics for the Si-strip detector were identical to those described in section 4.1.1. The data acquisition system is based upon standard CAMAC units. The outputs from the multiplexers are fed to Silena CAMAC ADCs. The master trigger is generated by the "busy" signal from the pattern trigger unit. The time of each event is recorded, and given by a scaler+clock with a resolution of 100$\mu$s. Since this clock overflows every 6.5536 seconds, a correction must be made in the offline analysis so that events are not lost when the time differences between events are calculated. Subsequent to the experiment, the data were converted into EUROGAM format, and again the MIDAS user interface package was used to perform the offline analysis.

In order to produce the $^{230}$Pu nuclei, the $^{208}$Pb($^{26}$Mg,4n)$^{230}$Pu reaction was employed. A rotating $^{208}$Pb target wheel was used with foil thicknesses varying between 500 and 800 $\mu$g/cm$^2$. The helium gas in the RITU device was separated from the beam-line vacuum by a 0.45 mg/cm$^2$ nickel foil. A natural Mg compound (Magnesoscene $Mg(C_5H_5)_2$) was placed in the JYFL ECR ion source to enable extraction of a $^{26}$Mg beam through the MIVOC method [Koivisto 94]. The $^{26}$Mg beam was then accelerated to an energy of 140 MeV by the K=130 MeV cyclotron. The energy loss through the Ni gas containment window was 2.4 MeV. A further single 0.9 mg/cm$^2$ nickel foil was used to degrade the incident beam to a centre of target energy of around 132 MeV, where fusion-evaporation code HIVAP [Reisdorf 81] calculations predict the maximum cross section for the reaction given above. In this experiment the beam was macro pulsed with beam phases of 5 ms on/5 ms off and 8 ms on/2 ms off in order to reduce the background from beam related events. The average beam current before pulsing was approximately 30 particle nA. The average count rate in the RITU Si-strip detector was 8 - 10 Hz. The total irradiation time was approxi-

mately 70 hours. Since the states populated by $\alpha$ decay were expected to be of low energy, and the $\gamma$ transitions strongly converted, no Ge detector was placed behind the focal-plane Si-strip detector of RITU.

## 5.3 Results

The total singles $\alpha$ spectrum of events occurring between beam pulses from the $^{26}Mg$ + $^{208}Pb$ reaction is shown figure 5.1. The peaks which dominate the $\alpha$ spectrum are due to the $\alpha$-decay of nuclei produced by transfer of several nucleons from the beam to the target. Indeed, the peaks corresponding to the $\alpha$ decay of fusion-evaporation products are not visible in this spectrum. It is necessary to perform an $\alpha$-$\alpha$ correlation to extract the events of interest from this background. The distribution of events at low energies (< 2 MeV) is due to $\alpha$ particles escaping the detector and depositing only a small amount of their kinetic energy. To extract events corresponding to the $\alpha$ decay of $^{230}Pu$ , a search was made for pairs of position and time correlated $\alpha$-$\alpha$ events, using the same method as described in section 4.2.3. In this case, the second event (in the same strip) had the constraint of having an energy between (7545 to 7585) or (7960 to 8000) keV corresponding to the known ground state to ground state $\alpha$-particle energies of $^{226}U$ and $^{222}Th$, respectively. No constraint was placed upon the energy of the first event occurring in the $\alpha$-$\alpha$ chain. The maximum allowed time interval between pairs of events was 900 ms. Searching for the decay of either $^{226}U$ or $^{222}Th$ subsequent to the first event gives a factor of 1.5 improvement in statistics when compared to a search made only for $^{226}U$. This is due to the fact that the probability of an $\alpha$ particle escaping the detector is approximately 50%. Again the vertical position window was approximately $\pm$ 1 mm. The spectrum of events correlated to the decay of either $^{226}U$ or $^{222}Th$ is presented in figure 5.2.

Here, it can be seen that there is a distribution of events at lower energy than that of the main peak. The energy of the main peak is 7055(17) keV, consistent with that measured for the $\alpha$ decay of $^{230}Pu$ [Andreyev 90]. The measured centroid of the

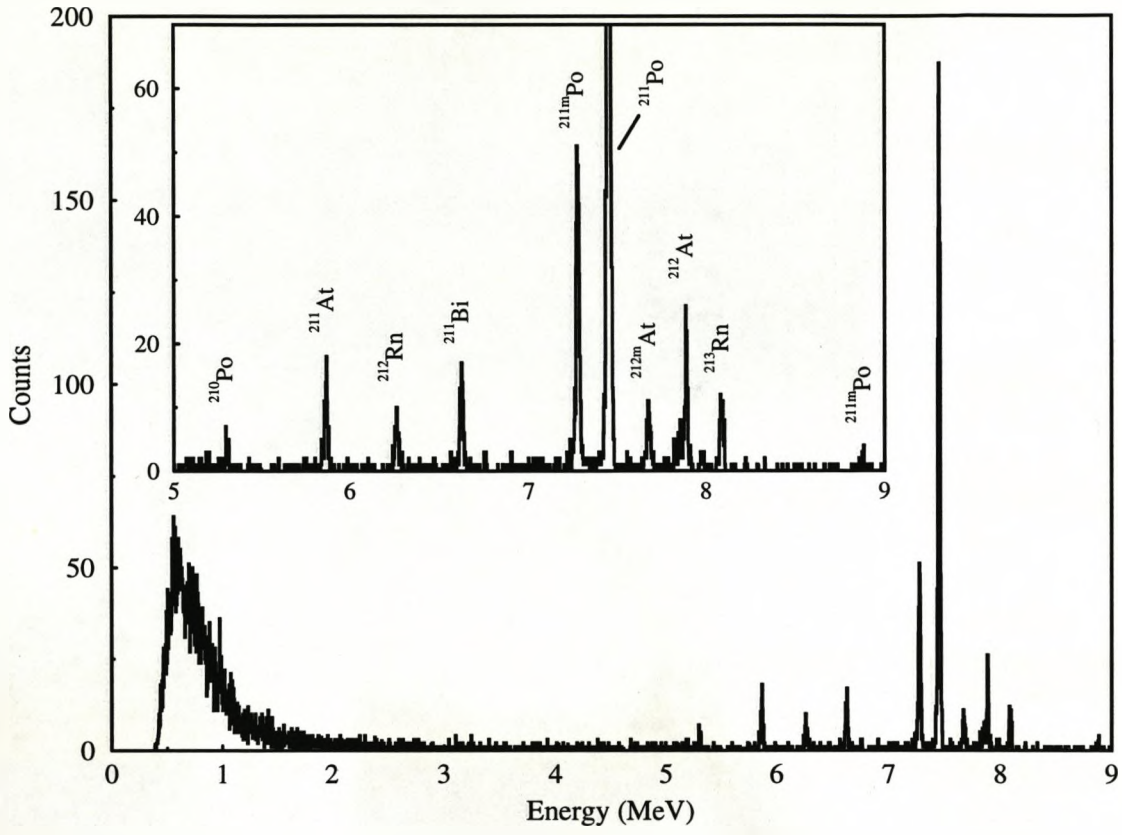


**Figure** 5.1: Spectrum of events occurring between beam pulses in the RITU Si-strip detector from the $^{26}Mg + ^{208}Pb$ reaction. The centre of target bombarding energy was approximately 132 MeV.

distribution of events at lower energy is 6970(19) keV. The measured intensity ratios are 68(24)% and 32(16)% for the higher and lower distributions, respectively. These values are similar to the $\alpha$-decay branching ratios observed in the heavier Pu isotopes [Akovali 98]. Thus it is reasonable to assume that the lower energy distribution corresponds to the $\alpha$ decay of $^{230}Pu$ to the $2^+$ state of $^{226}U$. However, if this is the case, it is expected that the measured centroid will be shifted to higher energy, due to the effect of conversion electrons summing with the $\alpha$ particle energy. The summing occurs because the source of the $\alpha$ activity is implanted into the sensitive detector layer. The effect of summing of the $\alpha$ particle energy with the conversion electron energy following population of excited states in the daughter nucleus has been in-

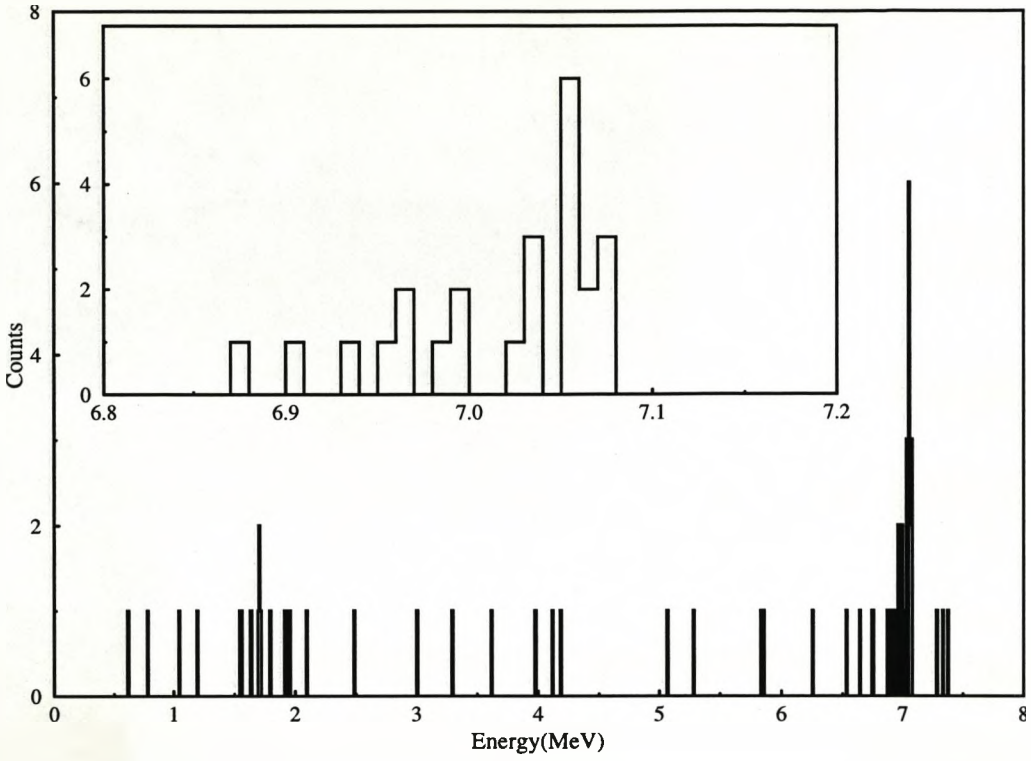


**Figure** 5.2: Events position and time correlated to the $\alpha$ decay of either $^{226}$U or $^{222}$Th, within a maximum search interval of 900 ms. The inset to this figure shows an expansion of the region around 7.0 MeV.

vestigated previously [Heßberger 89]. The probability that the conversion electrons deposit their full energy can be determined from the following expressions:

$$p = 0.5\left[\frac{(d_s - d_i)}{r + \frac{d_i}{r}}\right] = 0.5\frac{d_s}{r} \quad for \;\; r \geq d_s, \tag{5.1}$$

and

$$p = 0.5 + \frac{d_i}{r} \qquad\qquad for \;\; r < d_s, \tag{5.2}$$

where $d_s$ is the depletion depth of the detector, $d_i$ is the implantation depth of the $\alpha$-decaying source, and $r$ is the range of the emitted electrons in Si [Heßberger 89]. Since the excitation energy of the $2^+$ state in $^{226}$U is not known, it is difficult to estimate the shift in energy of the $\alpha$ peak due to summing of conversion electrons.

For this reason, a Monte Carlo computer code was employed to simulate the summing effect. The Monte Carlo simulation is discussed in the following section.

### 5.3.1 Monte Carlo Simulation

The Monte Carlo simulation determines the total energy deposited by a particular event in the Si-strip detector from a knowledge of the following parameters:

- the ground-state to ground-state $\alpha$-particle energy,
- the excitation energy of the excited state,
- the relative $\alpha$ decay branching ratios to the ground and excited states,
- the detector resolution,
- and the implantation depth of the evaporation residue.

The relevant internal conversion coefficients are taken from values tabulated by Rösel *et al.* [Rösel 78]. The emission of, and energy deposited by X-rays following internal conversion is also taken into account. The initial emission of $\alpha$ particles, electrons and photons is assumed to be isotropic. The energy deposited by the $\alpha$ particles is dependent upon the implantation depth and the direction of emission. If the direction of emission is such that the $\alpha$ particle may escape the detector, the distance to the front face of the detector is calculated and subtracted from the full range of the $\alpha$ particle in question. If the distance is greater than the full range of the $\alpha$ particle, then the full energy is deposited. If the distance is less than the full range, then only part of the $\alpha$ particle energy is deposited. The path of the electron is calculated assuming the differential cross section for the interaction between electrons and Si given by Kuzminikh and Vorobiev [Kuzminikh 75]. The integrated scattering length is then used in conjunction with the empirical expression for the range of electrons in Si given by Kantele [Kantele 95] in order to obtain the energy deposited by the electron. This prescription to describe the multiple scattering of electrons in Si was

used by Butler *et al.* in a Monte Carlo simulation to investigate the properties of detectors used in conversion electron spectroscopy [Butler 96a].

In order to test the Monte Carlo simulation, data from the recoil-decay tagging measurement were used. In these data, the $\alpha$ decay of $^{226}$U into the $2^+$ state of $^{222}$Th was observed with reasonable statistics. In order to cleanly extract a spectrum of events corresponding to the $\alpha$ decay of $^{226}$U, a triple $\alpha$-$\alpha$-$\alpha$ correlation was performed. Again the energy of the first event was allowed vary freely, with the demand that the second and third events must have an energy corresponding in the ranges (7942 to 8022) keV and (17.1 to 17.5) MeV, respectively. The former range corresponds to the $^{222}$Th ground state to ground state $\alpha$ particle energy, whilst the latter range corresponds to the full energy summing peak of the $\alpha$ particle energies of $^{218}$Ra and $^{214}$Rn. In this case, the two $\alpha$ particle energies sum, since the half-life of $^{214}$Rn is less than one $\mu$s. The pulse-processing electronics used are not capable of resolving the energies of the two $\alpha$ particles. The maximum time difference between events of type $\alpha_1$-$\alpha_2$ was 12 ms, and between events of type $\alpha_2$-$\alpha_{sum}$ was 0.15 ms. The spectrum of events extracted from these search criteria is shown in the upper panel of figure 5.3. Shown in the lower panel of figure 5.3 is a spectrum of events detected in a Ge detector placed behind the RITU Si-strip detector, in coincidence with events of energy (7340 to 7430) keV in the focal plane Si-strip detector. The peak at 183 keV is due to the $\gamma$ de-excitation of the $2^+$ state in $^{222}$Th; the observation of Ra X-rays in this figure is due to the tail of the $^{223}$Th $\alpha$-decay peak entering the coincidence gate. Here, the dominant $\alpha$ decay line from $^{223}$Th populates an excited $5/2^+$ state in $^{219}$Ra, which then decays via a strongly converted 140 keV $M1$ transition to the $7/2^+$ ground state. The difference in energy of the two $\alpha$-decay lines shown in the upper panel of figure 5.3 is 175 keV (measured energies: 7390(5) keV and 7565(5) keV) . The small discrepancy (175 compared to 183 keV) is due to the effect of conversion electrons summing with the $\alpha$ decay energy. Since the excitation energy of the $2^+$ state in $^{222}$Th is known (183 keV), this can be used as the input for the Monte Carlo simulation. The inten-

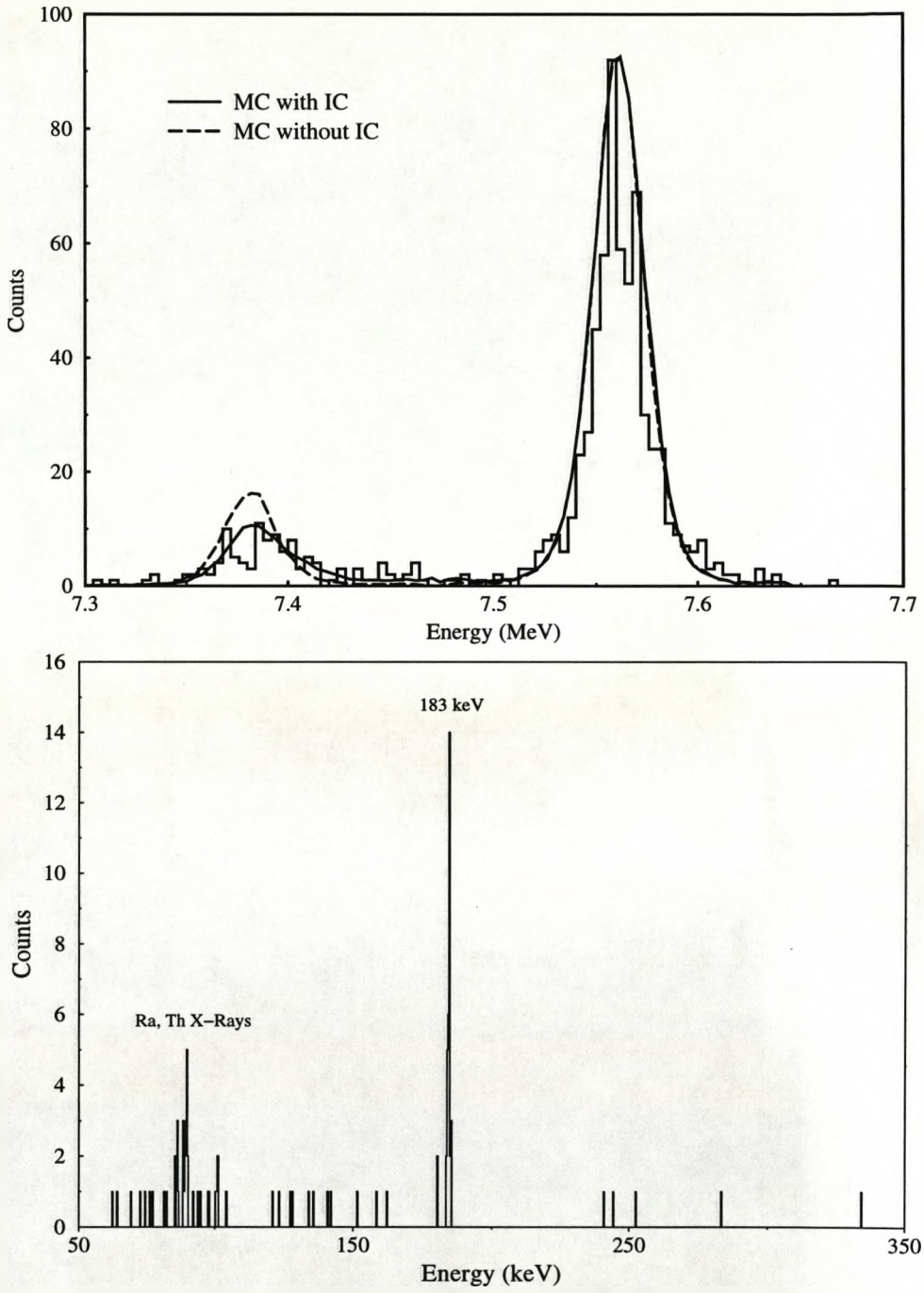


**Figure** 5.3: Upper panel: Events correlated to the decay of $^{222}$Th and full energy sum peak of $^{218}$Ra + $^{214}$Rn. The solid line and dashed lines are the results of Monte Carlo simulations with and without the inclusion of internal conversion, respectively. Lower panel: Gamma-ray events in coincidence with events of energy (7340 to 7430) keV in the focal plane Si-strip detector.

sity ratios to the ground and excited states were measured to be 84(4) and 16(2)%, respectively. The spectrum obtained from the Monte Carlo simulation is shown as the solid line in the upper panel of figure 5.3. Also shown, for comparison (dashed line), is the result of the Monte Carlo simulation if internal conversion is neglected. It is clear that the summing effect pushes the centroid of the fine structure peak to higher energy, and also has the effect of "smearing" the intensity over a wider energy range. The Monte Carlo simulation with the inclusion of internal conversion reproduces the experimentally measured $\alpha$-particle energies to within 0.5 keV. The $\alpha$-particle energy for the decay of $^{226}$U to the $2^+$ state of $^{222}$Th, corrected for the summing effect, is then 7385(5) keV.

Figure 5.4 shows further output from the Monte Carlo simulation. The long-dashed line corresponds to events which originate from decays to the $2^+$ state in $^{222}$Th. It can be seen that the summing effect shifts a fraction of the events below the ground state to ground state $\alpha$-decay peak. The measured intensity ratios given earlier must therefore be corrected in order to obtain the branching ratios. The fraction of decays to the $2^+$ state which are shifted into the ground state to ground state $\alpha$-decay peak is 13%. The corrected branching ratios are then 82(4)% and 18(2)% for the decays to the ground and $2^+$ states, respectively.

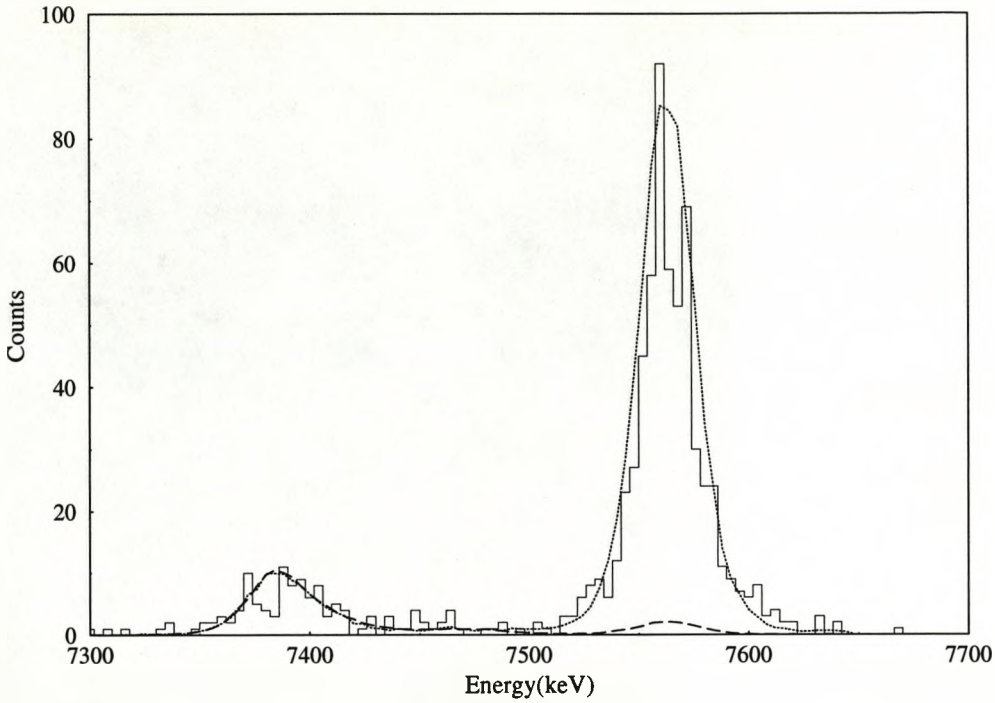


**Figure** 5.4: Further output from the Monte Carlo simulation. The long-dashed line corresponds to those events which originate from decays to the $2^+$ state in $^{222}$Th, showing that a fraction of the events are shifted beneath the ground state to ground state $\alpha$-decay peak.

In the case of the $\alpha$ decay of $^{230}$Pu, since the transition energy is not known, the energy of the $2^+$ to $0^+$ transition input into the Monte Carlo code is varied, and the centroid separation of the two peaks in the resulting spectrum measured, in order to obtain a calibration curve. The curve obtained is shown in figure 5.5. The transition energy which best reproduces the experimentally observed centroid separation is then taken as the transition energy. The experimentally observed centroid separation is 85(25) keV, which (from the Monte Carlo simulation) is given by a transition energy of 96(25) keV. This value is consistent with that obtained in the RDT measurement. The resulting Monte Carlo spectrum is shown together with the experimental data in figure 5.6. Using this transition energy, the $\alpha$-particle energy for the decay $^{230}$Pu (ground state) to $^{226}$U ($2^+$) is deduced to be 6961(30) keV. Measurement of the $2^+$ to

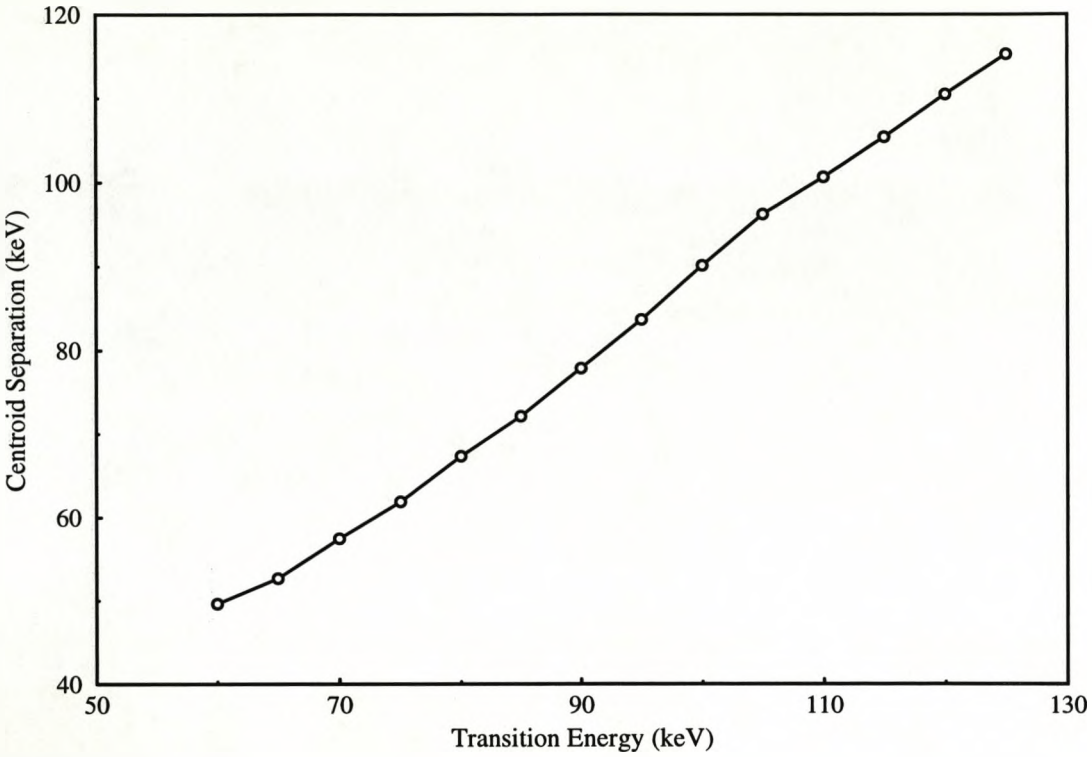


**Figure** 5.5: Calibration curve obtained from the Monte Carlo simulations. The transition energy input into the Monte Carlo code is shown on the x-axis and the resulting centroid separation in the output spectrum on the y-axis.

$0^+$ transition energy allows an estimate of the deformation parameter $\beta_2$ to be made, using the empirical relationships of refs. [Grodzins 62, Stephens 72]. The deduced value for $^{226}$U, using 96 keV, is $\beta_2 \simeq 0.20$. This is similar to that of the isotone, $^{224}$Th, and follows the systematic trend of decreasing deformation observed in the heavier U isotopes. Also in figure 5.6 (dashed line) is an output spectrum from the Monte Carlo simulation showing those events shifted beneath the ground state to ground state $\alpha$-decay peak. In this case, the fraction of shifted events is 35%, and the corrected branching ratios are 51(22)% and 49(25)% for the $\alpha$ decays to the ground and $2^+$ states, respectively.

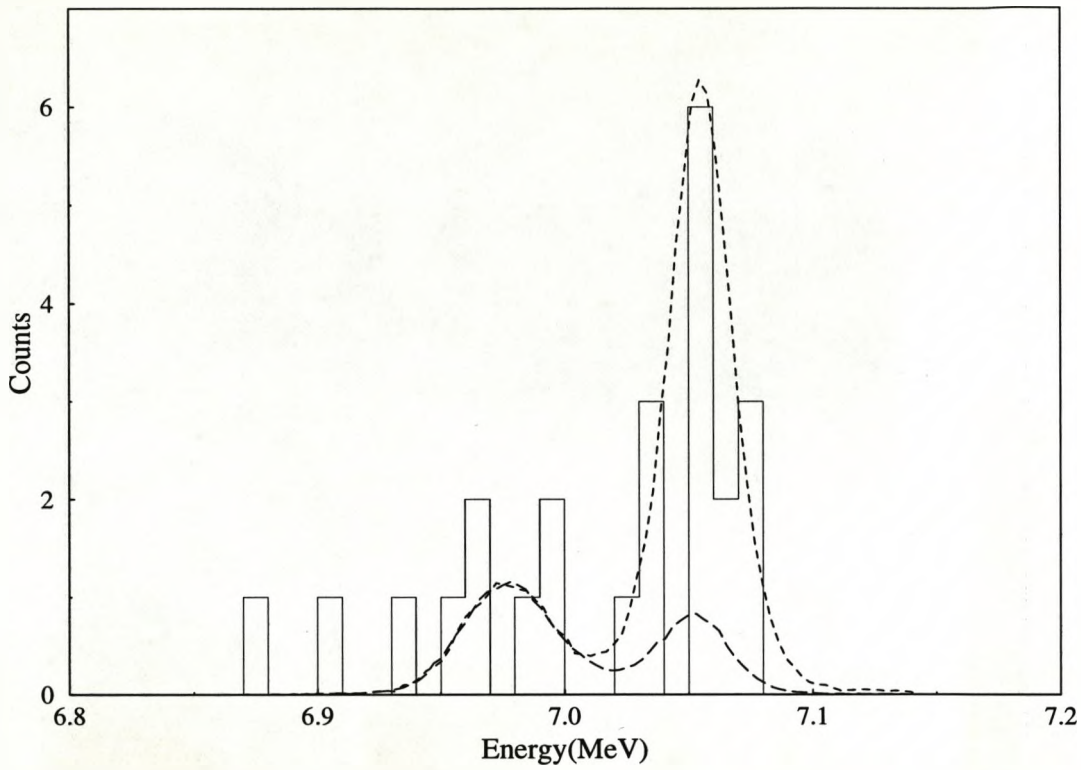


**Figure** 5.6: Experimental data as in figure 5.2. The dotted line is the spectrum obtained from a Monte Carlo simulation of the $\alpha$ decay of $^{230}$Pu into $^{226}$U. The input excitation energy of the $2^+$ state in $^{226}$U for the simulation is 96 keV. The dashed line (from the Monte Carlo simulation) corresponds to those events which originate from decays to the $2^+$ state of $^{226}$U.

### 5.3.2 Hindrance Factors

The improved measurements of the $\alpha$-decay properties of $^{226}$U, together with those for $^{230}$Pu, have been used to calculate hindrance factors for the decays to $2^+$ states. The formalism of Rasmussen [Rasmussen 59] was employed in the calculations (see section 3.5.1). A plot of the calculated values is shown in the lower panel of figure 5.7. Data for the heavier isotopes of U and Pu are taken from reference [Akovali 98].

Though the $\alpha$-decay half-life of $^{230}$Pu has not been measured, it is possible to estimate the ground state to ground state partial half-life from an extrapolation of the Geiger-Nuttall curves. The Geiger-Nuttall curves for several even-even isotopes

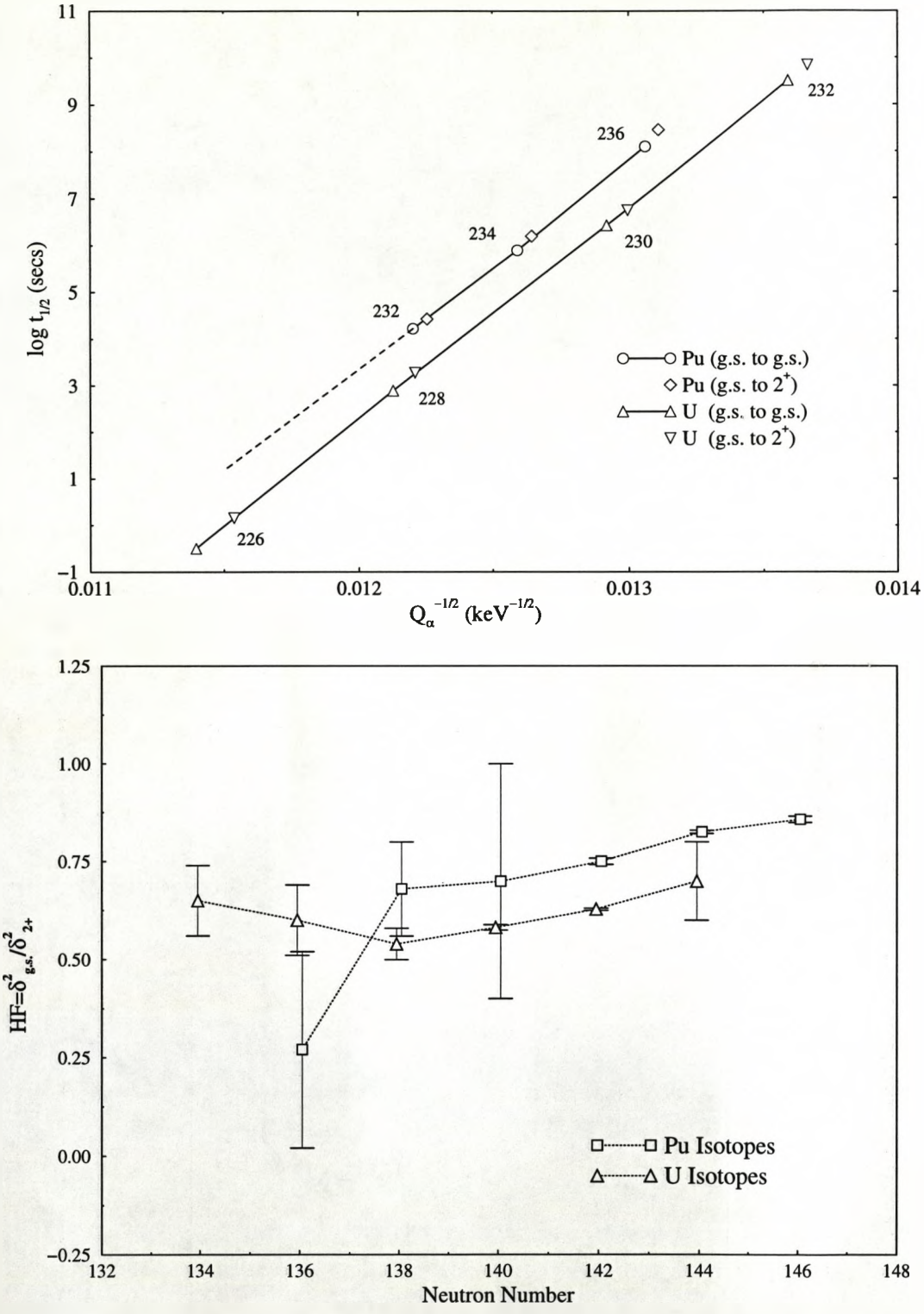


**Figure** 5.7: Upper panel: Plots of $Q_\alpha^{-1/2}$ against the logarithm of the partial half-life for several even-even U and Pu isotopes. The dashed line is an extrapolation used to deduce the $\alpha$-decay partial half-life for the ground to ground state $\alpha$ decay of $^{230}$Pu. Lower panel: Hindrance factors for the $\alpha$ decays to $2^+$ states, calculated using the formalism of Rasmussen [Rasmussen 59].

of U and Pu are shown in the upper panel of figure 5.7. The dashed line is the extrapolation. Using the branching ratios given previously, the $\alpha$ partial half-life of $^{230}$Pu was determined to be 154(66) s. It was not possible to measure this half-life in the present experiment, since the average time between events in each pixel of the Si-strip detector was approximately 30 s.

It can be seen from the calculated hindrance factors that for the isotopes of U, the systematic trend is parabolic around neutron number 138. The value for $^{226}$U determined in this work (HF = 0.65(9)) fits nicely with the systematic trend. In contrast with this is the value deduced for $^{230}$Pu (HF = 0.27(24)), which does not fit well with the systematic trend, though the error is very large. However, within the limits of the error bar it can said that the hindrance factors continue to decrease below neutron number 138. A much improved measurement of the branching ratio, along with a determination of the decay half-life would be desirable to confirm this trend.

## 5.4 Summary

Excited yrast states in the neutron-deficient nucleus $^{226}$U have been observed for the time using the recoil-decay tagging technique. The first observation of fine structure in the $\alpha$ decay of $^{230}$Pu has allowed a determination of the $^{226}$U $2^+$ to $0^+$ transition energy. A level scheme, deduced from the results of both experiments carried out in the course of this work is presented in figure 5.8. Though the $2^+$ to $0^+$ transition energy extracted from the $^{230}$Pu $\alpha$-decay experiment is somewhat larger than that given in Chapter 4, the conclusions presented regarding the rotational alignment properties and the ratio of the intrinsic electric dipole to electric quadrupole moment remain unchanged. A correction should, however, be made to the magnitude of the intrinsic dipole moment given in section 4.7. For a transition energy of 96(25) keV, the intrinsic quadrupole moment $Q_0$ of $^{226}$U is 680(190) fm$^2$. The magnitude of the intrinsic dipole moment $D_0$ is then 0.54(15) fm.

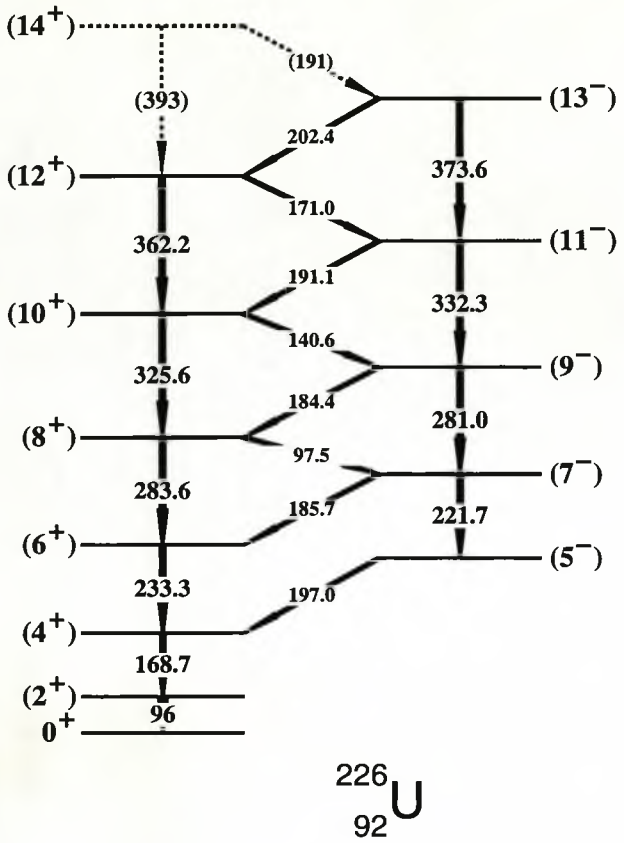


**Figure** 5.8: Level scheme deduced from the results of both experiments carried out in this work.

The behaviour of the difference in aligned angular momentum, $\Delta i_x$, between the positive- and negative-parity states is consistent with that expected for a rotating body with a reflection-asymmetric shape. The region of known octupole deformation has been extended to $Z = 92$. In addition, the intrinsic electric dipole moment of $^{226}$U, extracted from measurement of $E1/E2$ $\gamma$-ray branching ratios, is comparable to largest experimentally measured values in the region.

## 5.5 Future Prospects

The calculations of Nazarewicz *et al.* [Nazarewicz 84], presented in figure 2.3, show that $^{224}$U possesses one of the deepest minima for non-zero $\beta_3$ in the actinide region.

To date, this potentially interesting nucleus remains unstudied, due to the experimental difficulties involved.

The cross section for production of $^{224}$U, using the reaction $^{208}$Pb($^{20}$Ne,4n)$^{224}$U , is approximately 800 nanobarns [Yeremin 94]. In addition to this reduction in production cross section, the $\alpha$-decay energy of $^{224}$U coincides with that of $^{221}$Th, which is strongly produced in the same reaction. This means that a correlation of the type E.R. – $\alpha_1$ – $\alpha_2$ (see section 4.2.3) is required in order to uniquely identify $^{224}$U. This results in a factor of two reduction in statistics due to the loss of $\alpha$ particles which do not deposit their full energy in the detection system. A study of $^{224}$U using the recoil-decay tagging technique therefore does not seem feasible with currently available devices.

However, the use of an efficient recoil detector such as a parallel-plate avalanche counter, in conjunction with a germanium array such as EUROBALL or GAMMASPHERE may allow the study of many weakly-produced nuclei in and above this mass region. The large sea of background $\gamma$ rays from fission can be strongly suppressed, and conventional $\gamma$-ray spectroscopic techniques may then be used to extract the $\gamma$-rays of interest.

# References


[Ackermann 93] B. Ackermann *et al.*, Nucl. Phys. **A559** 61 (1993)

[Ahmad 88] S.A. Ahmad, W. Klempt, R. Neugart, E.W. Otten, P.-G. Reinhard, G. Ulm and K. Wendt, Nucl. Phys. **A483** 244 (1988)

[Aïche 88] M. Aïche *et al.*, J. Phys. G **14** 1191 (1988)

[Aïche 94] M. Aïche *et al.*, Nucl. Phys. **A567** 685 (1994)

[Akovali 98] Y.A. Akovali, Nucl. Data. Sheets **84** 1 (1998)

[Andreyev 89] A.N. Andreyev, D.D. Bogdanov, A.V. Yeremin, A.P. Kabachenko, O.A. Orlova, G.M. Ter-Akop'yan and V.I. Chepigin, Sov. J. Nucl. Phys. **50** 3 (1989)

[Andreyev 90] A.N. Andreyev *et al.*, Z. Phys. A **337** 231 (1990)

[Artna-Cohen 91] A. Artna-Cohen, Nucl. Data. Sheets **63** 79 (1991)

[Asaro 53] F. Asaro, F.S. Stephens and I. Perlman, Phys. Rev. **92** 1495 (1953)

[Bardeen 57] J. Bardeen, L.N. Cooper and J.R. Schreifer, Phys. Rev. **108** 1175 (1957)

[Beausang 96] C.W. Beausang and J. Simpson, J. Phys. G **22** 527 (1996)

[Bengtsson 79] R. Bengtsson and S. Frauendorf, Nucl. Phys. **A327** 139 (1979)

[Bengtsson 85] R. Bengtsson and J.D. Garrett, In. Rev. Nucl. Phys. **1** World Scientific (1985)

[Blatt 52] J.M. Blatt and V.F. Wiesskopf, *Theoretical Nuclear Physics*, John Wiley and Sons Inc., New York (1952)

[Bohr 36] N. Bohr, Nature **344** 137 (1936)

[Bohr 39] N. Bohr, Phys. Rev. **56** 426 (1939)

[Bohr 57] A. Bohr and B.R. Mottelson, Nucl. Phys. **4** 529 (1957)

[Bohr 58] A. Bohr, B.R. Mottelson and D. Pines, Phys. Rev. **110** 936 (1958)

[Bohr 58a] A. Bohr and B.R. Mottelson, Nucl. Phys. **9** 687 (1958)

[Bohr 69] A. Bohr and B.R. Mottelson, *Nuclear Structure Volume I: Single-Particle Motion*, W.A. Benjamin Inc., New York (1969)

[Bohr 75] A. Bohr and B.R. Mottelson, *Nuclear Structure Volume II: Nuclear Deformations*, W.A. Benjamin Inc., New York (1975)

[Bonin 83] W. Bonin *et al.*, Z. Phys. A **310** 249 (1983)

[Bonin 85] W. Bonin *et al.*, Z. Phys. A **322** 59 (1985)

[Borchers 87] W. Borchers, R. Neugart, E.W. Otten, H.T. Duong, G. Ulm and K. Wendt, Hyperfine Interactions **34** 25 (1987)

[Browne 92] E. Browne, Nucl. Data. Sheets **65** 669 (1992)

[Butler 91] P.A. Butler and W. Nazarewicz, Nucl. Phys. **A533** 249 (1991)

[Butler 96] P.A. Butler and W. Nazarewicz, Rev. Mod. Phys. **68** 349 (1996)

[Butler 96a] P.A. Butler *et al.*, Nucl. Instrum. Methods Phys.Res. A **381** 433 (1996)

[Casten 90] R.F. Casten, *Nuclear Structure from a Simple Perspective*, Oxford University Press, Oxford (1990)

[Chasman 80] R.R. Chasman, Phys. Lett. B **96** 7 (1980)

[Cocks 97] J.F.C. Cocks *et al.*, Phys. Rev. Lett. **78** 2920 (1997)

[Cocks 99] J.F.C. Cocks *et al.*, Nucl. Phys. **A645** 61 (1999)

[Cohen 58] B.L. Cohen and C.B. Fulmer, Nucl. Phys. **6** 547 (1958)

[Condon 28] E.U. Condon and R.W. Gurney, Nature **122** 439 (1928)

[Cristancho 94] F. Cristancho *et al.*, Phys. Rev. C **49** 663 (1994)

[Dahlinger 88] M. Dahlinger *et al.*, Nucl. Phys. **A484** 337 (1988)

[Davids 89] C.N. Davids and J.D. Larson, Nucl. Inst. Meth. Phys. Res. B **40/41** 1224 (1989)

[Debray 90] M.E. Debray *et al.*, Phys. Rev. C **41** R1895 (1990)

[Debray 94] M.E. Debray *et al.*, Nucl. Phys. **A568** 141 (1994)

[De Shalit 74] A. De Shalit and H. Feshbach, *Theoretical Nuclear Physics Volume 1: Nuclear Structure*, John Wiley and Sons Inc., New York (1974)

[Dorso 86] C.O. Dorso, W.D. Myers and W.J. Swiatecki, Nucl. Phys. **A451** 189 (1986)

[Egido 90] J.L. Egido and L.M. Robledo, Nucl. Phys. **A518** 475 (1990)

[Ennis 92] P.J. Ennis and C.J. Lister, Nucl. Inst. Meth. Phys. Res. A **313** 413 (1992)

[Enqvist 97] T. Enqvist *et al.*, Nucl. Inst. Meth. Phys. Res. B **126** 344 (1997)

[Fernández-Niello 82] J. Fernández-Niello, H. Puchta, F. Reiss and W. Trautmann, Nucl. Phys. **A391** 221 (1982)

[Fernández-Niello 91] J. Fernández-Niello, C. Mittag, F. Reiss, E. Ruchowska and M. Stallknecht, Nucl. Phys. **A531** 164 (1991)

[Gamow 28] G. Gamow, Z. Phys. **51** 204 (1928)

[Geiger 11] H. Geiger and J.M. Nuttall, Phil. Mag. **22** 613 (1911)

[Ghiorso 88] A. Ghiorso *et al.*, Nucl. Inst. Meth. Phys. Res. A **269** 192 (1988)

[Goodman 74] A.L. Goodman, Nucl. Phys. **A230** 466 (1974)

[Green 54] A.E.S. Green, Phys. Rev. **95** 1006 (1954)

[Greenlees 98] P.T. Greenlees *et al.*, J. Phys. G **24** L63 (1998)

[Grodzins 62] L. Grodzins, Phys. Lett. **2** 88 (1962)

[Haenni 77] D.R. Haenni and T.T. Sugihara, Phys. Rev. C **16** 120 (1977)

[Harris 65] S.M. Harris, Phys. Rev. B **138** 509 (1965)

[Haxel 49] O. Haxel, D. Jensen and H.E.Suess, Phys. Rev. **75** 1766 (1949)

[Heßberger 89] F.P. Heßberger, S. Hofmann, G. Münzenberg, K.-H. Schmidt and P. Armbruster, Nucl. Inst. Meth. Phys. Res. A **274** 522 (1989)

[Hughes 90] J.R. Hughes *et al.*, Nucl. Phys. **A512** 275 (1990)

[Inglis 54] D.R. Inglis, Phys. Rev. **96** 1059 (1954)

[Johnson 71] A. Johnson, H. Ryde and J. Sztarkier, Phys. Lett. B **34** 605 (1971)

[Kantele 95] J. Kantele, *Handbook of Nuclear Spectroscopy*, Academic Press, New York (1995)

[Koivisto 94] H. Koivisto, J. Ärje and M. Nurmia, Nucl. Inst. Meth. Phys. Res. B **94** 291 (1994)

[Krane 88] K.S. Krane, *Introductory Nuclear Physics*, John Wiley and Sons, New York (1988)

[Kuusiniemi 99] P. Kuusiniemi, *Private Communication* (1999)

[Kuzminikh 75] V.A. Kuzminikh and S.A. Vorobiev, Nucl. Inst. Meth. **129** 561 (1975)

[Leander 84] G.A. Leander and R.K.Sheline, Nucl. Phys. **A413** 375 (1984)

[Leander 86] G.A. Leander, W. Nazarewicz, G.F. Bertsch and J. Dudek, Nucl. Phys. **A453** 58 (1986)

[Leino 81] M. Leino, S. Yashita and A. Ghiorso, Phys. Rev. C **24** 2370 (1981)

[Leino 95] M. Leino *et al.*, Nucl. Inst. Meth. Phys. Res. B **99** 653 (1995)

[Mang 57] H.J. Mang, Z. Phys. **148** 582 (1957)

[Mang 60] H.J. Mang, Phys. Rev. **119** 1063 (1960)

[Möller 81] P. Möller and J.R. Nix, Nucl. Phys. A **361** 117 (1981)

[Mottelson 60] B.R. Mottelson and J.G. Valatin, Phys. Rev. Lett. **5** 511 (1960)

[Muikku 98] M. Muikku *et al.*, Phys. Rev. C **58** R3033 (1998)

[Myers 74] W.D. Myers and W.J. Swiatecki, Ann. Phys. (N.Y.) **84** 186 (1974)

[Nazarewicz 84] W. Nazarewicz, P. Olanders, I. Ragnarsson, J. Dudek, G.A. Leander, P. Möller and E. Ruchowska, Nucl. Phys. **A429** 269 (1984)

[Nazarewicz 85] W. Nazarewicz and P. Olanders, Nucl. Phys. **A441** 420 (1985)

[Nazarewicz 87] W. Nazarewicz, G.A. Leander and J. Dudek, Nucl. Phys. **A467** 437 (1987)

[Nazarewicz 92] W. Nazarewicz and S.L. Tabor, Phys. Rev. C **45** 2226 (1992)

[Neergård 70] K. Neergård and P. Vogel, Nucl. Phys. **A145** 420 (1970)

[Neergård 70a] K. Neergård and P. Vogel, Nucl. Phys. **A149** 209 (1970)

[Neergård 70b] K. Neergård and P. Vogel, Nucl. Phys. **A149** 217 (1970)

[Nilsson 55] S.G. Nilsson, Kgl. Dan. Viden. Selsk. Mat. Fys. Medd. **29** No.16 (1955)

[Nilsson 95] S.G. Nilsson and I. Ragnarsson, *Shapes and Shells in Nuclear Structure*, Cambridge University Press, Cambridge (1995)

[Nolan 85] P.J. Nolan, D.W. Gifford and P.J. Twin, Nucl. Inst. Meth. Phys. Res. A **236** 95 (1985)

[Nolan 90] P.J. Nolan, Nucl. Phys. **A520** 657c (1990)

[Nolan 94] P.J. Nolan, F.A. Beck and D.B. Fossan, Ann. Rev. Nucl. Part. Sci. **45** 561 (1994)

[Oganessian 91] Yu. Ts. Oganessian *et al.*, JINR LNR Scientific Report, 158 (1991)

[Paul 95] E.S. Paul *et al.*, Phys. Rev. C **51** 78 (1995)

[Poynter 89] R.J. Poynter *et al.*, J. Phys. G. **15** 449 (1989)

[Poynter 89a] R.J. Poynter *et al.*, Phys. Lett. B **232** 447 (1989)

[Preston 62] M.A. Preston, *Physics of the Nucleus*, Addison-Wesley Publishing Company, Reading, Massachusetts (1962)

[Raman 87] S. Raman, C.H. Malarkey, W.T. Milner, C.W. Nestor Jr. and P.H. Stelson, At. Data Nucl. Data Tables **36** 1 (1987)

[Raman 91] S. Raman, C.W. Nestor Jr., S. Kahane, K.H. Blatt, Phys. Rev. C **43** 556 (1991)

[Rasmussen 59] J.O. Rasmussen, Phys. Rev. **113** 1593 (1959)

[Reisdorf 81] W. Reisdorf, Z. Phys. A **300** 227 (1981)

[Ring 80] P. Ring and P. Schuck, *The Nuclear Many-Body Problem*, Springer-Verlag (1980)

[Rohoziński 88] S.G. Rohoziński, Rep. Prog. Phys. **51** 541 (1988)

[Rösel 78] F. Rösel, H.M. Fries, K. Alder and H.C. Pauli, At. Data Nucl. Data Tables **21** 91 (1978)

[Roy 94] N. Roy *et al.*, Nucl. Phys. **A462** 397 (1994)

[Salem 74] S.I. Salem, S.L. Panossian and R.A. Krause, At. Data Nucl. Data Tables **14** 91 (1974)

[Schmidt 79] K.-H. Schmidt *et al.*, Nucl. Phys. **A318** 253 (1979)

[Schmidt 84] K.-H. Schmidt, C.-C. Sahm, K. Pielenz and H.-G. Clerc, Z. Phys. A **316** 19 (1984)

[Schulz 91] N. Schulz *et al.*, Z. Phys. A **339** 325 (1991)

[Sheline 87] R.K. Sheline, Phys. Lett. B **197** 500 (1987)

[Simon 86] R.S. Simon *et al.*, Z. Phys. A **325** 197 (1986)

[Smith 95] J.F. Smith *et al.*, Phys. Rev. Lett. **75** 1050 (1995)

[Spear 90] R.H. Spear and W.N. Catford, Phys. Rev. C **41** R1351 (1990)

[Stephens 54] F.S. Stephens, F. Asaro and I. Perlman, Phys. Rev. **96** 1568 (1954)

[Stephens 55] F.S. Stephens, F. Asaro and I. Perlman, Phys. Rev. **100** 1543 (1955)

[Stephens 72] F.S. Stephens *et al.*, Phys. Rev. Lett. **29** 438 (1972)

[Stephens 72a] F.S. Stephens and R.S. Simon, Nucl. Phys. **A183** 257 (1972)

[Strutinsky 56] V.M. Strutinsky, Atom. Energyia **4** 150 (1956)

[Strutinsky 67] V.M. Strutinsky, Nucl. Phys. **A95** 420 (1967)

[Strutinsky 68] V.M. Strutinsky, Nucl. Phys. **A112** 1 (1968)

[Sujkowski 77] Z. Sujkowski, D. Chmielewska, M.J.A. De Voigt, J.F.W. Jansen and O. Scholten, Nucl. Phys. **A291** 365 (1977)

[Takahashi 73] K. Takahashi, M. Yamada and T. Kondoh, At. Data Nucl. Data Tables **12** 101 (1973)

[Uusitalo 96] J. Uusitalo, Ph.D thesis, University of Jyväskylä (1996)

[Ward 83] D. Ward, G.D. Dracoulis, J.R. Leigh, R.J. Charity, D.J. Hinde and J.O. Newton, Nucl. Phys. **A406** 591 (1983)

[Wieland 92a] M. Wieland *et al.*, Phys. Rev. C **45** 1035 (1992)

[Wieland 92b] M. Wieland *et al.*, Phys. Rev. C **46** 2628 (1992)

[Yeremin 94] A.V. Yeremin *et al.*, Nucl. Instrum. Methods Phys. Res., Sect. A **350** 608 (1994)

[Zolnowski 75] D.R. Zolnowski, T. Kishimoto, Y. Gono and T.T. Sugihara, Phys. Lett. B **55** 453 (1975)